Perspectives on Emerging Engineering Technologies

Approaches Focused On Electrical-electronics and Communication Engineering

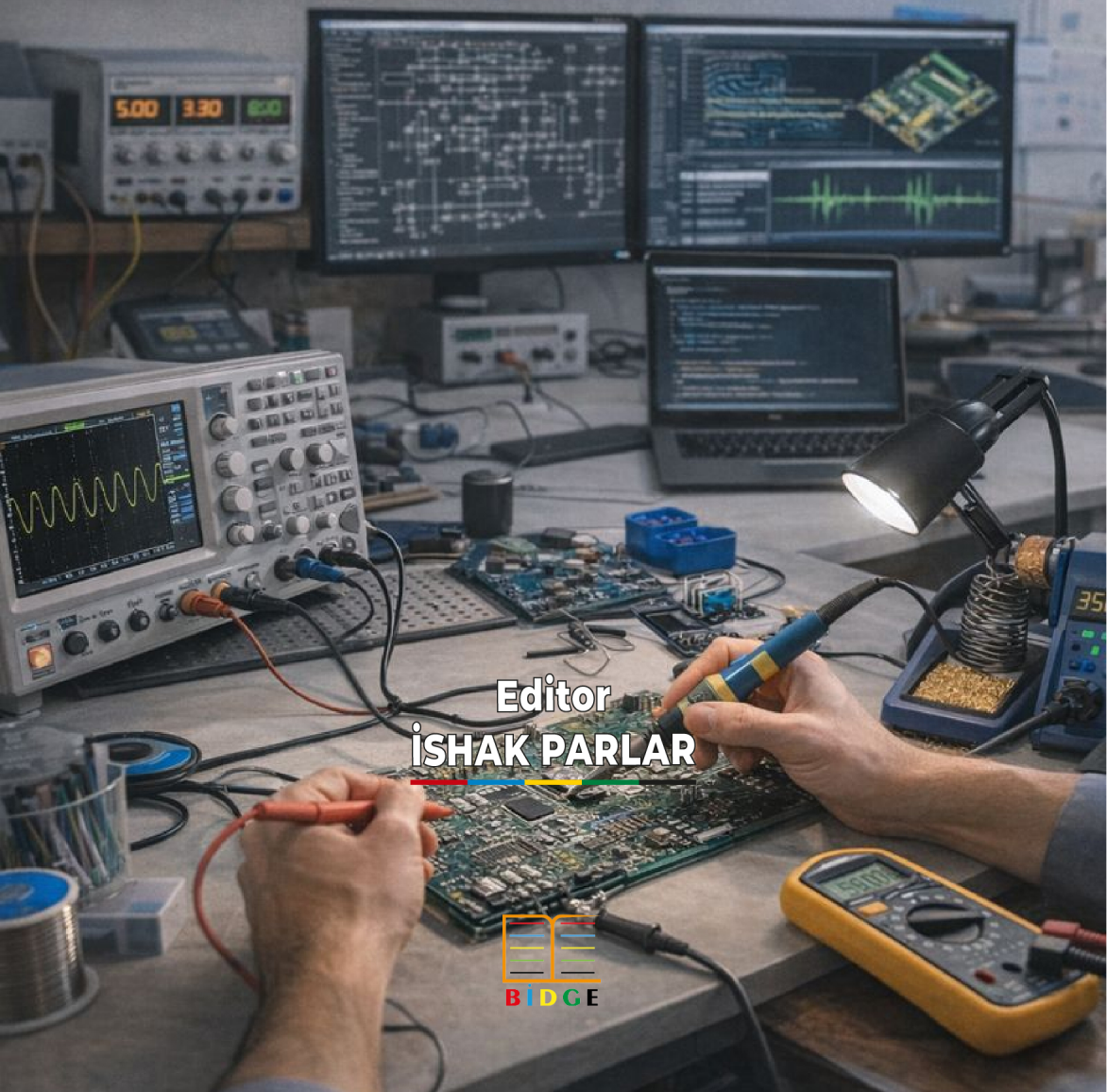

Editor
İSHAK PARLAR

BİDGE

BİDGE Yayınları

Perspectives on Emerging Engineering Technologies: Approaches Focused On Electrical-electronics and Communication Engineering

Editor: İSHAK PARLAR

ISBN: 978-625-8567-19-9

1st Edition
Page Layout By: Gözde YÜCEL
Publication Date: 2025-12-25
BİDGE Yayınları

Certificate No: 71374

www.bidgeyayinlari.com.tr - bidgeyayinlari@gmail.com
Krc Bilişim Ticaret ve Organizasyon Ltd. Şti.
Güzeltepe Mahallesi Abidin Daver Sokak Sefer Apartmanı No: 7/9 Çankaya / Ankara

PREFACE

Rapid advancements in engineering technologies have increasingly blurred the boundaries between traditional disciplines, leading to complex systems that require integrated and interdisciplinary approaches. This book brings together the latest theoretical developments and practical applications encompassing electromagnetic, microwave, and radio frequency systems, intelligent sensing, communication technologies, artificial intelligence, electric mobility, and advanced control methodologies. By offering contributions from diverse engineering fields, this book aims to provide a comprehensive overview of emerging technologies shaping the next generation of medical, industrial, and transportation systems. Designed for researchers, undergraduate and graduate students, and the related ecosystem, this book highlights how interdisciplinary collaboration supports innovative solutions to contemporary engineering challenges and the development of intelligent, efficient, and sustainable technological systems.

Asst. Prof. İshak PARLAR

VAN YUZUNCU YIL UNIVERSITY

İÇİNDEKİLER

CHAPTER 1

THE EVOLIOTION OF ELECTRIC MOTORS FROM THE DISCOVERY OF MAGNETISM TO TODAY'S ELECTRIC VEHICLES

HAYRETTİN GÖKOZAN[1]

The Development of Electric Motors

The development of electric motors, which convert electrical energy into mechanical energy, is a fascinating journey that began with simple laboratory experiments in the early 19th century and has evolved into a massive industry that powers the world today. The first steps related to electric motors began with the discovery of the connection between electric current and magnetism between 1820 and 1830. This started with Hans Christian Oersted's observation in 1820 that an electric current deflects a compass needle. In the 1820s, Michael Faraday established the first "electromagnetic rotation" apparatus. With this system, he proved that electrical energy could be converted into mechanical energy by using a wire rotating around a permanent magnet in a mercury pool.

This device was a laboratory prototype. The real challenge was turning this prototype into a usable machine. In 1825, William

[1] Assist. Prof. Dr., Manisa Celal Bayar Üniversitesi Turgutlu Meslek Yüksekokulu, Elektrik ve Enerji Bölümü, Orcid: 0000-0002-8917-4001

Sturgeon created the first electromagnet, paving the way for more powerful motors. In 1834, Moritz von Jacobi built the first truly functional electric motor. This motor could produce about 15 watts of power and could move a small boat down a river. In 1837, Thomas Davenport received the first electric motor patent in the United States. He used his motor to power a small printing press, but this venture was a commercial failure because batteries were very expensive at the time.

Between 1860 and 1880, the principle of "reversibility" was discovered. A DC generator (dynamo) could function like a motor when electricity was supplied. In 1873, Zénobe Gramme accidentally connected one dynamo to another and observed that the device began to rotate. This was the beginning of the first successful industrial-scale direct current (DC) motor. In 1884, Frank Sprague developed the first practical DC motor that did not produce a spark and operated at a constant speed. This invention paved the way for electric elevators and streetcars.

DC motors had a limited range. The invention of alternating current (AC) motors changed everything. This period is the most critical phase that determined the energy of the modern world. In 1888, Nikola Tesla introduced the multi-phase alternating current system and the induction motor (asynchronous motor). This brushless motor was much more durable and efficient. The competition between Thomas Edison (DC) and Nikola Tesla/George Westinghouse (AC) ended with the victory of the AC system thanks to Tesla's motor being more efficient. Galileo Ferraris independently discovered the principle of rotating magnetic fields around the same time as Tesla. Mikhail Dolivo-Dobrovolsky, in 1889, developed the "Squirrel Cage" three-phase induction motor, the type most widely used in industry today.

The electrification of the global transportation sector has kept electric motor technologies at the centre of academic research over

the last decade. Studies reveal that the period between 2015 and 2025 will be a "technological renaissance" focusing not only on performance but also on raw material sustainability and digitalization. In this context, Gökozan (2020) and Gökozan, H., & Taştan, M. (2019) have presented a critical analysis of traction motors and their corresponding drive topologies based on power storage, highlighting technical specifications for different vehicle segments.

The twentieth century was a period not only of motor growth but also of the development of their controllability. From the 1970s onwards, the development of semiconductors (transistors, drives), which are power electronics materials, allowed for precise control of motor speeds. Brushless DC (BLDC) motors, which reduce friction and extend lifespan, became widespread, used everywhere from computer fans to drones Ziemiański, D., Chwalik-Pilszyk, G., & Dudzik, G. (2025) p: 4630. The discovery of neodymium magnets, made from rare earth elements, in the 1980s enabled the creation of very small but incredibly powerful motors used in electric vehicles (like Tesla's). Table 1 summarizes these developments below.

Table 1. Development of electric motors.

Period	Development	Key Figure
1821	First major transformation	Michael Faraday
1834	First industrial DC motor	Moritz von Jacobi
1888	AC Induction Motor	Nikola Tesla
1960+	Brushless (BLDC) motors	Various Engineers
2010+	High-efficiency EV motors	Modern Automotive Revolution

Source: https://www.telcointercon.com/the-evolution-of-motor

Electric Motors According to Their Application Areas

Electric motors can be classified in various ways according to their structure and application areas.

Industrial and General-Purpose Motors

These motors are the "workforce of factories" where high power and durability are required. Asynchronous (Induction) Motors are the most used type of motor. They are used in water pumps, compressors, conveyor belts, fans, elevators, and general production machinery. Synchronous Motors are used where the speed needs to remain constant regardless of the load, such as in paper and cement factories, large crushing machines, clock mechanisms, and time relays.

Precision Control and Automation Motors

These are preferred in situations where speed, torque, or position needs to be controlled with milimeter precision. Servo motors move very precisely using position feedback (encoder). They are used in robot arms, CNC machines, packaging machines, and medical devices. Stepper motors convert electrical signals into specific step angles. They are used in 3D printers, scanners, photocopiers, and camera focusing systems.

Household and Portable Appliance Motors

These are generally smaller, high-speed, or battery-powered motors. Universal motors are motors that can operate with both AC and DC and can reach very high speeds. They are used in vacuum cleaners, mixers, hair dryers, and hand drills. Brushless DC (BLDC) motors offer high efficiency and quietness. They are used in computer fans, drones, cordless screwdrivers, and new generation washing machines.

Heavy Duty and Traction Motors

These are preferred in applications requiring very high starting torque (starting power). Series DC Motors: Torque increases enormously as the load increases. They are used as starter motors for trains, trams, cranes, and automobiles. Modern electric vehicle

motors are generally specially designed permanent magnet synchronous motors or induction motors. They are used in electric cars and electric buses such as Tesla and Togg.

Asynchronous motors (induction motors) are the most used type of motor in industry. These motors are divided into various groups according to their structure and power supply types.

Classification According to Rotor Structure

Asynchronous motors are divided into two types according to the design of the rotating part (rotor) inside. This distinction is the most important feature that determines the motor's characteristics. Squirrel Cage Asynchronous Motors, the rotor consists of aluminium or copper bars short-circuited at their ends (resembling a squirrel wheel). They are easy to maintain, inexpensive, and durable. 90% of motors in industry are of this type.

Slip Ring (Wound Rotor) Asynchronous Motors, the rotor also has windings like the stator, and these windings are connected to slip rings on the shaft. The starting torque can be increased by adding an external resistor. They are ideal for lifting heavy loads (breakers, large cranes).

Classification According to Number of Phases (Type of Power Supply)

They are divided into two main groups according to the type of electrical network used. Single-Phase Asynchronous Motors: Generally used in homes and small businesses. They cannot start on their own, so they need auxiliary elements such as "capacitors". They are used in washing machines, refrigerators, fans, and small pumps. Three-Phase Asynchronous Motors: Used in industry (380V). They are very powerful and can start rotating on their own. They are used in factory machines, conveyors, elevators, and heavy industrial equipment.

According to Construction Types and Protection Types

The physical structure of the motor may vary depending on the environment in which it will operate. Open Type Motors: These are motors where air flow passes directly through the windings, providing very good cooling, but are not suitable for dusty environments. Closed Type Motors: These are motors where the windings are completely isolated from the external environment, and cooling is provided by fins and a fan on the outer casing. Ex-Proof Motors: These are special motors designed to prevent sparks in places where there is a risk of gas or dust explosions (refineries, mines).

According to Housing and Mounting Type

Floor-Mounted Motors are bolted to the ground or a platform. Flanged Motors have a connecting ring on the front for direct connection to a gearbox (reducer) or machine housing.

Types of Electric Motors

Electric motors basically operate on the principle of electromagnetism and are divided into two main categories according to the type of operating current. However, hybrid operating modes also exist. The basic purpose of each motor is to convert electrical energy into mechanical energy (motion), but the ways they do this and their areas of application are quite different.

DC (Direct Current) Motors

Direct current motors (DC motors) are a well-known type of electric motor that converts electrical energy into mechanical energy (Kuczmann, M. (2024). DC motors are powered by direct current sources (batteries, accumulators, adapters) where the current flows in only one direction. They operate according to the principle of repelling conductors out of a magnetic field due to the current passing through them within a constant magnetic field (Lorentz

Force). In traditional brushed models, mechanical parts called brushes and commutator segments are used to constantly change the direction of the current. Their speed changes proportionally with the voltage. If the voltage increases, the motor speeds up. Therefore, they are very successful in applications requiring precise speed control. They have high starting torques (they start the movement very strongly). However, brushes wear out over time due to friction and require maintenance.

Brushed DC motors are simple in structure and inexpensive (toys, small household appliances). Brushless (BLDC) motors are more efficient, quieter, and longer-lasting, and are used in drones and electric vehicles. They use an electronic controller (ESC) instead of mechanical brushes. They are powered by DC power but manage the current internally as if it were alternating, offering very high efficiency and a long lifespan. Although direct current (DC) motors may seem complex, they work through the perfect harmony of a few basic parts. This structure is like a "magnetic bridge" that allows electricity to be converted into a physical force. As with all motors, the structure of a DC motor is basically divided into two parts: stationary and rotating parts.

Stationary Part

The stationary part is called the stator (inductor) and is the part that forms the outer casing of the motor and the stationary magnetic field. The housing (frame) is the metal enclosure that holds all the parts of the motor together and protects them from external influences. The main poles are where the magnetic field is generated. While permanent magnets are used in small motors, electromagnets with wire wound around them are found in large, powerful motors. The brushes are usually made of carbon (coal). This is because carbon is both a good conductor and, with its soft structure, can "slide" on the rotating commutator without abrading it. They provide

the electrical connection between the stationary external circuit and the rotating rotor. They transmit electricity by contacting the commutator (commutator segments).

Rotating Part

This is called the Rotor (Armor). It is the internal part of the motor that performs the rotational movement and from which mechanical power is obtained. Armature windings are conductive wires wound on grooves on the rotor. When current passes through these wires, it interacts with the magnetic field of the stator, creating rotational force. The Commutator (Commutator) consists of insulated copper segments fixed to the rotor shaft. Its most critical task is to change the direction of the current precisely when the rotor rotates, ensuring that the rotation remains constantly in the same direction. The Shaft is a steel rod that passes through the centre of the rotor and transmits the generated motion to the external gears or propellers. In addition to these, other complementary parts such as bearings and covers ensure that the shaft rotates with minimum friction. Ball bearings are generally used. The cooling fan is a small propeller mounted behind the rotor that expels the heated air inside the motor.

Based on their winding configuration, DC motors are classified as Series Wound Motors, Shunt Wound Motors, and Compound Motors. In Series Wound Motors, the field windings and armature windings are connected in series, producing very high starting torque (power). However, if run unchecked, their speed can increase uncontrollably, damaging the motor. They are commonly used in cranes, elevators, and trains (locomotives). In Shunt Wound Motors, the field windings and armature windings are connected in parallel. Even if the load changes, the speed remains almost constant (constant speed motor). Therefore, they are commonly used in fans, conveyor belts, and drilling machines. Compound Motors combine

both series and shunt winding characteristics. Thus, they have both high starting torque and controlled speed when running unchecked. They are commonly used in heavy industrial machinery with variable loads, such as press machines and rolling mills. Figure 1 shows a cross-section of a brushed DC motor.

Figure 1. Cross-section of a brushed DC motor

Source: https://www.elektrikrehberiniz.com/

Brushless DC Motors (BLDC)

BLDC motors are essentially an "inverted" version of classic DC motors. Unlike brushed motors, the rotor (rotating part) does not have windings. Instead, the rotor consists of permanent magnets with high magnetic attraction Khan, M. A., at all (2025) p:8497. Instead of magnets, coils (windings) are located on the outer fixed part of the stator (stationary part). They generally have a three-phase winding structure. Since the motor has no brushes, it needs an Electronic Speed Controller (ESC) to change the direction of the current Park, S. (2025), p: 481). The ESC acts as a "brain," determining when and to which coil to supply current based on the rotor's position. Some

BLDC motors have small Hall-Effect Sensors that detect the exact position of the rotor and report it to the driver (ESC). This provides high accuracy, especially at low speeds.

Brushless motors create a "rotating magnetic field". The electronic driver sends current to the stator windings sequentially, creating a magnetic attraction/repulsion force Taş, G., & Özdamar, M. (2025) p:140. The permanent magnets on the rotor follow this moving field and begin to rotate. Because there are no brushes, no electrical arc (spark) is formed, and friction loss is minimized.

Figure 2. Brushless DC motor

Source: (https://www.kontrolkalemi.com/fircasiz-dc-motor-brushless-motor/)

Special Purpose DC Motors

Special purpose DC motors are stepper and servo motors.

Stepper Motors

Stepper motors rotate step by step. They are used in 3D printers where precise positioning is required. If a motor can perform mechanical movement (i.e., rotation) when electrical pulses are applied to it, these types of motors are called stepper motors. In short,

they are motors that convert digital information into mechanical movement, i.e., they act as transducers. When an electric motor is energized, its rotors rotate continuously. For this rotation to stop, the energy must be cut off. However, this is different in stepper motors. The stator of a stepper motor has many poles (usually eight). Their polarity is changed using electronic switches. As a result of switching, the south and north poles of the stator are rotated. The south pole of the rotor and the north pole of the stator are in sequence.

The rotor's magnetism can be created using a permanent magnet or external excitation methods. A permanent magnet will be formed in this process. When an input pulse is applied to a stepper motor, it rotates a certain amount and stops. This amount of rotation is limited by a certain angle depending on the motor's design. In a stepper motor, the rotor's rotation changes depending on the number of pulses applied to the input. When a single pulse is applied, the rotor moves one step and stops. When more pulses are applied, it moves as many steps as the number of pulses. This is the working principle of all stepper motors.

There are some terms used in stepper motors. These are:

- **Step Angle (SA):** This is an angular rotation in degrees, where the shaft rotates with each change in winding polarity. This is achieved with a single input pulse. It is expressed in degrees/step or simply in degrees.
- **Step Per Revolution (SPR):** This indicates the total number of steps required for a full 360° rotation. SPR = 360° / SA
- **Step Per Second (SPS):** The number of angular steps the motor travels in 1 second, comparable to the rotational speed per minute of A.C. and D.C. motors.

  SpS = SPR (r/min)/60 or w = 2 Pi (SPS / SPR) rad/s.

- **Driver Circuit:** This is a general term defined in electronics for motor control. It usually consists of components such as a power supply, sequential logic, and power switching.

Figure 3. Stepper motor and driver circuit

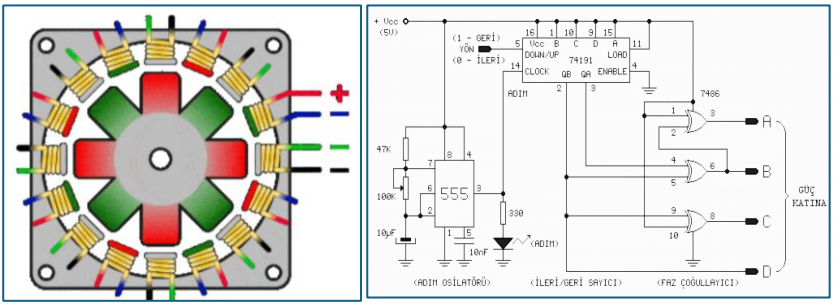

Source: https://www.bozukdevre.net/

A wide variety of stepper motors have been manufactured, including permanent magnet stepper motors (PM), variable reluctance stepper motors (VR), hybrid stepper motors, hydraulic stepper motors, and linear stepper motors. The simplest permanent magnet stepper motor consists of a two-pole permanent magnet rotor rotating inside a four-pole stator with slots. Variable reluctance (VR) stepper motors, like permanent magnet stepper motors, have at least a four-pole stator. The only difference from permanent magnet stepper motors is that the rotor is made of non-residual magnetized, non-permanent magnetized, and is made of toothed soft iron. The teeth are formed in grooves parallel to the cylinder axis. They come in single-piece and multi-piece versions.

Hybrid stepper motors are an improved version of permanent magnet and variable reluctance stepper motors. Stepper motors that control the pressure inlet path of a servo valve belonging to a hydraulic motor with translators (rotary linear converters) are called hydraulic stepper motors. In short, stepper motors that determine the movement and direction of the shaft by controlling the pressurized

oil path of the hydraulic motor are called hydraulic stepper motors. Hydraulic stepper motors are also called electro-hydraulic stepper motors. Motors whose mechanical motion is not circular but moves along a horizontal axis (x or y axes) are called linear motors. That is, linear motors move in the X and Y directions or in any vector direction in the X and Y plane. These types of motors contain two orthogonal electromagnetic fields on a housing. To complete this field, the iron core is made square. Thus, a two-axis linear stepper motor is created.

Stepper motors are used in conveyor belts, manufacturing machines, printers, tape drives, memory processing, medical devices, machine tools, sewing machines, cameras, taximeters, card readers, adjustment and control technology, and remote-control displays. In short, stepper motors act as transducers, converting digital information into mechanical motion wherever controlled movement or positioning is required.

DC Servo Motors

They are manufactured in two different ways that can operate on both DC and AC voltages. DC servo motors are special types of motors that operate with direct current (DC) and are used in mechanisms requiring high-precision speed, position, and torque control. The biggest difference from a standard DC motor is that it operates in a "closed loop" system thanks to a feedback mechanism. The basic characteristics of DC servo motors are precision, high torque, fast response, size, and power. They are widely used in robotics, CNC machines, aerospace, medical devices, and automation systems.

DC servo motors are not only a motor, but a combination of four main components. The DC motor converts electrical energy into mechanical motion. The feedback sensor (encoder/potentiometer) measures the current position or speed of the motor shaft. The gear

mechanism (reducer) reduces speed to increase torque and improve precision. The control circuit corrects the motor's movement by calculating the difference (error signal) between the target position and the actual position.

AC (Alternating Current) Motors

AC motors operate with alternating current, whose direction and intensity are constantly changing. The alternating current flowing into the windings in the stator (stationary part) creates a rotating magnetic field. This field forces the rotor in the center to rotate along with it. In the most common type, the "Asynchronous (Induction) Motor," there is no physical contact between the rotor and the magnetic field; the movement is entirely due to magnetic induction. As with asynchronous motors, the speed in synchronous motors depends on the frequency (Hz) of the current.

Additional devices such as frequency converters (inverters) are required to change the speed. Alternating current motors are very durable. Because they do not contain brushes like conventional DC motors, they require almost no maintenance. Most of the giant machines in industrial facilities are AC motor driven. In addition, they are commonly used in household appliances (washing machines, refrigerators).

Alternating current (AC) motors are simpler, more durable, and easier to maintain than DC motors. They basically consist of two main parts and supporting auxiliary parts.

Housing and Stator (Fixed Part)

The outermost fixed part of the motor is called the housing and carries the entire motor. It is usually made of aluminum or cast iron. The fins on it help cool the motor. The stator is formed by pressing thin, silicon steel sheets together to reduce magnetic losses. Stator windings are copper or aluminum wires placed in slots inside

the stator. When alternating current passes through these windings, magnetization occurs, and the poles constantly shift, creating a rotating field.

Rotor (Rotating Part)

This is the part that rotates within the magnetic field created by the stator. There are two main rotor structures depending on the type of AC motor. The Squirrel Cage Rotor is the most common. It consists of copper or aluminum rods placed in grooves opened on sheet metal packages and short-circuited at their ends. It gets its name because its structure resembles a "squirrel wheel". In the Wound (Slip Ring) Rotor, there are also actual windings on the rotor. These winding ends can be connected to external resistors, thus adjusting the starting torque of the motor.

Auxiliary Components

The air gap is the very thin space between the stator and the rotor. Magnetic fluxes pass through this gap. For efficiency, this gap should be as narrow as possible. Bearings and roller bearings ensure that the rotor shaft rotates with minimum friction.

The cooling fan is attached to the rear end of the shaft and provides air circulation to dissipate internal heat while the motor is running. The terminal box is the box where the cables from the mains are connected to the motor. The motor connection adjustment is made here.

They are manufactured in both single-phase and three-phase versions. There is no difference in their structure, only in their windings. Single-phase AC motors are the most common type of motor we encounter in our homes and small workshops. Refrigerators, washing machines, fans, and small pumps operate with these motors. They are very similar to three-phase motors, but their biggest difference is in the stator windings.

Single-Phase AC Asynchronous Motors

Single-phase AC asynchronous motors have two types of windings inside the stator: the main winding and the auxiliary winding. The main winding consists of thick wires and is in operation throughout. The auxiliary winding is made of thin wires. It is placed at a 90° electrical angle to the main winding to enable the motor to start. The rotor (rotating part) usually has a squirrel cage structure. Instead of windings, there are aluminum bars short-circuited together. The capacitor is connected in series with the auxiliary winding. It creates a phase difference between the current and voltage, generating the motor's starting torque. The centrifugal switch is a mechanical switch that disconnects the auxiliary winding when the motor reaches a certain speed (usually 75% of full speed).

The most interesting feature of single-phase asynchronous motors is that they cannot start on their own. When AC current is applied to a single-phase winding, only a pulsating magnetic field is created, not a "rotating" magnetic field. This field tries to pull the rotor from side to side, but since the rotor is stationary, no net rotational force is generated. The auxiliary winding and its connected capacitor shift the phase of the current from the mains. In this way, an "artificial" rotating magnetic field is created in the stator. The rotating magnetic field induces current in the rotor bars (Faraday's Law). The rotor also creates its own magnetic field and begins to follow the rotating field of the stator. Once the motor starts, the auxiliary winding is no longer needed. The centrifugal switch snaps, disconnecting the auxiliary winding and the starting capacitor. The motor then continues to rotate with only the main winding.

The most common types are Motors with auxiliary windings, where the auxiliary winding is used only at the start. Motors with permanent capacitors have both the capacitor and auxiliary winding continuously in the circuit (like in fans). Motors with dual capacitors are advanced models that provide both high power at start and high

efficiency during operation, using two capacitors (start and run). Single-phase motors are not limited to capacitor-based asynchronous motors. There are many different types of single-phase AC motors depending on the application, torque requirement, and cost. Other common types of single-phase motors include:

Universal Motors (AC/DC Motors)

These motors are called "universal" because they can operate with both alternating current (AC) and direct current (DC). Structurally, they are very similar to DC series motors (they are brushed and commutated). They can reach very high speeds (20,000+ RPM) and have very high starting torque. However, because they are brushed, they operate noisily and require maintenance. They are used in vacuum cleaners, drills, mixers, hair dryers, etc.

Figure 4. Universal motor

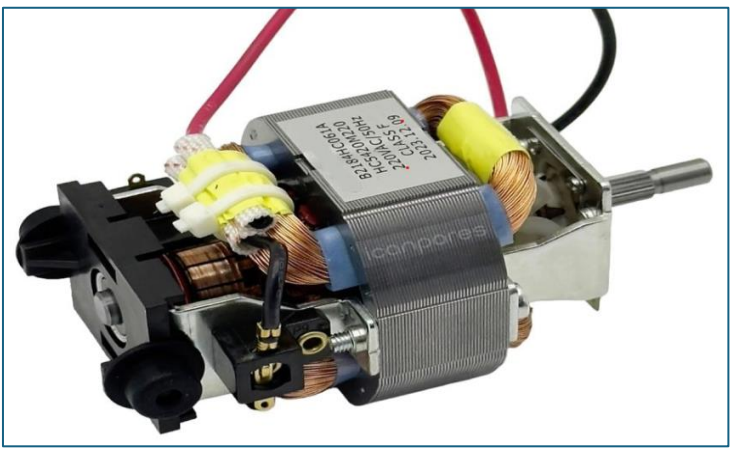

Source: https://www.icanpares.com/cv

Shaded Pole Motors

This is the simplest and cheapest type of motor. Instead of an auxiliary winding or capacitor, copper rings (shade coils) placed at

one corner of the main poles are used. The copper ring creates a "sliding" magnetic field by creating a delay in that part of the main magnetic field. This weak field causes the rotor to rotate. Their efficiency is very low, and their starting torque is weak. However, they are very cheap and durable. They are commonly used in applications requiring low power, such as small cooling fans, oven interior lighting fans, and juicers.

Repulsion Motors

The stator has AC windings, and the rotor is wound and commutated like a DC motor rotor. The brushes are short-circuited. The starting torque is one of the highest among all 1-phase motors. Speed and direction can be controlled by changing the angle of the brushes. Today, it has largely been replaced by driver-controlled motors.

Three-Phase AC Asynchronous Motors

Three-phase asynchronous motors are widely used in industry. They are called "asynchronous" because when converting electrical energy into mechanical energy, the rotor speed is always slightly slower than the rotational magnetic field speed of the stator (synchronous speed). The motor basically consists of two main parts, as in single-phase asynchronous motors. The stator is the stationary part and has three separate phase windings with an electrical angle of 120° between them. When current is applied, this part creates the rotating magnetic field.

The rotor (moving part) can have two different structures, like the rotor of a single-phase asynchronous motor. The squirrel cage rotor is formed by short-circuiting aluminium or copper bars at the ends. It is the most common type, very durable and maintenance-free. The slip ring (wound) rotor also has windings, and these windings can be connected to external resistors. It is preferred where high starting torque is required.

Figure 5. Cross-section of a 3-phase asynchronous motor.

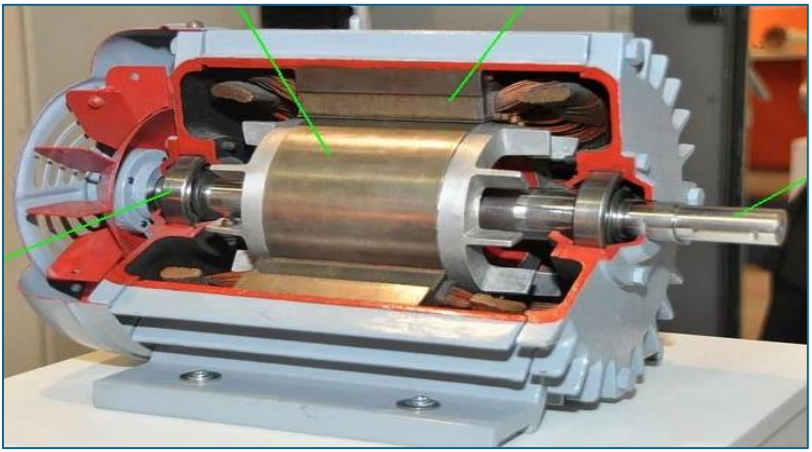

Source: https://www.automationtr.com/as

When 3-phase AC is applied to the stator windings, a magnetic field is created within the stator that rotates at synchronous speed (Ns). This rotating field cuts the stationary rotor bars, inducing a voltage (EMF) there. The induced current creates its own magnetic field. According to Lenz's Law, the rotor begins to rotate, trying to catch up with the stator field that created it. The rotor can never reach synchronous speed. If it did, the torque would drop to zero because the magnetic field lines would not be cut. This speed difference is called slip.

$$Ns = 120xf/2p$$

(Here, f is the frequency and 2P is the number of poles.)

The motor terminal box contains the winding ends (U-V-W and X-Y-Z). There are two connection types depending on the motor's mains voltage. Star (λ) connection provides low voltage and low current. It is generally used for starting the motor initially. Delta (Δ) connection provides full power and torque. This connection is used after the motor has reached its speed.

Star-Delta Starting is large motors draw 5-7 times the normal current from the mains during startup. To prevent this, the motor is first started with a Star connection and then switched to Delta once it has accelerated.

Three-phase asynchronous motors are preferred because they are simple, economical, efficient, and their speed can be controlled with various starters and frequency converters.

Figure 6. Asynchronous motor and terminal connection.

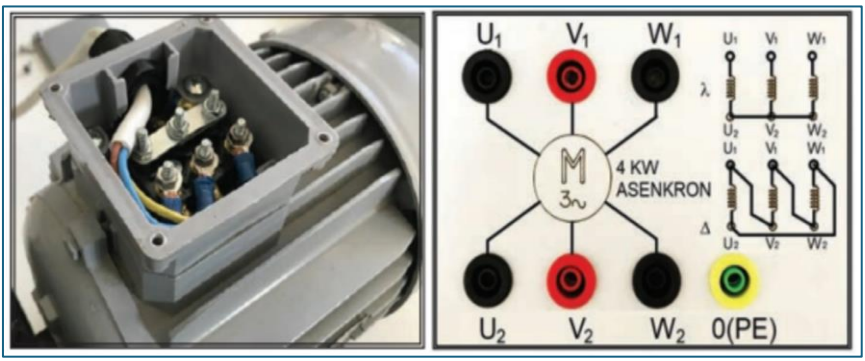

Source: https://www.electricistanbul.com/2023

Commonly Used Motors in Electric Vehicles

Motors used in electric vehicles (EVs) are technologies that provide much higher efficiency (90%+) and instantaneous torque compared to internal combustion engines. The motor unit (system architecture) of an electric vehicle is not just the motor; a structure called "3-in-1" is usually used. The inverter converts the DC (Direct Current) electricity from the battery into AC (Alternating Current) electricity that the motor can understand. This is where the motor's speed and torque are controlled. The motor converts the electricity into motion. The gearbox is a single stage fixed gearbox that reduces the speed of electric motors, which can reach very high speeds such

as 15,000-20,000 RPM, before transmitting it to the wheels. In today's automotive industry, three main types of motors stand out.

Permanent Magnet Synchronous Motors (PMSM)

This is the most popular type of motor used in most modern electric vehicles (e.g., the rear motor of the Tesla Model 3, Hyundai Ioniq 5). It has very powerful magnets made of rare earth elements in its rotor. It offers very high efficiency, compact size and light weight. It provides high torque even at low speeds. However, the raw materials required for magnet production (such as neodymium) are costly and strategically difficult to obtain.

Three-Phase Asynchronous (Induction) Motors

These are the motors that started the electric vehicle revolution. They were widely used in the first versions of the Tesla Model S and Model X. There is no magnet in the rotor; the current passes through the stator windings and induces a magnetic field on the rotor. They are very durable, inexpensive, and do not require magnets. They are quite efficient at high speeds (highway driving). They can be slightly heavier and larger than Permanent Magnet Synchronous Motors; also, their efficiency may decrease somewhat at low speeds.

Brushless DC Motors (BLDC)

They are mostly preferred in small electric vehicles (electric bicycles, scooters, and some microcars). They are like synchronous motors but have a different control method (trapezoidal waveform). They require no maintenance, have a long lifespan, and are relatively easy to control. They may not provide as smooth a ride as synchronous motors in passenger cars requiring high power.

The reason these motors are chosen for electric vehicles is Regenerative Braking, Zero Emissions, and Acceleration. All these motors act like a generator when you take your foot off the

accelerator, converting the vehicle's kinetic energy into electricity and charging the battery. This results in energy recovery. Traditional brakes waste kinetic energy by converting it into heat. The regenerative system converts this energy into electricity instead of heat, preventing the system from overheating Ayhan D., Bakbak A. (2025), p: 236. Traditional pad brakes are only used in emergencies. Because normal deceleration is achieved by the "magnetic resistance" created by the motor, brake pads last 3-4 times longer than those in internal combustion vehicles. They do not release any exhaust gases while operating and do not wait for revving like internal combustion engines; they deliver maximum torque instantly at the pedal.

References

Ayhan D., Bakbak A., “Hafif Elektrikli Araçlar İçin Araç Modeli ve Sürüş Döngüsüne Göre Elektrik Motoru Tasarımı” Int. J. of 3D Printing Tech. Dig. Ind., 9(2): 236-246, (2025). DOI: 10.46519/ij3dptdi.1630021

Gökozan, H. (2020). Traction Motors and Motor Drivers Used in Electric Vehicles. European Journal of Science and Technology (19), 105-111. https://doi.org/10.31590/ejosat.699699

Gökozan, H., & Taştan, M. (2019). Autonomous road vehicles and electrical-electronic equipment, Research & Reviev in Engineering–Summer 261

Khan, M. A., Baig, D. E. Z., Ali, H., & Albogamy, F. R. (2025). Optimized system identification (SI) of brushless DC (BLDC) motor using data-driven modeling methods. *Scientific Reports*, *15*(1), 8497. https://doi.org/10.1038/s41598-025-93444-0

Kuczmann, M. (2024). Review of DC Motor Modeling and Linear Control: Theory with Laboratory Tests. Electronics, 13(11), 2225. https://doi.org/10.3390/electronics13112225

Park, S. (2025, October). Development of a 3D-Printed BLDC Motor and Controller for Robotic Applications. In *Actuators* (Vol. 14, No. 10, p. 481). https://doi.org/10.3390/act14100481

Taş, G., & Özdamar, M. (2025). Estimation of PID parameters of BLDC motor system by using machine learning methods. *Signal, Image and Video Processing*, *19*(2), 140. https://doi.org/10.1007/s11760-024-03714-z

Ziemiański, D., Chwalik-Pilszyk, G., & Dudzik, G. (2025). Analysis of Stator Material Influence on BLDC Motor Performance. Materials, 18(19), 4630. https://doi.org/10.3390/ma18194630

https://www.automationtr.com Erişim Tarihi Kasım 2025
https://www.bozukdevre.net/ Erişim Tarihi Kasım 2025
https://www.electricistanbul.com/2023/ Erişim Kasım 2025
https://www.elektrikrehberiniz.com/ Erişim Kasım 2025
https://www.icanpares.com/cv Erişim Tarihi Aralık 2025
https://www.kontrolkalemi.com/ Erişim Tarihi Aralık 2025
https://www.telcointercon.com/the-evol. Erişim Aralık 2025

CHAPTER 2

ADVANCED ANTENNA TECHNOLOGIES FOR MODERN RADAR SYSTEMS: ACTIVE ELECTRONICALLY SCANNED ARRAYS (AESA) AND METAMATERIAL-BASED SOLUTIONS

LEVENT SEYFİ[1]

Introduction

The antenna subsystem remains the dominant performance-limiting element in modern radar systems, particularly in multifunctional and spectrum-contested operational environments. Recent radar architectures increasingly rely on adaptive, software-defined antenna apertures capable of real-time reconfiguration in response to mission dynamics, interference, and platform constraints (Skolnik, 2008; Mailloux, 2018; Aboelazm, 2025).

The classical radar range equation,

$$R_{max} = \left(\frac{P_t G^2 \lambda^2 \sigma}{(4\pi)^3 S_{min}} \right)^{\frac{1}{4}}$$

[1] Prof.Dr., Konya Technical University, Electrical and Electronics Engineering, Orcid: 0000-0002-8698-5140

explicitly highlights the quadratic dependence of detection range on antenna gain (G). Consequently, even incremental improvements in array efficiency, sidelobe suppression, or adaptive beam control yield disproportionate system-level benefits (Mahafza, 2017).

In contemporary radar systems, antennas must simultaneously satisfy stringent requirements on beam agility, polarization diversity, instantaneous bandwidth, low probability of intercept (LPI), and electromagnetic survivability. These demands have accelerated the transition from mechanically scanned antennas to Passive Electronically Scanned Arrays (PESAs), and ultimately to fully Active Electronically Scanned Arrays (AESAs) with digital beamforming capabilities (Brookner, 2017; Kwon & Park, 2025).

Parallel to these developments, metamaterial and metasurface technologies have emerged as transformative enablers for antenna miniaturization, low-RCS radome design, and compact beam-steering solutions. Recent studies demonstrate that metasurface-assisted AESA apertures can achieve simultaneous improvements in bandwidth, angular stability, and electromagnetic stealth (Caloz & Itoh, 2006; Glybovski et al., 2016; Mirzapour et al., 2024).

Passive and Active Electronically Scanned Arrays (PESA/AESA): A Comparative Analysis

Beam Steering Fundamentals: For a uniformly spaced linear array, the progressive phase shift required to steer the main beam toward angle (θ_0) is given by

$$\Delta\phi = -kdsin\,\theta_0$$

where ($k = \frac{2\pi}{\lambda}$) and (d) denotes the inter-element spacing (Balanis, 2016).

In PESA architectures, this phase progression is imposed via centralized passive beamforming networks. While effective for rapid beam steering, PESAs inherently lack element-level adaptability and are constrained in terms of waveform agility and interference suppression (Skolnik, 2008).

AESA Architecture and System-Level Advantages: Figure 1 conceptually contrasts PESA and AESA architectures. In AESAs, each radiating element integrates a dedicated T/R module, enabling distributed control of phase, amplitude, frequency, and polarization.

Figure 1. Conceptual comparison of PESA and AESA architectures

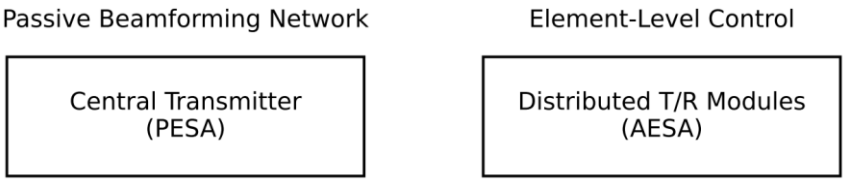

Recent 2025-era AESA implementations increasingly adopt tile-based digital subarrays, allowing scalable apertures with enhanced maintainability and fault tolerance (Brandfass et al., 2019). This distributed intelligence enables graceful degradation and supports mission continuity under partial hardware failure.

Performance Comparison: Compared to PESAs, AESAs offer:

- Pulse-to-pulse frequency agility,
- Adaptive null steering against dynamic jammers,
- Multi-beam and multi-function operation,
- Improved LPI characteristics.

However, these benefits come at the cost of increased thermal density, power consumption, and calibration complexity, necessitating advanced thermal management and embedded health-monitoring systems (Herd & Conway, 2015; Aboelazm, 2025).

AESA Radar Components: Phase Shifters, Signal Processors, and T/R Modules

Phase Shifters and True-Time Delay Networks: Wideband AESA radars increasingly employ true-time-delay (TTD) units to mitigate beam squint effects inherent in frequency-dependent phase shifters. The squint angle can be approximated by

$$\Delta\,\theta \approx tan^{-1}(\frac{\Delta\,f}{f_0} tan\,\theta_0)$$

highlighting the necessity of TTD architectures for ultra-wideband radar applications (Mailloux, 2018).

T/R Modules and GaN MMIC Technologies: Modern T/R modules integrate power amplifiers, low-noise amplifiers, variable attenuators, phase shifters or TTD units, and digital control logic. The widespread adoption of GaN-on-SiC MMIC technologies has significantly enhanced power density, efficiency, and radiation hardness.

Recent experimental results reported in IEEE Transactions on Microwave Theory and Techniques (2025) demonstrate GaN-based T/R modules achieving >60% power-added efficiency at X- and Ku-band frequencies (Hu et al., 2025).

Digital Beamforming and Signal Processing: Figure 2 illustrates a fully digital AESA radar block diagram, wherein each antenna element is followed by an RF-to-digital conversion chain.

Figure 2. Block diagram of a fully digital AESA radar system

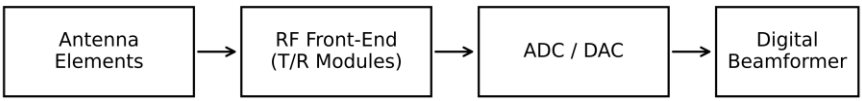

Beamforming is performed using complex weight vectors.

$$\boldsymbol{w} = [w_1, w_2, \ldots, w_N]^T$$

enabling adaptive algorithms such as MVDR and STAP for interference and clutter suppression (Van Trees, 2002; Ward, 1998).

Metamaterial-Based Radome and Beam-Steering Design: Low RCS and Wideband Performance

Metamaterial Electromagnetic Properties: Metamaterials exhibit engineered effective permittivity (ε_{eff}) and permeability (μ_{eff}), yielding a refractive index

$$n = \sqrt{(\varepsilon_{eff}\mu_{eff})}$$

Negative or anisotropic refractive indices enable unconventional wave manipulation mechanisms such as backward propagation and subwavelength focusing (Pendry, 2000; Veselago, 1967).

Metamaterial Radomes for AESA Systems: Figure 3 depicts a multilayer metamaterial radome designed for broadband transmission and angular stability. Recent studies demonstrate that metasurface-based radomes can simultaneously reduce in-band insertion loss and out-of-band RCS by more than 40% (Mirzapour et al., 2024).

Figure 3. Multilayer metamaterial-based radome structure

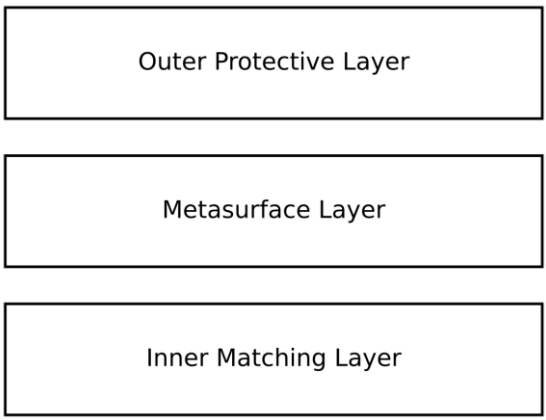

Metasurface-Assisted Beam Steering: Metasurfaces provide spatially varying phase discontinuities, enabling compact beam-steering without bulky feed networks. Hybrid AESA–metasurface architectures reported in 2025 show promising reductions in system size, weight, and power (SWaP), particularly for airborne radar platforms (Wang et al., 2025).

Simultaneous Multi-Beam Formation in Multifunction AESA Arrays

Multifunction AESA radars exploit digital beamforming to generate multiple independent beams concurrently. The array output can be expressed as

$$y(t) = \sum_{m=1}^{M} \boldsymbol{w}_m^H \boldsymbol{x}(t)$$

where (M) denotes the number of simultaneous beams.

Figure 4 illustrates a conceptual multi-beam AESA operational scenario supporting surveillance, tracking, and communication functions simultaneously (Herd & Conway, 2015).

Figure 4. Simultaneous multi-beam operation in an AESA aperture

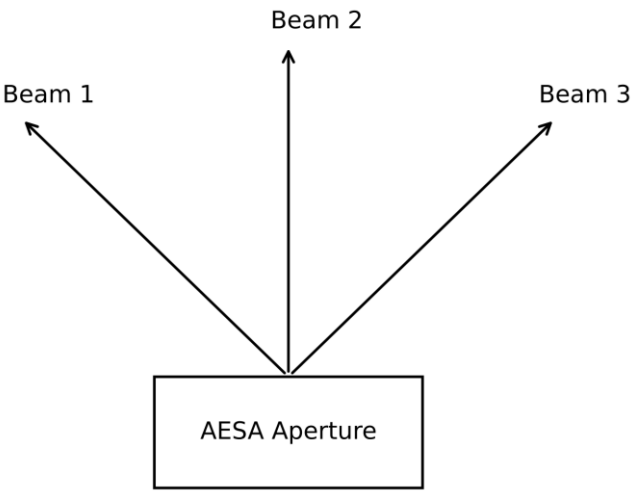

Manufacturing Technologies and Test Methods (PCB, MMIC)

AESA fabrication relies on advanced multilayer RF PCBs, low-loss substrates, and high-yield MMIC processes. Thermal management is addressed using embedded heat spreaders, vapor chambers, and liquid cooling solutions (Pozar, 2011).

Figure 5 presents a typical AESA tile integrating RF, digital, and thermal subsystems.

Figure 5. Modular AESA tile architecture

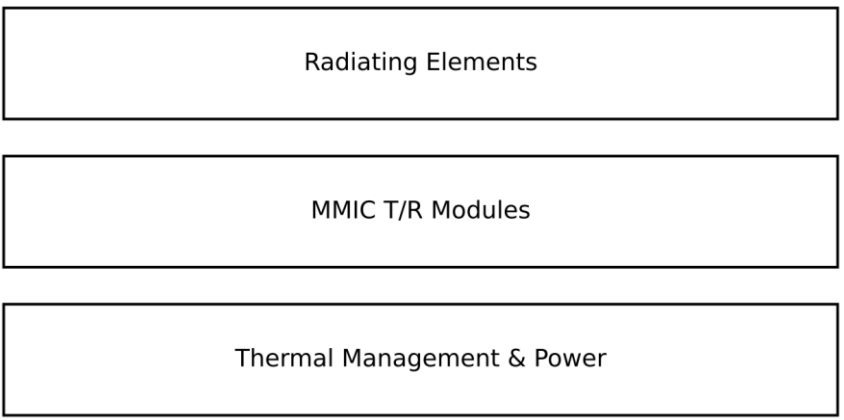

Advantages and Resilience of AESA in Electronic Warfare Environments

AESAs provide inherent advantages in EW environments through adaptive nulling, frequency agility, and waveform diversity. The output jammer-to-signal ratio is given by

$$JSR_{out} = \boldsymbol{w}^H \boldsymbol{R}_j \boldsymbol{w}$$

where $\boldsymbol{R}_j$ is the jammer covariance matrix (Ward, 1998).

Recent studies indicate that AI-assisted adaptive nulling can improve jammer suppression by more than 15 dB in dense EW scenarios (Sfetcu, 2024).

Future Trends

Digital Phased Array Radar and AI-Assisted Beam Management

The convergence of fully digital phased arrays and artificial intelligence is shaping next-generation radar systems. Cognitive radar frameworks leverage machine learning to adapt beam patterns, waveforms, and resource allocation in real time (Haykin, 2006; Guerci, 2014).

Figure 6 shows a high-level block diagram of an AI-assisted cognitive AESA radar. Recent experimental demonstrations confirm the feasibility of real-time AI-driven beam scheduling in operational radar prototypes (Aboelazm, 2025).

Figure 6. AI-assisted cognitive AESA radar architecture

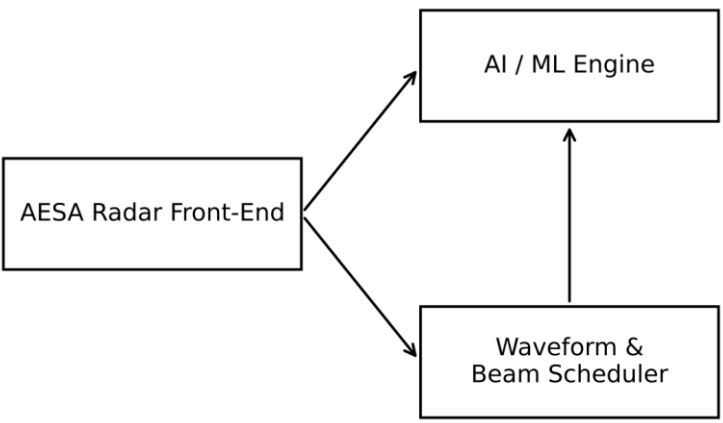

References

Aboelazm, M. A. (2025, July). Integration of AI-Driven Electronic Warfare Radio Monitoring Systems with Antenna Array Direction Finding for Advanced Signal Classification and Localization. In *2025 International Telecommunications Conference (ITC-Egypt)* (pp. 503-508). IEEE.

Balanis, C. A. (2016). *Antenna theory: Analysis and design* (4th ed.). Wiley.

Brandfass, M., Boeck, M., & Bil, R. (2019, October). Multifunctional aesa technology trends-a radar system aspects view. In *2019 IEEE International Symposium on Phased Array System & Technology (PAST)* (pp. 8138-8143). IEEE.

Brookner, E. (2017). *Phased-array radars*. SciTech Publishing.

Caloz, C., & Itoh, T. (2006). *Electromagnetic metamaterials*. Wiley.

Glybovski, S. B., et al. (2016). Metasurfaces: From microwaves to visible. *Physics Reports*, *634*, 1–72.

Guerci, J. R. (2014). *Cognitive radar*. Artech House.

Haykin, S. (2006). Cognitive radar: A way of the future. *IEEE Signal Processing Magazine*, *23*(1), 30–40.

Herd, J. S., & Conway, M. D. (2015). The evolution to modern phased array architectures. *Proceedings of the IEEE*, *104*(3), 519-529.

Hu, C. J., Li, H. Y., Xu, J. X., Chen, R. F., Zhu, J. M., & Zhang, X. Y. (2025, June). A 24–30 GHz GaN-on-SiC T/R Front-End Module with 37.1-dBm Output Power and 34.4% PAE. In *2025 IEEE Radio Frequency Integrated Circuits Symposium (RFIC)* (pp. 195-198). IEEE.

Kwon, J., & Park, H. (2025). AI-enabled adaptive beamforming for resilient AESA radars in electronic warfare environments. *IEEE Aerospace and Electronic Systems Magazine, 40*(1), 22–35.

Mahafza, B. R. (2017). *Radar systems analysis and design*. CRC Press.

Mailloux, R. J. (2018). *Phased array antenna handbook* (3rd ed.). Artech House.

Mirzapour, M. I., Ghorbani, A., & Azadi Namin, F. (2024). Metasurface radome to achieve a wideband high gain, low RCS, and low SLL antenna. *IETE Journal of Research*, *70*(1), 206-213.

Pendry, J. B. (2000). Negative refraction makes a perfect lens. *Physical Review Letters, 85*(18), 3966–3969.

Pozar, D. M. (2011). *Microwave engineering* (4th ed.). Wiley.

Sfetcu, N. (2024). *Electronic Warfare and Artificial Intelligence*. MultiMedia Publishing.

Skolnik, M. I. (2008). *Radar handbook* (3rd ed.). McGraw-Hill.

Van Trees, H. L. (2002). *Optimum array processing*. Wiley.

Veselago, V. G. (1967). The electrodynamics of substances with simultaneously negative values of ε and μ. *Usp. fiz. nauk*, *92*(3), 517-526.

Wang, L., Lan, F., Cong, X., Song, T., Yang, M., Li, Y., ... & Yang, Z. (2025). Reflection-enhanced terahertz beam steering via a backside-driven metasurface enabled by dielectric-superstrate matching. *Optics Express*, *33*(17), 35958-35969.

Ward, J. (1998, April). Space-time adaptive processing for airborne radar. In *IEE Colloquium on Space-Time Adaptive Processing* (pp. 1-6). London UK: IEE.

CHAPTER 3

ELECTROMAGNETIC MODE ANALYSIS IN MICROWAVE RESONATORS: A COORDINATE SYSTEM-BASED APPROACH

Baran Aras[1]
Selçuk Alparslan Avci[2]

Introduction

From modern communication systems to sensing and measurement applications, electromagnetic (EM) mode structures operating in microwave frequency bands are utilized in many fields. For the design and analysis of these structures, accurate modeling is needed to describe the spatial behavior of the EM fields. The microwave resonator is one of the fundamental building blocks in this field because they can store the EM energy at certain frequencies, thus controlling the fields. The modes which the resonator supports decide directly the EM principle of the microwave resonators and, consequently, the resonance frequencies associated with them. Overall, to solve the problem of EM modes,

[1] Lecturer, Cankiri Karatekin University, Vocational School, Department of Electrical and Energy, Orcid: 0000-0001-7694-9165
[2] Asst.Prof., Karabuk University, Faculty of Engineering and Natural Sciences, Department of Electrical and Electronics Engineering, Orcid: 0000-0003-4918-5272

Maxwell equations are applied along with suitable choice of the coordinate system and appropriate choice of the boundary conditions along with selection of resonator geometry. The coordinate system chosen has a direct effect on the mathematical expression as well as on the separability of the solution and on the complexity of the resulting distributions of EM fields and on how resonance frequencies are to be calculated. Mode analysis of microwave resonators must, thus, be regarded in the context of geometry, coordinate system and solution structure. In many microwave resonator-related studies published in the literature, the decisive influence of a coordinate system in analyzing modes is usually discussed indirectly. No systematic comparison is pursued. In this book chapter, the systematic inspection of the EM mode analysis is realized using the coordinate system approach holistically: Rectangular, cylindrical, and spherical cavity resonators are considered as examples. Supported by analytical solutions, numerical calculations, and limited visualizations, a clear demonstration is performed regarding the effect that the selection of coordinate system exerts on the EM behavior of microwave resonators.

The Concept and Basic Principles of Microwave Resonators

Microwave resonators are EM structures with a specific geometry that trap EM energy at microwave frequency levels within a closed volume, allowing the formation of wave modes that remain stable only at discrete resonance frequencies (Yang, Leon Bennett, Calisir, Xiao, & Huang, 2024). EM structures of a particular geometry that confines EM energy in microwave frequency levels in a closed volume can support discrete electromagnetic wave modes, which can only be maintained in discrete resonance frequencies (Yang, Leon Bennett, Calisir, Xiao, and Huang, 2024). According to Maxwell equations, a system that is able to operate only at specific frequencies when the relevant boundary conditions are met is known

as a microwave resonator. The basis of the resonator concept is that an EM wave is reflected multiple times in a closed or semi-closed space, reinforcing at some frequencies and attenuating unwanted frequency components. This process of constructive and destructive interference is referred to as resonance. Therefore, microwave resonators are primarily used to achieve resonance. The performance of microwave resonators depends on the geometry and applied boundary conditions, as well as the dielectric and magnetic permeability of the materials used (Sheng, Xiong, Hao, & Wang, 2020).

Microwave resonators can be broadly categorized into two main groups: three-dimensional metal-walled cavity resonators and two-dimensional planar (microstrip, ring, etc.) resonators (Collin, 2007; Pozar, 2012). Figure 1 shows the basic groups and their operating principles. Cavity resonators generally have rectangular, cylindrical, or spherical geometries and possess high energy storage capabilities with high quality factor (Q) values (Jackson, 2021). Planar resonators, on the other hand, are widely used in communication circuits, sensing systems, and integrated RF applications due to their more compact structure. One of the most important performance parameters of a microwave resonator is the quality factor (Q) (Alahnomi et al., 2021). The Q factor is a measure of the ratio between the energy stored in the resonator and the energy lost in one period, and it determines the sharpness of the resonance curve. Resonators with high Q values operate in a narrow band and are quite sensitive to frequency variations (Pozar, 2012). This feature enables resonators to be widely used in sensor applications. As a result, microwave resonators are one of the fundamental system elements in many important applications such as frequency selection, signal filtering, stable oscillator generation, EM field concentration, and sensing (Pozar, 2012). Mode analysis, resonance frequency calculations, and field distribution solutions are important

for accurately modeling the EM behavior of resonators (Collin, 2007).

Figure 1. Basic Types and Operating Principles of Microwave Resonators

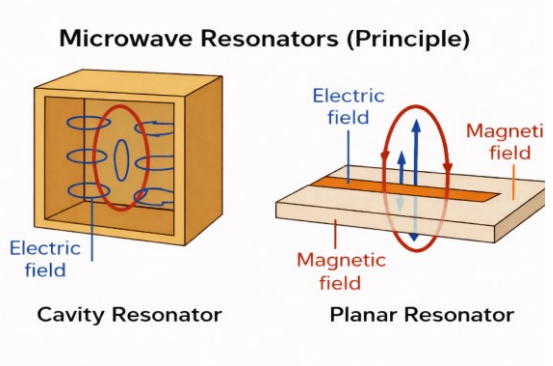

Electromagnetic Mode Concept

EM waves do not propagate randomly in structures with boundary conditions, such as a resonator, as they do in free space. Depending on the geometry of the resonator system and the EM boundary conditions, they can only take on specific field distributions (Zou et al., 2023). These stable spatial distributions of EM fields are called EM modes. Each mode is a solution within the resonator where the electric and magnetic fields are distributed in a specific spatial order, possessing its own resonance frequency. These modes are commonly classified as TE (Transverse Electric) mode, TM (Transverse Magnetic) mode, and TEM (Transverse Electromagnetic) mode (Pozar, 2012). TEM modes do not occur in closed-cavity resonators because there are no two separate conductors in the cross-section of the system that could create a static potential difference (Collin, 2007). Each mode is characterized by its own resonance frequency, field distribution, and energy density (Balanis, 2012).

In TE modes, the propagation-directional component of the electric field is zero (E_z=0), while the longitudinal component of the magnetic field is not zero ($H_z \neq 0$). In this case, the electric field is entirely located in the transverse plane, while the longitudinal component of the magnetic field is decisive in energy transfer. In TM modes, the opposite of TE is true; the propagation-directional component of the magnetic field is zero (H_z=0), while the longitudinal component of the electric field is not zero ($E_z \neq 0$). In this mode, energy density is more predominantly represented by the electric field (Figure 2). In TEM modes, both the propagation-directional components of the electric and magnetic fields are zero (E_z=0, H_z=0) (Pozar, 2012).

Figure 2. TE and TM Modes.

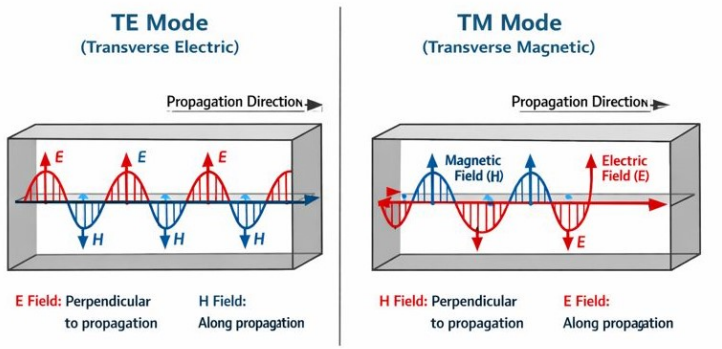

Another distinguishing feature of EM modes is the spatial behavior of the field components. Within a resonator, the electric and magnetic field components exhibit sinusoidal distributions in three directions of space, or distributions defined by various specific functions (Balanis, 2012). While some regions of the field exhibit maximum values, others experience points where the field drops to zero. This spatial distribution directly determines the physical character of the mode and the energy density within the resonator. Different modes can produce different field distributions within the same resonator. Modes are generally represented as TE_{mnp} or TM_{mnp}

(Marcuvitz, 1951). Here, the indices m, n, and p indicate how many half-waves the EM field contains in the respective spatial directions (Collin, 2007). Modes with lower indices generally have lower resonance frequencies, and in most applications, these lower-index modes are the first to be excited, referred to as the fundamental mode. Consequently, the concept of EM modes is the most fundamental physical component determining the operating principle of microwave resonators. The frequency at which the resonator operates, where the field will be concentrated, and how energy will be stored are directly dependent on the modes used. Therefore, the correct definition and analysis of the modes form the basis of microwave resonator design and performance evaluation. This is because the EM modes supported in a microwave resonator cannot be directly and arbitrarily selected by the system user. These modes are determined by the geometric structure of the resonator, the EM boundary conditions, and the applied feeding mechanism. However, the designer can practically guide which mode will be effectively and dominantly excited by designing the resonator dimensions, excitation frequency, and excitation type to suit the target mode.

The Relationship Between The Coordinate System and the Resonator Maxwell Equations

This section examines in detail why EM field solutions in microwave resonators are directly dependent on the choice of coordinate system, how this choice is necessarily determined by geometry, and how Maxwell's equations are transformed into different mathematical structures in different coordinate systems. This relationship, which forms the analytical basis of mode analysis, is critical for the accurate modeling of resonators (Tang, Li, Chen, Wang, & Jiang, 2024). EM field analysis in resonators begins with Maxwell's equations formulated in the appropriate coordinate system; here, the choice of coordinates fundamentally determines

the complexity of solving boundary value problems (Naji & Warr, 2019).

EM fields are vector quantities that carry information about direction and magnitude at every point in space. The electric field E and the magnetic field H can have components in different spatial directions, and the mathematical expression of these components varies depending on the coordinate system used. Therefore, although Maxwell's equations are physically universal laws independent of the coordinate system (Jackson, 2021), the explicit mathematical form of these equations takes different forms depending on the coordinate system used (Collin, 2007).

In the Cartesian coordinate system, field components are expressed as E_x, E_y, E_z and H_x, H_y, H_z, while in the cylindrical coordinate system there are different component definitions such as E_r, E_φ, E_z and in the spherical coordinate system E_r, E_θ, E_φ. This situation directly leads to mathematical differences in the modeling of EM fields through differential operators (Balanis, 2012).

In microwave resonators, fields are generally analyzed by assuming time harmonics. In this approach, it is assumed that all field magnitudes change sinusoidally with respect to time, and the fields are expressed using complex amplitudes as shown in (1) and (2).

$$E(r,t)=\Re\{E(r)e^{j\omega t}\} \quad (1)$$

$$H(r,t)=\Re\{H(r)e^{j\omega t}\} \quad (2)$$

Thanks to this acceptance, Maxwell's equations are reduced to a time-independent frequency domain form, and the problem ceases to be a time-dependent differential equation problem and becomes a spatial boundary value problem. This transformation forms the basis for performing mode analysis and resonance frequency calculations analytically (Collin, 2007).

Maxwell's equations under the assumption of time harmonics are shown in equations (3) and (4).

$$\nabla \times E = -j\omega\mu H \tag{3}$$

$$\nabla \times H = j\omega\varepsilon E \tag{4}$$

If wave equations for electric and magnetic fields are derived separately from equations (3) and (4), equations (5) and (6) are obtained.

$$\nabla^2 E + k^2 E = 0 \tag{5}$$

$$\nabla^2 H + k^2 H = 0 \tag{6}$$

Here, $k=\omega\sqrt{\mu\varepsilon}$ represents the wave number. These wave equations are fundamental differential equations that determine the spatial distribution of fields within the resonator. However, writing these equations in a solvable form directly depends on the coordinate system used (Balanis, 2012).

The Effect of Boundary Conditions on the Modal Structure

In closed metal-walled microwave cavity resonators, boundary surfaces are generally modeled as perfect conductors (PEC). In this case, the tangential components of the electric field on the metal surfaces must be zero ($E_t=0$) (Pozar, 2012).

This boundary condition allows only certain spatial field patterns to form within the resonator. The formation of random field distributions is physically impossible. When boundary conditions are considered together with the wave equations, an eigenvalue problem arises. These eigenvalues represent the resonance frequencies, and the eigenfunctions represent the field distributions of the modes.

Geometry-Coordinate System Compatibility and Separability

For the analytical solution of resonator modes, it is essential that the coordinate system used is compatible with the resonator geometry. This compatibility allows the wave equations to be written in a separable form (Pozar, 2012).

- In rectangular cavity resonators: the Cartesian coordinate system is used. Field solutions are expressed with sine and cosine functions. Separable solutions are obtained directly (Pozar, 2012).
- In cylindrical cavity resonators: A cylindrical coordinate system is used. Bessel functions are derived in field solutions. Angular and radial dependencies are separated from each other (Pozar, 2012).
- In spherical cavity resonators: A spherical coordinate system is used. Spherical harmonic functions are included in the solution. The fields exhibit three-dimensional angular dependence (Harrington, 2001).

Even though the coordinate system is not a direct physical quantity in itself, it indirectly generates a strong influence on the resonant behavior in that it defines the mathematical terms through which mode frequencies are derived. In rectangular resonators, mode frequencies can be expressed in terms of algebraic roots, in cylindrical resonators the roots of Bessel functions can be used to give mode frequencies, and in spherical resonators roots of the spherical harmonics eigenvalues can be used to give mode frequencies. This clearly explains why resonators with different geometries exhibit completely different frequency spectra and why mode densities vary from structure to structure.

Mode Analysis in A Rectangular Cavity Resonator

Microwave resonators are rectangular cavity resonators, which are the most basic and widely used structure (Pozar, 2012). Rectangular cavity resonators are widely used in the literature as instructive and reference structures for mode analysis due to their geometric simplicity and the mathematically separable solutions they offer.

The rectangular cavity resonator is a closed volume with edge lengths a, b and d respectively, filled with a homogeneous medium and all surfaces considered to be perfect conductors (PEC). The boundary conditions for the dimensions of the resonator are shown in (7) using the Cartesian coordinate system.

$$0 \leq x \leq a,\ 0 \leq y \leq b,\ 0 \leq z \leq d \tag{7}$$

This structure, due to its symmetry properties, allows EM fields to be expressed in a separable manner along the x, y, and z directions.

Since all walls of the rectangular cavity resonator are considered perfect conductors, the tangential components of the electric field on the metal surfaces must be zero (E_t=0).

This boundary condition severely restricts the EM field distributions that can occur within the resonator, allowing only modes with specific spatial patterns to form. When the boundary conditions are solved together with the wave equations, an eigenvalue problem arises for the resonator.

The field is expressed by the scalar Helmholtz equation obtained for the longitudinal component of the electric or magnetic field under harmonic assumption (8), (9) (Pozar, 2012).

$$\nabla^2 \Psi + k^2 \Psi = 0 \tag{8}$$

$$\Psi(x,y,z) = X(x)Y(y)Z(z) \tag{9}$$

The solutions to these equations are expressed in terms of sine and cosine functions.

In TE modes, the component of the electric field in the direction of propagation is zero (E_z=0).

In this case, the solution is realized in terms of the longitudinal component of the magnetic field in H_z. Considering the boundary conditions, the H_z component is expressed as in (10).

$$H_z = H_0 . cos\left(\frac{m\pi x}{a}\right) . cos\left(\frac{n\pi y}{b}\right) sin\left(\frac{p\pi z}{d}\right) \qquad (10)$$

In Equation (10), m, n and p are integers greater than or equal to zero and cannot be zero at the same time. These indices represent the spatial mode number of the field distribution inside the resonator.

In TM modes, the longitudinal component of the magnetic field is zero (H_z=0).

In this case, the solution is realized through the longitudinal component of the electric field, E_z. Considering the boundary conditions, the E_z component is expressed as in (11).

$$E_z = E_0 . sin\left(\frac{m\pi x}{a}\right) . sin\left(\frac{n\pi y}{b}\right) sin\left(\frac{p\pi z}{d}\right) \qquad (11)$$

In TM modes, the indices m, n, and p must all be non-zero. This is a direct consequence of the boundary conditions.

The resonance frequencies of the TE and TM modes for the rectangular cavity resonator are given by a common expression. This expression is shown in Equation (12).

$$f_{mnp} = \left(\frac{c}{2}\right) \sqrt{(m/a)^2 + (n/b)^2 + (p/d)^2} \qquad (12)$$

In equation (12) c stands to denote the phase velocity of the EM wave within the resonator. This formula makes it obvious that

the dimensions and mode indices of the resonator help in determining the resonance frequencies.

With a rectangular cavity resonator, the mode with the lowest resonance frequency is the fundamental mode. In most applications, depending on the geometric dimensions, the basic mode is either TE_{101} or TE_{011}. The first mode is especially popular in real-life engineering practice due to the low loss and constant distribution of the field.

Here the Cartesian coordinates system in finding the analytical solution of EM modes of rectangular cavity resonators has been provided. The results of the obtained expressions demonstrate unambiguously the direct correlation between the resonator geometry and the mode structure and give a strong theoretical foundation on which the numerical and comparative analysis will be presented in the subsequent sections.

Mode Analysis in Cylindrical Cavity Resonator

Cylindrical cavity resonators are preferred in many microwave applications due to their rotational symmetry, although their mode structures exhibit different mathematical properties compared to rectangular cavities. This difference is fundamentally based on the change in the coordinate system used.

A cylindrical cavity resonator is a closed metal volume with radius a and height d. The interior of the resonator is filled with a homogeneous medium and all surfaces are considered to be perfect conductors (PEC). Boundary conditions for the dimensions of the resonator using a cylindrical coordinate system are shown in (13).

$$0 \le r \le a,\ 0 \le \varphi < 2\pi,\ 0 \le z \le d \tag{13}$$

This geometry allows EM fields to be expressed in separate radial, angular, and longitudinal directions.

The scalar Helmholtz equation obtained under the assumption of time harmonics is represented by equation (14) and takes the form of equation (15) in the cylindrical coordinate system.

$$\nabla^2\Psi + k^2\Psi = 0 \tag{14}$$

$$\left(\frac{1}{r}\right)\left(\frac{\partial}{\partial r}\right)\left(r\frac{\partial\Psi}{\partial r}\right) + \left(\frac{1}{r^2}\right)\left(\frac{\partial^2\Psi}{\partial\varphi^2}\right) + \frac{\partial^2\Psi}{\partial z^2} + k^2\Psi = 0 \tag{15}$$

In cylindrical cavity resonators, the longitudinal component of the electric field is zero in TE modes (E_z=0).

In this case, the solution is made in terms of the longitudinal component of the magnetic field H_z. For TE modes, the H_z component is generally written as: $J_m(\cdot)$ is the m-th order Bessel function and is shown in equation (16).

$$H_z = H_0 J_m\left(\frac{x_{\{mn\}r}}{a}\right) cos(m\varphi)\, sin\left(\frac{p\pi z}{d}\right) \tag{16}$$

In TM modes, the longitudinal component of the magnetic field is zero (H_z=0). In this case, the solution is made via the longitudinal component of the electric field E_z, and the general expression is shown in equation (17).

$$E_z = E_0 J_m\left(\frac{y_{\{mn\}r}}{a}\right) \cos(m\varphi)\, \sin\left(\frac{p\pi z}{d}\right) \tag{17}$$

For TE and TM modes, the values y_{mn} and x_{mn} represent the roots of the Bessel Function.

The resonance frequencies of TE and TM modes in cylindrical cavity resonators are given by the following general expression equation (18) (Harrington, 2001).

$$f_{\{mnp\}} = \left(\frac{c}{2\pi}\right)\sqrt{\left(\frac{x_{\{mn\}}}{a}\right)^2 + \left(\frac{p\pi}{d}\right)^2} \tag{18}$$

Comparison of Rectangular and Cylindrical Cavity Resonators

The fundamental differences between cylindrical cavity resonators and rectangular cavity resonators are: In a rectangular cavity, modes are expressed using trigonometric functions. In a cylindrical cavity, the mode structure is determined by Bessel functions. Angular symmetry in a cylindrical cavity significantly affects the field distribution of the modes. The resonance spectrum can be denser and more complex in a cylindrical cavity. All these differences stem from the direct relationship between the resonator geometry and the coordinate system used (Collin, 2007; Harrington, 2001; Pozar, 2012).

In this section, EM modes in cylindrical cavity resonators are analytically investigated using a cylindrical coordinate system. The existing literature shows that the mode structure is directly dependent not only on the resonator dimensions but also on the mathematical nature of the coordinate system.

Mode Analysis in A Spherical Cavity Resonator

When considering cavity resonators with spherical symmetry and examining their EM mode structures using a spherical coordinate system, it is seen that spherical cavity resonators, although having a more limited range of applications compared to rectangular and cylindrical cavities in practical applications, are the structures that most clearly reveal the relationship between mode analysis and the coordinate system. Therefore, spherical resonators constitute an important reference example in theoretical EM field analyses (Jackson, 2021). A spherical cavity resonator is a closed sphere with radius a, filled with a homogeneous medium, and its surface is considered a PEC. Boundary conditions for resonator dimensions using a spherical coordinate system are shown in (19).

$$0 \leq r \leq a,\ 0 \leq \theta < \pi,\ 0 \leq \varphi \leq 2\pi \tag{19}$$

Spherical geometry reveals a more complex spatial behavior in which EM fields vary in both radial and angular directions. The geometry allows for the expression of EM fields in a separable manner in radial, angular, and longitudinal directions. The scalar Helmholtz equation obtained under the time harmonic assumption is shown by (20). In the spherical coordinate system, it becomes a rather long expression due to the complex nature of the Laplace operator. The separable solution approximation is expressed by equation (21).

$$\nabla^2 \Psi + k^2 \Psi = 0 \tag{20}$$

$$\Psi(r, \theta, \varphi) = R(r)\Theta(\theta)\Phi(\varphi) \tag{21}$$

Angular equations are solved in terms of spherical harmonic functions, and radial equation in terms of spherical Bessel functions (Jackson, 2021).

In spherical cavity resonators, unlike in previous sections, TEM modes do not occur, and only TE and TM modes are supported. In TE modes, the radial component of the electric field is zero, and in TM modes, the radial component of the magnetic field is zero. These modes exhibit complex patterns where the fields are distributed in accordance with spherical symmetry. Mode structures in spherical resonators create a denser spectrum compared to rectangular and cylindrical cavities. The main reason for this is the increase in degrees of freedom in the angular direction (Jackson, 2021).

In the case of spherical cavity resonators resonant frequencies are calculated with eigenvalues of spherical Bessel functions and spherical harmonics. Such eigenvalues are not expressible in close form as the product of simple algebraic numbers, and are typically obtained either from tabulated values or through numerical methods. This scenario easily illustrates the reason why

the mode frequencies of spherical resonators must be of more complicated mathematical nature than the other geometries.

Theoretical EM analysis Spherical cavity resonators are of greater importance to theoretical analysis than to practical engineering. They provide one of the most general and symmetrical examples of the solution of the Maxwell equations and best illustrate the choice of coordinate system on mode analysis.

Spherical cavity resonators are more important in theoretical EM analysis than in practical engineering applications. These structures offer one of the most general and symmetrical solution examples of Maxwell's equations and most clearly demonstrate the effect of coordinate system selection on mode analysis.

In this respect, spherical resonators can be viewed as the complementary example of the method of describing the coordinate system that is presented in this study. Here, the spherical cavity resonators are explored with the help of a spherical coordinate system where EM modes are analyzed. The mathematical representation of mode analysis needs to increase in complexity with the increase of complexity in the resonator geometry. This again shows how the choice of a coordinate system is decisive to solutions of EM fields.

Numerical Computation-Visualization Approach

This section aims to visualize the EM mode expressions obtained analytically in previous sections by transferring them to a digital environment and calculating resonance frequencies and field distributions. The main goal of this approach is to demonstrate that coordinate system-based mode analysis is not only theoretical but also numerically verifiable and visually interpretable. Most current studies in the literature involve full-wave numerical methods (Bişkin, Saydam, & Aksoy, 2025; Di Vora et al., 2024; Lee, Kim, Rim, Kwon, & Choi, 2024; Zadeh et al., 2024). In this study,

however, numerical calculations are performed using an approach that directly utilizes analytical solutions and does not involve any full-wave numerical methods (FEM, FDTD, etc.). Thus, the results obtained are a direct extension of the theoretical expressions presented in previous sections.

Numerical calculations were performed for three main purposes: numerical calculation of the analytically obtained resonance frequencies for the rectangular cavity resonator, numerical verification of the fundamental mode (the lowest frequency mode), and visualization of the EM field distribution for a selected mode. For these purposes, all calculations were performed in the MATLAB environment; MATLAB was only used for the numerical evaluation of analytical expressions and the visual presentation of the obtained results.

The values given in Table 1. are the data outputs of the system prepared in the MATLAB simulation environment for the rectangular cavity resonator with dimensions a = 0.10m, b = 0.05m, d = 0.08m based on equation (12).

In closed rectangular cavity resonators, since the fields must satisfy the standing wave condition in the longitudinal direction, modes corresponding to the p=0 condition are not physically accepted. Therefore, although the TE_{100} mode is defined as the fundamental mode in waveguide structures, the physical mode with the lowest resonance frequency in closed cavity resonators is the TE_{101} mode. As a result of the numerical calculations performed in this study, it was seen that the (m,n,p) = (1,0,1) mode has an approximate resonance frequency of 2.4 GHz and can be defined as the fundamental mode for the rectangular cavity resonator. The obtained results are in full agreement with the theoretical expectations regarding closed cavity resonators.

Table 1. Example Numerical Calculation of Resonance Frequency in a Rectangular Cavity Resonator

m	n	p	Resonance Frequency (GHz)
1	0	0	1.50
0	1	0	3.00
0	0	1	1.88
1	1	0	3.35
1	0	1	2.40
0	1	1	3.55
1	1	1	3.86

Since the mode examined in this section is the TE mode, the longitudinal component of the electric field is zero. Therefore, the longitudinal component of the magnetic field, which most clearly represents the mode structure and spatial field distribution, was chosen to visualize the field distribution. This section's work can be detailed in another study, including examples within the TM mode. The relevant field distribution visualization is shown in Figure 3.

Figure 3. Magnetic Field Distribution in TE_{101} Mode

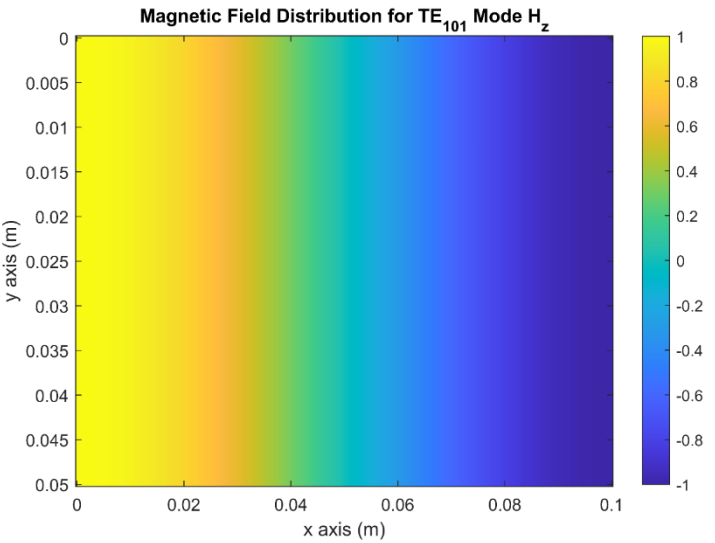

A cross-section in the middle of the resonator was visualized in a two-dimensional cross-section. Looking at the field distribution, the H_z component will be seen to have a cosinusoidal variation in the x-direction and homogeneous in the y-direction. It implies that during the TE_{101} mode the field varies in both x and z directions only and no node is formed in the y-direction. These transitions between the positive and negative field regions clearly reveal the nodal and antinodal regions of the resonator. This calculated field distribution agrees with the field behavior of TE modes and points to the numerical results of the analytically derived mode expression. The visual interpretation of the coordinate-dependent mode structure of rectangular cavity resonators is possible by this result.

When the Bessel function structure is analyzed in MATLAB, the resonance frequency for the cylindrical cavity resonator is found to be 2.57 GHz. Figure 4. shows the MATLAB analysis command line for this function structure.

Figure 4. MATLAB Analysis Commands for Bessel Function in Cylindrical Cavity Resonators

```
a = 0.05;
d = 0.08;
c = 3e8;
x_11 = 1.841;
p = 1;
f_cyl = (c/(2*pi))*sqrt((x_11/a)^2 + (p*pi/d)^2);
fprintf('Cylindrical cavity TE_11 mode frequency: %.2f GHz\n', ...
        f_cyl/1e9);
```

The analytical expressions of EM field distributions in cylindrical and spherical cavity resonators involve special functions such as Bessel functions and spherical harmonics, depending on the coordinate system used. This makes the visualization of field distributions mathematically more complex and relegates the comparison of the coordinate system-based solution structure, which is the main objective of this study, to a secondary role. Therefore, while a detailed visualization of the field distribution is presented for the rectangular cavity resonator, the field distributions for cylindrical

and spherical cavity resonators are not presented graphically; instead, the focus is on the numerical calculation of the resonance frequencies that characterize the mode behavior of these structures. In this context, the resonance frequencies of the selected modes for the cylindrical cavity resonator, along with the roots of the Bessel function used, are shown in Table 2. below.

Table 2. Resonance frequencies of selected modes for cylindrical cavity resonator (p = 1)

Mode	**Root used**	**Root Value**	**Resonance Frequency**
TE_{111}	$J_1'(\chi) = 0$	1.841	2.57 GHz
TM_{011}	$J_1'(\chi) = 0$	2.405	2.96 GHz
TE_{211}	$J_2'(\chi) = 0$	3.054	3.47 GHz
TE_{011}	$J_2'(\chi) = 0$	3.832	4.11 GHz
TM_{111}	$J_0'(\chi) = 0$	3.832	4.11 GHz

Table 2. displays the resonance frequencies of various TE and TM modes of the cylindrical cavity resonator. The χ 2 values which are obtained in the calculations are just the zero points of the Bessel functions and their derivatives which are determined as part of the radial solution of the field equations in the cylindrical coordinate system. The primary motivation behind such use of such roots is that the metal-walled cavity boundary conditions demand that the electric or magnetic field components in the radial direction are zero at some radius values. The terms of TE mode imply that the derivative conditions apply to the magnetic field, so the roots of the Bessel functions are taken, whereas in TM mode the roots of the Bessel functions are taken, as it is the case that the electric field is zeroed. The acquired resonance frequencies indicate that the frequency rises with the increase in the root value given that a clear indication of the mode order and frequency spectrums is determined based on the coordinate system within the cylindrical cavity resonators.

Approach Comparisons

By using a Cartesian coordinate system in rectangular cavity resonators, Maxwell equations can be solved as a product of sine and cosine decoupled equations. This allows getting resonance frequencies in closed form and visualizing field distributions in a relatively simple manner.

However, in cylindrical cavity resonators, a cylindrical coordinate system is used and solutions are represented in terms of Bessel functions and resonance frequencies are calculated in terms of the roots of these functions. This adds mathematical complexity to the structure of the solution and complicates field distributions visualization.

The use of the spherical coordinate system of spherical cavity resonators simplifies the computations of solutions to spherical harmonics and spherical Bessel functions, and typically does not permit the resonance frequencies to be expressed in closed form. Thus, the significance of the coordinate system-based approach is shown by the fact that the spherical cavity resonators are essentially important in revealing the mathematical constraints of this method.

Whilst resonance frequencies in rectangular cavity resonators can be directly determined in terms of geometric dimensions and mode indices, resonance frequencies in cylindrical cavity resonators are determined to be based on the roots of the Bessel function. In sphere cavities resonant systems, resonance frequencies are primarily determined by numbers.

In this regard, the frequency expression derived in the rectangular cavity resonators provide the simplest form of solution, whereas the expression of the cylindrical and the spherical cavity resonators are characteristic of their respective increasing complexity in math. It proves that the selection of a coordinate system is not a matter of preference that is geometrically inclined,

but a core component that directly defines how the solution will be represented.

Compared to all other field distribution structures, the rectangular cavity resonators are the most beneficial structure when assessed in terms of visualizing field distribution. Field distributions using a Cartesian coordinate system have made possible solutions to be the clear and intuitive presentation of field distributions on two-dimensional cross-sections. Thus, the visualization of the field distribution of a rectangular cavity resonator has been conducted.

This is not true in cylindrical and spherical cavity resonators however because the field expressions require the addition of special functions that complicate the visualization process. In the present work, as the primary aim of the given work is to demonstrate how the coordinate system influences the structure of the solution, field distributions of these resonators have not been represented graphically, rather an analysis has been conducted in accordance with their frequency behavior.

In terms of numerical values, rectangular cavity resonators are the most acceptable structure in directing the transfer of the analytical expressions to the numerical context. Although numerical analysis of the cylindrical cavity resonator involves the application of Bessel function roots, numerical methods cannot be avoided in the spherical cavity resonators. This scenario proves the fact that the coordinate system based approach is not only decisive in the methods of computation but also in practical methods of the computation. These differences have been concretely demonstrated by calculations done in the MATLAB environment.

Conclusion And Evaluation

The paper examines the EM mode behaviour in microwave resonators in the context of a coordinate system-based approach. The cavity resonators are taken as rectangular, cylindrical, and spherical

cavity resonators and the influence of resonator geometry and the adopted coordinate system on the EM field solutions is shown on analytical, numerical and visual levels. It is revealed that the mode patterns, which result in a solution of Maxwell equations in with respect to different coordinate systems, are marked by major differences not only due to geometric differences but also as a direct result of the mathematical structure of the solution. In the case of rectangular cavity resonators, it was found that the solutions found in the Cartesian coordinate system can be used to express resonance frequencies in closed form and explicitly visualize field distributions. This framework provides the most convenient method of analytical checks by numbers and physical clarity of field patterns. It has been demonstrated that in the cylindrical cavity resonators, passing to the cylindrical coordinate system the solutions can be represented in the form of Bessel functions and the resonance frequencies can be found using roots of Bessel functions. The most complicated form of the solution structure is the spherical cavity resonators in the form of spherical coordinate system, and resonance frequencies have often been found not to have a closed form. Mathematical calculations conducted in the research made it possible to check the mode expressions obtained analytically in the MATLAB program; it became possible to solidify the theoretical findings by calculating the resonance frequencies, estimating the fundamental mode, and plotting the field distribution of a chosen mode. The correspondence between the numerical and analytical values is confirmation of credibility of coordinate system-based method. The results evidently demonstrate that the EM mode analysis of microwave resonators can vary not only with the geometry of the resonators but also with a coordinate system. This research paper is a systematic approach to the relationship between coordinate system, geometry, and mode analysis and gives the information which is usually widely distributed in the literature in a comprehensive structure.

References

Alahnomi, R. A., Zakaria, Z., Yussof, Z. M., Althuwayb, A. A., Alhegazi, A., Alsariera, H., & Rahman, N. A. (2021). Review of recent microwave planar resonator-based sensors: Techniques of complex permittivity extraction, applications, open challenges and future research directions. *Sensors, 21*(7), 2267.

Balanis, C. A. (2012). *Advanced engineering electromagnetics*: John Wiley & Sons.

Bişkin, O. S., Saydam, T., & Aksoy, S. (2025). Accuracy Analyses of FDTD Resonance Frequency Calculations for a Partially Dielectric-Filled Cavity. *International Journal of Numerical Modelling: Electronic Networks, Devices and Fields, 38*(1), e70011.

Collin, R. E. (2007). *Foundations for microwave engineering*: John Wiley & Sons.

Di Vora, R., Braggio, C., Carugno, G., Gardikiotis, A., Lombardi, A., Ortolan, A., & Ruoso, G. (2024). A new class of axion haloscope resonators: the polygonal coaxial cavity. *arXiv preprint arXiv:2403.14503*.

Harrington, R. F. (2001). Time-harmonic electromagnetic fields. *(No Title)*.

Jackson, J. D. (2021). *Classical electrodynamics*: John Wiley & Sons.

Lee, Y.-H., Kim, I., Rim, S., Kwon, T.-Y., & Choi, M. (2024). Resonant mode calculation method for extremely large-scale optical ring resonators. *Optics Express, 32*(18), 31231-31237.

Marcuvitz, N. (1951). *Waveguide handbook*: Iet.

Naji, A., & Warr, P. A. (2019). Geometrical perturbation techniques and Approximate Analysis for eigenmode splitting and shifting in electromagnetic planar Dual-Mode Resonators. *Scientific reports, 9*(1), 2417.

Pozar, D. M. (2012). Microwave engineering. *Fourth Editions, University of Massachusetts at Amherst, John Wiley & Sons, Inc*, 26-30.

Sheng, N., Xiong, W., Hao, S., & Wang, S. (2020). *Microwave material electromagnetic parameter testing system based on the resonant cavity method.* Paper presented at the 2020 International Conference on Microwave and Millimeter Wave Technology (ICMMT).

Tang, Z., Li, Y., Chen, Z., Wang, Y., & Jiang, M. (2024). Advancing electromagnetic field modeling in axially anisotropic media with conformal method in 3D cylindrical coordinate systems. *Physica Scripta, 99*(6), 065526.

Yang, X., Leon Bennett, E., Calisir, I., Xiao, J., & Huang, Y. (2024). Theoretical study of new microwave resonators utilizing dispersive materials. *Journal of Applied Physics, 136*(16).

Zadeh, S. G., Ghirri, A., Pagano, S., Tocci, S., Gatti, C., & Cassinese, A. (2024). High-Q cavity coupled to a high permittivity dielectric resonator for sensing applications. *arXiv preprint arXiv:2410.05831*.

Zou, J., Li, C.-J., Zheng, C., Wang, D., Zhang, J., Wang, X., . . . Hou, Z.-L. (2023). A Novel Strategy for Detecting Permittivity and Loss Tangent of Low-Loss Materials Based on Cylindrical Resonant Cavity. *Sensors, 23*(12), 5469.

CHAPTER 4

THE ROLE OF FPGAS IN THE PHYSICAL LAYER OF NEXT-GENERATION MOBILE COMMUNICATION SYSTEMS

1. SELMAN KULAÇ[1]

Introduction

The development of next-generation wireless communication technologies such as 5G and 6G has further increased the importance of hardware architectures used at the physical layer (PHL) to enhance network capacity, speed, and reliability. The fundamental goals of 5G and 6G networks include high data rates, low latency, wide coverage, and energy efficiency. Achieving these goals relies heavily on computationally intensive

[1] Prof. Dr., Duzce University, Electrical-Electronics Engineering Dept., Orcid: 0000-0002-7737-1569

signal processing algorithms and high bandwidth at the physical layer. Therefore, comparing different hardware platforms such as FPGA (Field Programmable Gate Array), ASIC (Application Specific Integrated Circuit), CPU (Central Processing Unit), and GPU (Graphics Processing Unit) in terms of performance, energy efficiency, and flexibility has become a critical research area for both academic and industrial applications.

The fundamental processes used in the physical layer of 5G and 6G technologies include channel coding (e.g., LDPC and Turbo coding), multiple antenna systems (MIMO), modulation/demodulation, signal filtering, mathematical transformations such as FFT/IFFT, and AI-based optimizations. Performing these processes at high speed and low latency directly impacts the overall network performance. The high data speeds and low latency requirements of 5G and 6G, in particular, push the limits of traditional CPU-based solutions. At this point, alternative hardware architectures such as GPUs, FPGAs, and ASICs are coming to the forefront.

Comparison of Processor Hardware Plaforms

Comparative studies on the performance of physical layer operations on hardware platforms reveal the unique advantages and disadvantages of each platform. For example, FPGAs can offer both higher performance and better energy efficiency compared to CPUs and GPUs in basic linear algebra operations such as BLAS (Basic Linear Algebra Subroutines). One study showed that a matrix-multiplication core developed on an FPGA was 18.7-22.0 times faster than a CPU and 3.8-6.0 times faster than a GPU (Xiong & Xu, 2020:5). Similarly, an FPGA-based Mersenne Twister random number generator operated approximately 25 times faster than a CPU and 9 times faster than a GPU (Tian & Benkrid, 2009:5). Furthermore, from an energy efficiency perspective, it has

been reported that FPGAs can generate 37 and 35 times more random numbers than CPUs and GPUs, respectively, with the same amount of energy (Tian & Benkrid, 2009:5).

However, GPUs excel particularly in applications requiring high parallelism, such as deep learning and image processing. For example, in the training and inference of deep neural networks (DNNs), GPUs provide significant speedups compared to CPUs due to their multi-core architecture (Kokkinis et al., 2024). However, the high power consumption and data transfer latencies of GPUs can be a disadvantage, especially in embedded and energy-constrained applications (Hu et al., 2022:8). Furthermore, while GPUs offer high programmability and flexibility, hardware-level customization options are more limited compared to FPGAs.

ASICs offer the highest performance and energy efficiency at the physical layer. Especially in use cases where high data rates and minimal delay are critical, such as 5G and 6G, ASIC-based solutions are preferred. For example, a 192 Mbps MIMO-OFDM transceiver ASIC design can successfully manage the high computational load and hardware complexity brought by multi-antenna systems (Perels et al., 2005:4). However, the lack of flexibility and high development costs of ASICs pose a disadvantage during periods when new standards and algorithms change rapidly (Hu et al., 2022:8).

A study presented information stating that the architecture of FPGAs makes them an efficient solution for hardware acceleration, and offered the following: Devices like ASICs and GPUs use an outdated method for switching between programming and memory. Furthermore, the high amount of power required for storage and retrieval tasks causes performance latency, making them unsuitable for applications where real-time information is needed. The reconfigurable nature of FPGAs grants them greater flexibility compared to ASICs, but this comes at the cost of higher

power consumption and larger physical footprint. They are also more efficient than general-purpose processors, but require more complex programming and lower flexibility costs. Unlike ASICs and GPUs, FPGAs do not need to switch between memory and programming, making the data storage and retrieval process more efficient. Because the FPGA architecture is more flexible, the amount of power an FPGA uses for a particular task can be customized to the desired level. Unlike GPUs, which contain processing cores that must receive and execute instructions, FPGAs have a flexible architecture that maps code to physical logic circuits. However, similar to GPU programming, a fundamental understanding of the underlying principles is necessary to write code that achieves optimal performance (Amato, 2023:84).

Another study focuses on algorithms and non-binary low-density parity control (NB-LDPC) decoder designs targeting GPU, FPGA, and ASIC-based architectures. The former is noted for providing high energy efficiency due to its high core count (i.e., data parallelism) and memory bandwidth, while requiring twice as much power as the latter. FPGAs, as shown in later sections of the study, require low power (ASICs even lower) and high-efficiency performance (ASICs even higher). They offer a high degree of customization and can lead to superior energy efficiency. However, it is emphasized that both present limitations in terms of coding and development effort, parallelization complexity, and cost compared to GPUs (Ferraz et al., 2021:33).

In their 2021 study, Chundi et al.2022:11 presented a model-based neural network algorithm for channel estimation in 5G mmWave communication systems, along with hardware peer optimization and a matched FPGA subsystem implementation. Several neural network structures and methods leveraging sparsity to reduce computational complexity were examined. A key finding was that quantizing weights and activations to lower bit precisions,

together with implementing a purpose-built cache, effectively lowered off-chip memory traffic. The FPGA prototype was highlighted as providing up to a 10-fold improvement in latency compared to Intel Xeon processors and Nvidia 2080 Ti GPUs. The improved latency and lower resource usage resulted in a 300-fold reduction in the subsystem's energy consumption compared to CPU and GPU-based systems.

The first part of Shah's 2023:148 study proposes an efficient and reconfigurable implementation of the 3rd Generation Partnership Project (3GPP) 3D-SCM (Spatial Channel Model) for 5G-NR on Xilinx and Intel FPGA platforms using a high-level synthesis (HLS) oriented approach flow. The impact of various HLS optimization techniques on total latency and hardware resource utilization on the target acceleration platforms is investigated. Using the proposed methodologies, accelerated designs on Xilinx Alveo U280 and Intel Arria 10 FPGAs achieved speed increases of 65x and 95x, respectively, compared to the base CPU implementation. This speed increase was further enhanced to 173x by optimizing the design to utilize specialized resources such as UltraRAM (URAM) and High Bandwidth Memory (HBM) found on the Xilinx FPGA. The latter segment of this paper focuses on accelerating the 3GPP channel model using GPU platforms. This study examines different optimization techniques to leverage the parallelism and memory hierarchy of GPUs, focusing particularly on CUDA-based solutions. Empirical findings reveal that the implemented solution operates at about 240 times faster than the CPU-based implementation. The GPU design exhibits a 33.3% increase in single-precision performance compared to an accelerated design on a data center-class FPGA. However, it also consumes 7.5% more energy.

In summary, the comparison of hardware architectures deployed in the 5G and 6G physical

layers holds significant importance with respect to network performance, powerefficiency, adaptability,and scalability. Existing research demonstrates that each hardware solution performs best in particular use cases, and the optimal platform must be chosen based on the specific application demands. For example, FPGAs are preferred in applications requiring low latency, flexibility, and energy efficiency; GPUs in high parallelism, dense matrix operations, and deep learning applications; and ASICs in situations requiring maximum performance and energy efficiency in the final products (Kestur et al., 2010:6) (Xiong & Xu, 2020:5) (Hu et al., 2022:8) (Tian & Benkrid, 2009:5) (Perels et al., 2005:4). CPUs, conversely, stand out with their flexibility and ease of software-based development. In this context, comparing hardware platforms in the 5G and 6G physical layers stands out as a fundamental research area for the design and optimization of future communication networks.

Examples of FPGA Hardware Plaform Use Cases for 5G and 6G Physical Layers

Fifth and sixth generation (5G and 6G) wireless communication technologies play a fundamental role in today's digital transformation. These technologies are designed to meet critical requirements such as high data rates, low latency, wide coverage, and reliability. Field Programmable Gate Arrays (FPGAs) stand out as a key hardware solution in meeting the complex algorithms and high-performance requirements that arise in the physical layer (PHY) of 5G and 6G. The use of FPGAs in the physical layer is critical in meeting the requirements of next-generation communication systems due to both their reconfigurability and hardware acceleration advantages.

To understand the use cases of FPGAs in the 5G and 6G physical layer, it is first necessary to examine the fundamental

requirements of these technologies and the challenges encountered in the physical layer. 5G is designed to support different use cases such as ultra-reliable low-latency communication (URLLC), enhanced mobile broadband (eMBB), and massive machine-type communication (mMTC). 6G, on the other hand, is shaped by advanced goals such as even higher data rates, near-zero latency, artificial intelligence integration, and global coverage (Nakamura, 2020:5). These goals necessitate the development of more complex algorithms and hardware solutions in the physical layer.

One of the key technologies that stands out in the 5G and 6G physical layer is multiple-input multiple-output (MIMO) and OFDM-based systems. Park and Ogunfunmi addressed the efficient implementation of the MIMO-OFDM physical layer on FPGAs and demonstrated that fundamental operations such as the fast Fourier transform can be optimized with shared architectures to save hardware resources. The proposed architecture saves at least 40% of hardware resources while providing the same data rate as known MIMO-OFDM implementations (Park & Ogunfunmi, 2012:25). This work reveals how effective the parallel processing capabilities of FPGAs are in implementing complex signal processing algorithms in real-time at the physical layer.

New modulation techniques used in 5G systems are also important areas requiring the use of FPGAs. Keerthana and Rajaram investigated the implementation of a Filter Banked Multi-Carrier Modulation (FBMC) based baseband modulator, proposed as an alternative to OFDM in 5G systems, on an FPGA. FBMC offers advantages such as better spectral efficiency and lower out-of-band propagation. In this study, the FBMC baseband modulator was modeled on an FPGA and evaluated in terms of performance, resource utilization, and power consumption. The results show that the FPGA architecture offers an efficient solution in digital signal processing applications thanks to its reconfigurability, compact

size, and high computational power (Keerthana & Rajaram, 2019:6). These findings demonstrate that new waveforms in 5G and 6G can be rapidly prototyped at the physical layer using FPGAs.

Another important issue at the physical layer of 5G is error correction coding. Specifically, low-density parity check codes (LDPC) and polarity codes are used as fundamental error correction mechanisms in the 5G NR (New Radio) standard. Nadal and Baghdadi addressed the implementation of Quasi-Cyclic (QC) LDPC, the key channel coding code for 5G, on an FPGA with an efficient and flexible hardware architecture. The proposed architecture offers high parallelism to support all 5G configurations and maximizes processing unit utilization, increasing processing speed. Compared to a marketable 5G LDPC decoder, the introduced FPGA prototype provides higher processing speeds in most configurations (Nadal & Baghdadi, 2020:7). This work demonstrates that FPGAs are an ideal platform for flexible and high-performance error correction solutions at the physical layer of 5G.

Similarly, the implementation of polar codes used in 5G control channels on FPGAs is also an important research area. Mohammed and Abdullah investigated the combined implementation of polar coding and chaotic modulation used for control channels in 5G wireless systems on an FPGA. Leveraging its parallel processing architecture, the FPGA can execute encoding and decoding tasks more rapidly and with lower resource utilization. The research demonstrated that the framework developed using Xilinx System Generator was effectively deployed on FPGA hardware and consumed fewer resources relative to prior works. (Mohammed & Abdullah, 2022:6). These findings reveal that complex encoding techniques in 5G and 6G can be effectively developed at the physical layer with FPGAs.

In the study by Rudramuniyappa and Harsha, a novel architecture is presented for the FPGA implementation of an end-to-end PDCCH (Physical Downlink Control Channel) chain compliant with 3GPP standards for 5G-NR. The proposed end-to-end implementation is stated to consume 30705 resources (1.98%) with a latency of 1.5 μs. The novel design demonstrates superior performance compared to the prior solution and its simpler implementation in terms of latency, resource utilization, throughput, and power efficiency (Rudramuniyappa & Harsha et al. 2025:14).

In another study, heuristic tree-search-based approaches were proposed to overcome this challenge as a way to meet the real-time decoding requirements for large MIMO configurations. FPGAs offer an ideal platform for accelerating MIMO signal decoding due to their potential for integration into the signal processing chain with low latency and low power consumption. This study presents a software/hardware collaborative design for a multi-level tree-search approach integrating the computation of multiple tree levels. The proposed heuristic method is stated to transform the tree-search process into a stream operation suitable for FPGA architecture. A series of hardware designs and algorithmic optimizations that significantly improve scalability and decoding time are demonstrated. As a result, a design capable of decoding 64x64 64-QAM MIMO code within 10 ms real-time requirements is obtained (Hassan, et al, 2025:11).

In conclusion, the application areas of FPGAs in the physical layer of 5G and 6G encompass a wide range of fields, including the implementation of advanced modulation techniques such as MIMO-OFDM and FBMC, hardware acceleration of error correction algorithms such as LDPC and polar codes, high-throughput implementation of security protocols, real-time processing of base station hardware, optimization of control

channels, prototyping of next-generation waveforms, and satellite communications. Current research in these areas clearly demonstrates that FPGAs are an indispensable hardware platform in the 5G and 6G physical layer.

References

Xiong, C. & Xu, N. (2020). Performance comparison of blas on cpu, gpu and fpga. *2020 IEEE 9th Joint International Information Technology and Artificial Intelligence Conference (ITAIC)* . https://doi.org/10.1109/itaic49862.2020.9338793

Tian, X. & Benkrid, K. (2009). Mersenne twister random number generation on fpga, cpu and gpu. *2009 NASA/ESA Conference on Adaptive Hardware and Systems* . https://doi.org/10.1109/ahs.2009.11

Kokkinis, G., Ahmed, Q. Z., Sambell, A., Chochliouros, I. P., Lazaridis, P. I., & Zaharis, Z. D. (2024). A comparison between cpu and gpu computing in dnn-based doa estimation. *Mechanisms and Machine Science* . https://doi.org/10.1007/978-3-031-49421-5_64

Hu, Y., Liu, Y., & Liu, Z. (2022). A survey on convolutional neural network accelerators: gpu, fpga and asic. *2022 14th International Conference on Computer Research and Development (ICCRD)* . https://doi.org/10.1109/iccrd54409.2022.9730377

Perels, D., Haene, S., Luethi, P., Burg, A., Felber, N., Fichtner, W., & Bölcskei, H. (2005). Asic implementation of a mimo-ofdm transceiver for 192 mbps wlans. *Proceedings of ESSCIRC 2005 : 31st European Solid-State Circuits Conference* . https://doi.org/10.1109/ESSCIR.2005.1541598

Amato, Giovanni Luca. (2023) *Acceleration of an OFDM modulator on a Xilinx FPGA*. Diss. Politecnico di Torino.

Ferraz, Oscar, et al. (2021). A survey on high-throughput non-binary LDPC decoders: ASIC, FPGA, and GPU architectures. *IEEE Communications Surveys & Tutorials* 24.1 (2021): 524-556.

Chundi, Pavan Kumar, Xiaodong Wang, and Mingoo Seok. (2021) Channel estimation using deep learning on an FPGA for 5G millimeter-wave communication systems. *IEEE Transactions on Circuits and Systems I: Regular Papers* 69.2. 908-918.

Shah, NASIR ALI. (2023). Heterogeneous Acceleration for 5G New Radio Channel Modelling Using FPGAs and GPUs.

Kestur, S., Davis, J. D., & Williams, O. (2010). Blas comparison on fpga, cpu and gpu. *IEEE Computer Society Annual Symposium on VLSI* . https://doi.org/10.1109/isvlsi.2010.84

Nakamura, T. (2020). 5g evolution and 6g. *2020 IEEE Symposium on VLSI Technology* . https://doi.org/10.1109/vlsitechnology18217.2020.9265094

Park, J. S. & Ogunfunmi, T. (2012). Efficient fpga-based implementations of mimo-ofdm physical layer. *Circuits, Systems, and Signal Processing 31*(4). https://doi.org/10.1007/s00034-012-9411-4

Keerthana, R. & Rajaram, S. (2019). Fpga implementation of fbmc baseband modular for 5g wireless communication. *2019 2nd International Conference on Intelligent Computing, Instrumentation and Control Technologies (ICICICT)* . https://doi.org/10.1109/icicict46008.2019.8993290

Nadal, J. & Baghdadi, A. (2020). Fpga based design and prototyping of efficient 5g qc-ldpc channel decoding. *2020 International Workshop on Rapid System Prototyping (RSP)* . https://doi.org/10.1109/rsp51120.2020.9244853

Mohammed, R. K. & Abdullah, H. A. (2022). Efficient fpga implementation of chaotic based communication system with polar encoding. *2022 9th International Conference on Electrical and Electronics Engineering (ICEEE)* . https://doi.org/10.1109/iceee55327.2022.9772554

Rudramuniyappa, Harsha, et al. (2025). Optimized Algorithms for FPGA Implementation of PDCCH Chain for 5G-NR Base Station." *IEEE Transactions on Circuits and Systems I: Regular Papers*.

Hassan, Mohamed W., Hatem Ltaief, and Suhaib A. (2024) Fahmy. "High throughput massive MIMO signal decoding using multi-level tree search on FPGAs." *2024 IEEE 32nd Annual International Symposium on Field-Programmable Custom Computing Machines (FCCM)*. IEEE.

CHAPTER 5

DEEP REINFORCEMENT LEARNING APPROACH FOR PRIORITY-CONSTRAINED DYNAMIC MULTI-STOP VEHICLE ROUTING PROBLEM

1. Mert Sami ŞENERLER[1]
2. Hasan TİRYAKİ[2]

Introduction

The exponential growth of e-commerce volume and the proliferation of "on-demand" service models in recent years have necessitated a fundamental paradigm shift in urban logistics operations. Traditional Vehicle Routing Problem (VRP) approaches used in logistics planning, wherein all demands are known a priori (static), prove insufficient in meeting today's dynamic, uncertain, and speed-centric logistics requirements (Simoni and Winkenbach, 2023).

Modern logistics operations exhibit a stochastic nature characterized by the real-time arrival of orders, continuously fluctuating traffic conditions, and differentiating customer expectations. In this context, the problem evolves beyond merely finding the shortest path for vehicles; it transforms into a complex challenge regarding which orders to group (batching), which deliveries require urgency (priority), and how to optimize multi-stop routes under capacity constraints (Maleki and Asadi, 2024). In particular, the concurrent management of

[1] Master's Student, Kırklareli University Electrical and Electronics Engineering, Orcid: 0009-0008-7717-3766
[2] Assoc. Prof., Kırklareli University, Electrical and Electronics Engineering, Orcid: 0000-0001-9175-0269

orders requiring urgent delivery within the same pool as standard orders gives rise to an optimization problem in the "NP-Hard" class, thereby intensifying operational complexity.

Heuristic methods such as Genetic Algorithms, Tabu Search, or Nearest Neighbor (Greedy) are frequently employed in the literature to solve such dynamic problems (Wang et al., 2025). However, these methods often exhibit a "myopic" nature and neglect long-term reward maximization. For instance, Zhang and Van Woensel (2023) emphasized the necessity for methods capable of anticipating the stochastic nature of dynamic events, stating that heuristic-based approaches prove inadequate during periods of peak demand and create bottlenecks that diminish overall system efficiency.

Deep Reinforcement Learning (DRL) stands out as a robust alternative to surmount these limitations. DRL enables an agent to learn the optimal "policy" through trial-and-error by interacting with its environment. In this study, the Proximal Policy Optimization (PPO) algorithm was selected, as it is increasingly regarded as the "gold standard" in the literature for dynamic routing problems, particularly due to its stability and sample efficiency (Deineko and Kehrt, 2024; Argoubi and Mili, 2024).

The primary objective of this study is to develop a priority-aware PPO model possessing end-to-end learning capabilities to address the Dynamic Order Assignment and Routing problem encountered in urban delivery operations.

The primary objective of this study is to develop a priority-aware PPO model possessing end-to-end learning capabilities to address the Dynamic Order Assignment and Routing problem encountered in urban delivery operations.

The principal objectives of the model addressed within the scope of this study are as follows:

- **Dynamic Batching:** Enabling the agent to form efficient groups by making strategic waiting decisions rather than processing orders individually (Cals et al., 2021).

- **Priority Management**: Ensuring that high-urgency orders (High Priority) are autonomously recognized by the system and prioritized during delivery processes (Colak and Fescioglu-Unver, 2024).
- **Robustness:** Ensuring the system can maintain operations without failure under conditions of excessive demand load and uncertainty.

An examination of the existing literature reveals that current studies generally treat assignment and routing as decoupled problems (Maleki and Asadi, 2024). These studies typically utilize PPO for assignment while delegating routing tasks to heuristic (greedy) methods.

By addressing these gaps in the literature, this study presents the following original contributions:

- **Integrated Decision Mechanism:** An integrated approach is presented that optimizes assignment and routing decisions within a hierarchical structure and is capable of making "one-shot" decisions.
- **Reward-Based Priority Learning:** Urgency constraints are taught to the agent through the reward function rather than rule-based systems; it has been experimentally proven that the agent processes high-priority orders faster than standard ones, similar to the "Attention Score Amplifier" logic proposed by Deineko and Kehrt (2024).
- **Robustness Under Stress:** The developed model has demonstrated its operational robustness by maintaining its success rate compared to the traditional Greedy method in stress tests where demand density was increased by 50%.

Literature Review

In this section, the evolution within the literature of the Dynamic Vehicle Routing Problem (DVRP), Deep Reinforcement Learning (DRL) algorithms, and the constraints forming the foundation of this study (priority, batching, multi-stop) is reviewed. By focusing on recent

studies between 2021 and 2025, this review aims to identify the limitations of existing methods and highlight the research gaps that this study intends to bridge.

Whereas the Traditional Vehicle Routing Problem (VRP) possesses a deterministic structure in which all demands are known a priori (before operation), modern logistics has evolved into Dynamic VRP (DVRP), a stochastic process where the information set is updated over time. In their comprehensive literature review on DVRP, Zhang and Van Woensel (2023) attribute this shift to the increase in "speed and uncertainty" factors in logistics and classify the problem as "DVRP with Random Requests" (DVRPRR).

Traditional solution methods, namely Exact Methods and Meta-heuristics (e.g., Genetic Algorithms, Tabu Search), prove insufficient in dynamic environments requiring real-time decision-making due to their high computational burdens. This limitation has steered researchers towards "Data-Driven" approaches, which are capable of being trained offline and generating decisions in the order of milliseconds during online operations (Shahbazian et al., 2024).

Deep Reinforcement Learning (DRL) demonstrates superior generalization capabilities compared to traditional methods, particularly in combinatorial optimization problems characterized by high-dimensional state spaces (Zhang et al., 2025). An examination of the studies in the literature reveals a distinct divergence in algorithmic preferences:

- **Deep Q-Network (DQN):** Although preferred in some early studies, its applicability to large-scale problems has been scrutinized, as the computational power required—particularly in large action and observation spaces—becomes a bottleneck (Cals et al., 2021). Furthermore, it has been reported in the literature that DQN tends to overestimate action values, which negatively impacts training stability and convergence (Colak and Fescioglu-Unver, 2024; Wu et al., 2025). The risk of "suboptimal convergence" in vast state-action spaces limits its success in complex constrained problems (Deineko et al., 2024).

- **Proximal Policy Optimization (PPO):** Recent studies highlight PPO for DVRP and order assignment solutions due to its stability (Deineko and Kehrt, 2024; Maleki and Asadi, 2024). The primary reason for selecting PPO is its use of a "clipped objective function," which prevents drastic shifts in policy updates, thereby minimizing the risk of training collapse and offering a more stable learning process (Argoubi and Mili, 2024). Additionally, unlike value-based methods, it is computationally more efficient as it updates the policy without the necessity of calculating every single state-action pair (Cals et al., 2021). Specifically in problems requiring constraint satisfaction, PPO produces more reliable results compared to other methods thanks to this stable structure (Argoubi and Mili, 2024).

In the realm of dynamic logistics, urgency is predominantly modeled using hard time windows. However, in their study on electric vehicle charging stations, Colak and Fescioglu-Unver (2024) argue that urgency should be managed not solely through temporal constraints but also via "priority classes" (e.g., Express vs. Normal). Furthermore, they assert that Deep Reinforcement Learning (DRL) outperforms classical methods in maintaining the equilibrium between these classes. In the literature, urgency management is generally addressed under two main categories:

- **Dynamic State Features:** Deineko and Kehrt (2024) defined an "Urgency Factor" (f_u) based on the remaining time and distance for each request in their PPO-based models, thereby ensuring that the network's attention mechanism focuses on this input.
- **Reward Shaping:** Beeks et al. (2022) employed Bayesian optimization to dynamically shape the reward function in multi-objective optimization problems (e.g., minimizing late orders). Similarly, Colak and Fescioglu-Unver (2024) proposed a reward mechanism that imposes a penalty on the agent in the event of delays for high-priority services.

The processing of orders in groups rather than individually (known as batching) is a critical strategy for enhancing operational efficiency. In the literature, this subject is examined through concepts such as "Virtual Batching" and "Strategic Waiting."

- **Strategic Waiting:** The capability of an agent to select a "wait" action to construct a more efficient route in the future, rather than pursuing an immediate but minor reward, was successfully implemented by Cals et al. (2021) in e-commerce warehouses.
- **Matching Degree:** Maleki and Asadi (2024) proposed a "Matching Degree" (MD) function that measures the compatibility of orders with one another and with the courier. However, the aforementioned study utilized the batching process solely during the assignment phase, while adhering to a dynamic greedy method during the routing phase.

The Vehicle Routing Problem with Pickup and Delivery (VRPPD) mandates that the vehicle must visit the pickup point (P_i) before the delivery point (D_i). In DRL models, this precedence constraint is typically enforced via the "Action Masking" method (Pathan and Shrivastava, 2024). Zhang et al. (2025) demonstrated the superiority of learning-based methods in dynamic insertion problems using Transformer-based architectures and Rotary Positional Embeddings (RoPE) in their model named "Neuro-Ins."

Studies from the 2024–2026 period (including pre-prints) that are directly related to the subject of this study are summarized below:

- **Zou et al. (2025)-Multi-Agent Pointer Transformer (MAPT):** They proposed the "Multi-Agent Pointer Transformer" model for multi-vehicle dynamic problems. Although this study addresses the concept of batching through vehicle coordination and utilizes relation-aware attention, it models priority constraints as a stochastic variable, focusing on joint action distribution rather than explicit priority management.

- **Maleki and Asadi (2024)-MDRL:** These authors adopted a two-stage approach termed "Multi-step DRL" (MDRL). In the first stage, order assignment (determining the proportion of orders to assign) is performed using PPO, while a dynamic heuristic method is employed for routing in the second stage. This "decoupled" structure may lead to assignment decisions failing to fully predict the subsequent routing costs.
- **Argoubi and Mili (2024)-Hybrid PPO-GNN:** In their study on fuel distribution, they combined PPO with Graph Neural Networks (GNN) and incorporated a deterministic constraint verification layer. While the study focuses on time windows and feasibility, it does not cover dynamically changing customer priority levels (express/normal) as proposed in this study.

The conducted literature review indicates that existing studies remain insufficient in three fundamental aspects:

- **Decoupling of Assignment and Routing:** Even recent studies, such as Maleki and Asadi (2024), decouple the problem into assignment (learning-based) and routing (heuristic-based) phases. This separation leads to missed opportunities for integrated (end-to-end) optimization.
- **Dynamic Priority Integration:** Neural solutions addressing how an incoming urgent order should dynamically alter the existing route in multi-stop scenarios are limited. While Deineko and Kehrt (2024) approached this issue via attention mechanisms, there is a scarcity of studies combining this approach with multi-vehicle settings and dynamic batching.
- **Learning of Constraints:** The autonomous learning of PDP constraints and urgency levels via the reward function-as opposed to strictly rule-based methods, similar to the work of Colak and Fescioglu-Unver (2024)- remains an open research area.

This study aims to bridge these gaps in the literature by unifying assignment and routing within a single hierarchical structure using the PPO algorithm and by training the model on priority constraints via a reward mechanism.

Material and Method

In this section, the mathematical model (Markov Decision Process) of the addressed Dynamic Vehicle Routing Problem (DVRP), the proposed solution architecture (Centralized PPO Agent), and the technical details of the simulation environment where the experiments were conducted are presented. Going beyond a purely theoretical optimization model, the study is constructed within a realistic "Digital Twin" environment built upon real geographical data (OpenStreetMap) belonging to the Kırklareli Central District and stochastic variables (traffic, weather conditions, preparation times).

Rather than a Multi-Agent structure where each courier acts as an independent decision-maker, the proposed architecture is built upon a Centralized PPO Agent (Centralized Dispatcher) that manages the entire fleet from a single center. The simulation environment comprises a total of 60 couriers directed by the agent. To reflect real-world dynamics, the fleet structure consists of heterogeneous vehicle types:

- **Motorcycle:** 45 km/h speed and a carrying capacity of 2 packages.
- **Light Commercial Vehicle:** 35 km/h speed and a carrying capacity of 4 packages.
- **Bicycle:** 20 km/h speed and a carrying capacity of 1 package.

The problem is modeled as a Markov Decision Process (MDP). At each time step t, the agent receives a state observation (S_t) from the environment, selects an action (A_t), and consequently obtains a reward (R_t) and a new state (S_{t+1}).

The agent's perception of the environment is structured as a flattened architecture consisting of normalized vectors. The state vector S_t comprises three main components:

$$S_t = \{O_t, C_t, \tau_t\} \quad (1)$$

Where:

- $\boldsymbol{O_t}$ **(Order State):** A 6-dimensional feature vector generated for each active order.

$$o_i = [p_i, t_{SLA}^{rem}, x_i^{rest}, y_i^{rest}, x_i^{cust}, y_i^{cust}] \quad (2)$$

Here, p_i represents the order's priority coefficient, t_{SLA}^{rem} the remaining delivery time, and the (x, y) coordinates represent the restaurant/customer locations.

- $\boldsymbol{C_t}$ **(Courier State):** A 5-dimensional state vector for each courier in the fleet.

$$c_j = [I_{avail}, L_{cur}, x_j^{cur}, y_j^{cur}, Cap_{max}] \quad (3)$$

Here, I_{avail} indicates the courier's availability status (binary value), and L_{cur} denotes the instantaneous load.

- $\boldsymbol{\tau_t}$ **(Global Time):** Normalized time information used to learn traffic density and order patterns.

A Multi-Discrete action space is utilized in the study. This structure allows the agent to make an independent decision for every order in the assignment pool. The dimension of the action space is as follows:

$$A_t \in \{0,1, \dots, K\}^N \quad (4)$$

Here, N represents the maximum number of active orders, and K represents the number of couriers. The action $K + 1$ corresponds to the "No-Op" (No Operation or Do Not Assign) action. This structure allows the agent to decide to strategically wait when a suitable match is not yet available.

The reward function R_t, which guides the agent's learning process, is designed to maximize on-time delivery while penalizing constraint violations and the delay of urgent orders.

The total reward consists of the following components:

$$R_{total} = R_{delivery} + R_{penalty} \quad (5)$$

On-Time Delivery Reward ($R_{delivery}$): A scaled reward is given to encourage early delivery when the order is delivered within its SLA (Service Level Agreement) duration:

$$R_{delivery} = \alpha \cdot \left(1.0 - 0.5 \cdot \frac{t_{elapsed}}{t_{SLA}} \right) \quad (6)$$

(Here, α is the scaling coefficient.)

Penalties ($R_{penalty}$):

- **Delay Penalty:** A fixed penalty (-0.2) is applied in the event that the SLA duration is exceeded.
- **Cancellation Penalty:** A large penalty (-1.0) is applied if the order cannot be delivered and results in cancellation.
- **Priority Penalty**: An additional penalty (-0.02) is applied for each time step when the waiting time of high-priority orders exceeds a critical level (90% of SLA). This term serves as the fundamental mechanism ensuring the agent focuses on priority orders.

The Proximal Policy Optimization (PPO) algorithm was utilized for the training of the model. PPO ensures the stable progress of training by limiting policy updates within a trust region (clip range).

The model possesses a non-shared Multi-Layer Perceptron (MLP) architecture for both the Policy (Actor) and Value (Critic) functions.

- **Input Layer:** Flattened State Vector (S_t).
- **Hidden Layers:** 2 hidden layers, each consisting of 64 neurons.
- **Activation Function:** Tanh or ReLU.
- **Output Layer**: Action probability distribution (Logits).

During the 1 million-step training process, the hyperparameters specified in the table below were used to optimize stability.

Table 1 PPO Model Training Hyperparameters

Parametre	Value	Description
Learning Rate (α)	5×10^{-5}	Low learning rate for stable convergence.
n_steps	4096	Data steps collected in each update cycle.
Batch Size	1024	Sample group used in gradient calculation.
Gamma (γ)	0.99	Importance coefficient assigned to future rewards.
Entropy Coef.	0.1	High entropy to maintain exploration ability.
Clip Range (ϵ)	0.05	Conservative limit in policy updates.

In order to enhance the validity of the study, a comprehensive simulation environment reflecting real-world dynamics was developed instead of a simple grid-world. This "Digital Twin," built upon geographical data belonging to Kırklareli Central District, possesses a stochastic rather than a deterministic (fixed) structure:

- **Order Generation:** Poisson sürecine benzer şekilde, günün saatine göre değişen talep yoğunluklarıyla rastgele sipariş üretimi yapılmaktadır.
- **Traffic and Weather:** The developed "Traffic Management Subsystem" and "Weather Profile" dynamically adjust vehicle speeds based on the time of day and weather conditions (rain, snow).
- **Uncertainties:** Restaurant preparation times and order cancellation probabilities are modeled using a Gaussian distribution.

The general operation of the simulation environment and the agent's decision-making process is summarized in Figure 1.

Figure 1 Flow Diagram of the Simulation Model and Hierarchical Control Architecture.

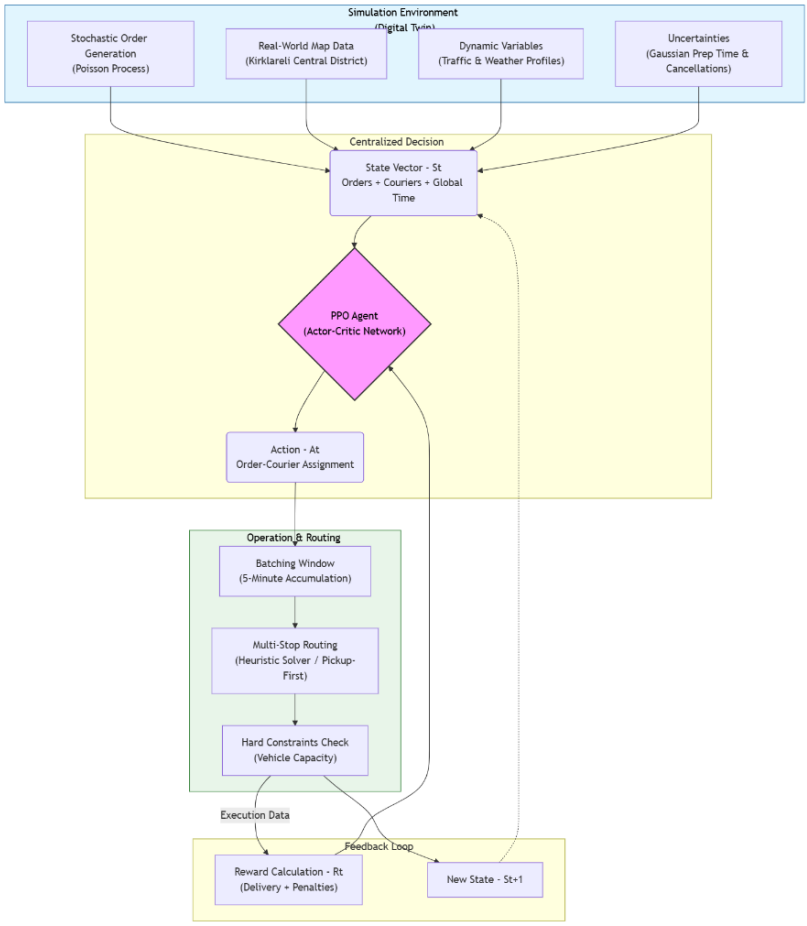

The diagram in Figure 1 illustrates the loop between the stochastic environment and the PPO Agent. The system generates the state (S_t) through a Poisson process and uncertainties (Traffic, Weather). While the PPO Agent makes assignment decisions (A_t), these decisions are passed through a batching window and optimized by a heuristic solver under strict capacity constraints.

As seen in the flow diagram, the proposed system utilizes a hierarchical structure containing a combination of "End-to-End" assignment and "Heuristic" routing:

- **Batching Window:** Orders are presented to the agent in 5-minute time windows. This allows the agent to optimize orders in the pool rather than acting reactively to individual orders.
- **Capacity and Multi-Stop:** The physical capacity of the vehicles is defined as a "Hard Constraint". When multiple orders are assigned to a courier, the multi-stop routing algorithm generates the shortest route by observing the "Pickup before Delivery" rule.

Results and Discussion

In this section, the performance of the developed PPO-based dynamic vehicle routing model is evaluated considering the concepts of "Overall Efficiency," "Priority Sensitivity," and "Operational Robustness." The obtained results are presented in comparison with the "Greedy" (Nearest Neighbor) algorithm, which was selected as the Baseline. The experiments were conducted on 24-hour operational datasets within the Kırklareli city center simulation environment shown in Figure 2.

Figure 2 Kırklareli City Center

The primary performance of the model was evaluated based on the order fulfillment rate (Success Rate) and total work volume (Throughput). The comparative analyses presented in Figure 3 and Figure 4 demonstrate that the PPO agent provides a significant advantage in operational efficiency.

Figure 3 Comparison of Success Rates of PPO and Greedy Algorithms

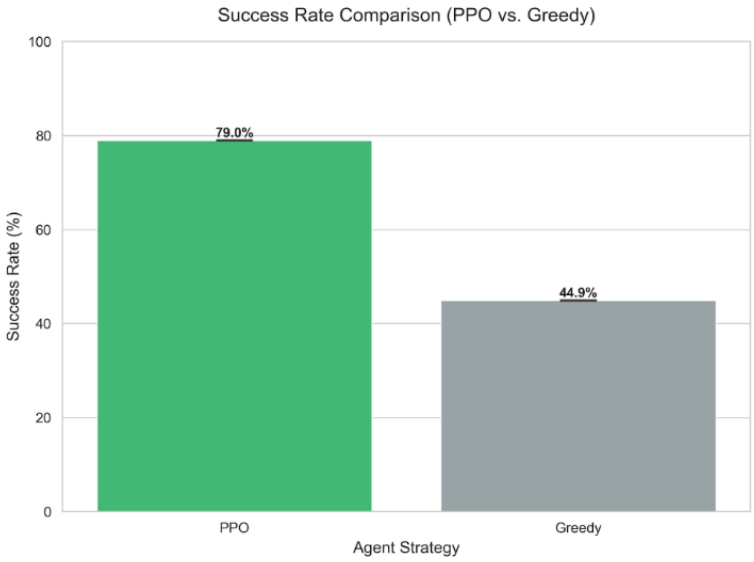

According to the simulation results;

- **Greedy Algorithm:** Could only deliver 44.9% of the orders on time. Focusing on local (myopic) decisions, this approach caused couriers to fill their capacity on inefficient routes and led to system congestion during peak hours.
- **PPO Agent:** Achieved a 79.0% success rate under the same conditions. Learning to maximize long-term gain through the reward function, the agent managed the courier fleet more effectively, approximately doubling the Service Level.

Figure 4 Total Delivered Order Volume (24-Hour)

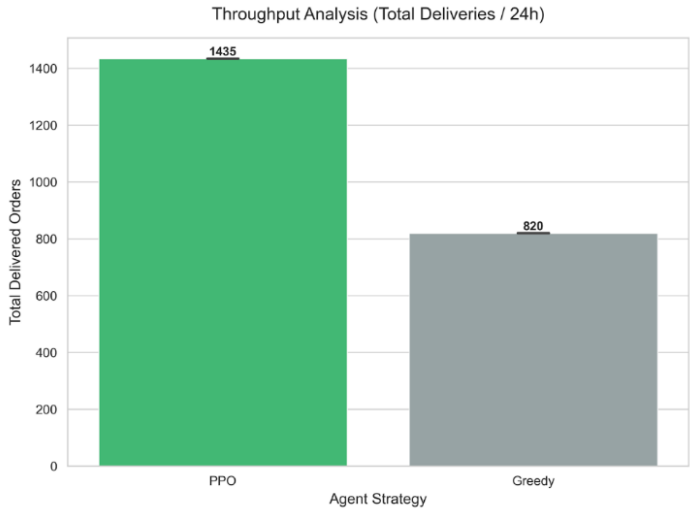

When analyzed in terms of work volume, the PPO agent completed a total of 1435 deliveries, whereas the Greedy method remained at 820. This demonstrates that the proposed model can meet 75% more demand with existing resources and proves that it maximizes operational capacity usage (Fleet Utilization).

It was observed that the "Strategic Waiting" behavior, mentioned in the literature by Cals et al. (2021), emerged autonomously in our developed model. Figure 5 shows the average delivery times.

Figure 5 Average Delivery Times of the Algorithms

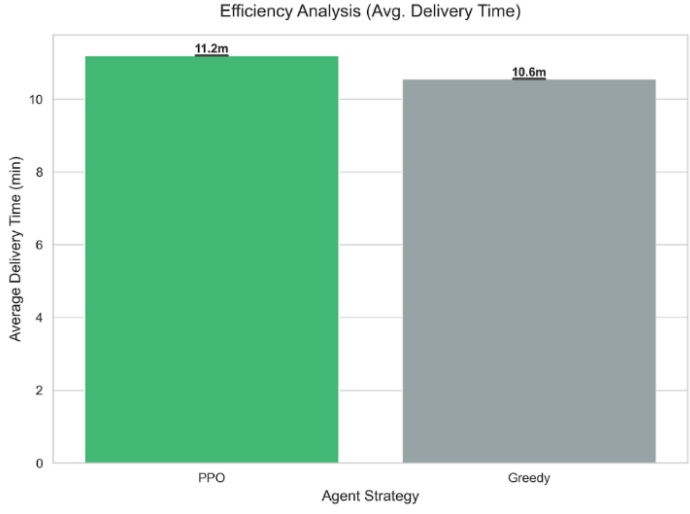

As seen in Figure 5, the average delivery time of the PPO agent (11.2 min) is marginally higher than that of the Greedy method (10.6 min). This situation is not a performance loss; rather, it represents a conscious strategy. While the Greedy algorithm tends to transport incoming orders instantly and individually, the PPO agent preferred to perform grouping (Batching) by holding orders in the pool for a short period. This slight sacrifice in delivery time enabled a massive increase in the total number of transported packages (Figure 4).

One of the fundamental hypotheses of the study is whether the PPO agent can distinguish "High Priority" orders. In this analysis (Figure 6), in order to eliminate the bias created by restaurant preparation times (Hot: 15 min, Normal: 10 min), the data was examined using the "Normalized Pickup Delay" metric.

Figure 6 Courier Response Times According to Order Priorities (Pickup Delay)

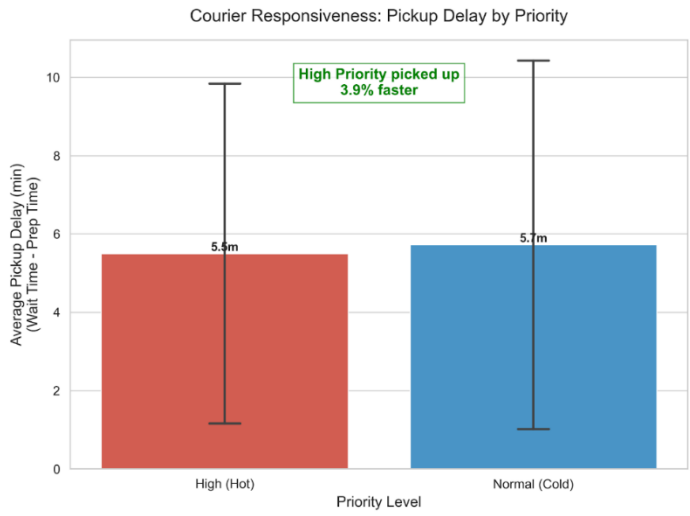

The findings in Figure 6 prove that the PPO agent is sensitive to urgency levels (Priority Levels).

- **High Priority Orders:** Were picked up with an average delay of 5.5 minutes.
- **Normal Orders:** ere picked up with an average delay of 5.7 minutes.

Statistically, the agent responded 3.9% faster to urgent orders. This finding confirms that the "delay penalties" integrated into the reward function ($R_{penalty}$) within the MDP model were autonomously learned by the agent. The agent discovered that the cost of delaying urgent orders is high without any rule-based coding.

In order to test the scalability of the developed model, a "Chaos Scenario" was created by increasing the Order Generation Rate by 50%. The analyses of this situation are presented in Figure 7.

Figure 7 Robustness Test Under 50% Increased Demand Load

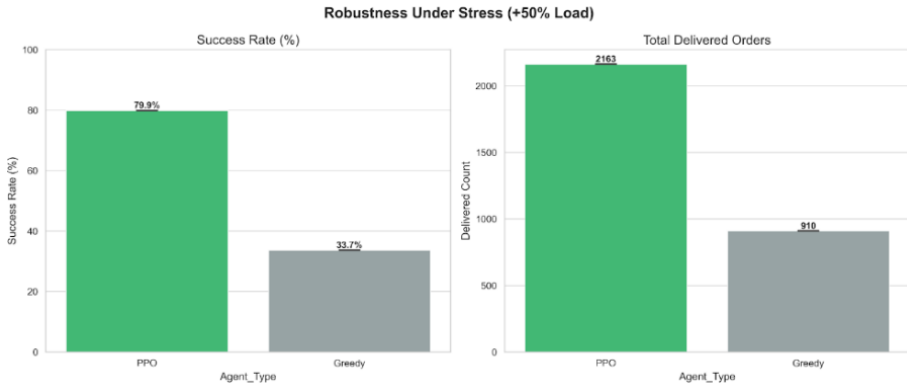

The results presented in Figure 7 constitute the most striking finding of the study:

- **System Collapse (Greedy):** Under increased load, the success rate of the Greedy algorithm dropped dramatically to the 33.7% level. Simple heuristic methods failed to manage the increasing combinatorial complexity, leading to system congestion.
- **Robustness (PPO):** he PPO agent exhibited high resilience (Robustness) by maintaining a 79.9% success rate even in the chaos environment. As intensity increased, the agent adopted a more aggressive grouping (batching) strategy and successfully delivered 2163 orders.

This result demonstrates that the proposed "Hierarchical PPO" architecture offers a reliable solution not only under normal conditions but also during unforeseen demand fluctuations.

Conclusion

In this study, an integrated solution architecture based on Deep Reinforcement Learning (PPO) was developed for the "Priority-Constrained Dynamic Vehicle Routing Problem" (Priority-Constrained DVRP), one of the most complex problems of modern urban logistics. Extensive simulations conducted under stochastic demand and traffic conditions within a simulation environment created using real geographical location data of Kırklareli province and urban detour factors have proven the superiority of the proposed model over traditional methods.

Key inferences obtained from the study are as follows:

- **Operational Superiority:** he developed PPO agent generated 75% more work volume (throughput) with the same resources compared to the standard "Nearest Neighbor" (Greedy) algorithm and increased the success rate from 44.9% to 79.0%. This result indicates that artificial intelligence optimizes not only the route but also the fleet capacity.
- **Autonomous Strategy Development:** It was revealed that the agent autonomously learned the "strategic waiting" behavior, which increases total efficiency by briefly holding and grouping (Batching) orders instead of delivering them instantly.
- **Priority Sensitivity:** Without any rule-based coding, the model successfully distinguished "High Priority" orders solely through the penalty mechanism in the reward function. In analyses adjusted for preparation times, it was determined that urgent orders were processed statistically faster than normal orders.
- **Robustness**: The most critical finding of the study was obtained in stress tests. In the chaos scenario where the demand load was increased by 50%, while traditional methods collapsed (33% success), the proposed model

maintained the 80% level, proving that the system possesses high resilience against uncertainties.

While this study reveals the potential of "End-to-End" learning approaches in dynamic routing problems, it also opens new doors for future research:

- **Multi-Agent Collaboration (Multi-Agent RL):** In the current study, a centralized agent makes the decisions. In future studies, distributed architectures (MARL) where each courier makes their own decisions and communicates with each other can be examined.
- **Graph Neural Networks (GNN):** Representing the state space with Graph Neural Networks instead of vectors may enable better learning of relationships in the map topology.
- **Real-World Integration (Sim2Real):** It is suggested to transfer the developed model from the simulation environment to real logistics operations (Transfer Learning) and to test it on drone-supported hybrid delivery scenarios.

In summary, it is expected that increasing studies aimed at the optimization of modern urban logistics, as in this study, will be beneficial in reducing traffic density and carbon emissions.

References

Argoubi, M., & Mili, K. (2025). A Hybrid PPO-GNN Framework for Adaptive Vehicle Routing under Uncertainty: Application to Fuel Delivery Logistics. IEEE Access, 1–1. https://doi.org/10.1109/access.2025.3635886

Beeks, M., Afshar, R. R., Zhang, Y., Dijkman, R., Van Dorst, C., & De Looijer, S. (2022, June). Deep reinforcement learning for a multi-objective online order batching problem. In Proceedings of the International Conference on Automated Planning and Scheduling (Vol. 32, pp. 435-443). https://doi.org/10.1609/icaps.v32i1.19829

Cals, B., Zhang, Y., Dijkman, R., & Van Dorst, C. (2021). Solving the online batching problem using deep reinforcement learning. Computers & Industrial Engineering, 156, 107221. https://doi.org/10.1016/j.cie.2021.107221

Colak, A., & Fescioglu-Unver, N. (2024). Deep reinforcement learning based resource allocation for electric vehicle charging stations with priority service. Energy, 313, 133637. https://doi.org/10.1016/j.energy.2024.133637

Deineko, E., & Kehrt, C. (2024). Learn to solve vehicle routing problems asap: A neural optimization approach for time-constrained vehicle routing problems with finite vehicle fleet. arXiv preprint arXiv:2411.04777. https://doi.org/10.2139/ssrn.4975275

Maleki, A., & Asadi, A. OPTIMIZING ON-DEMAND FOOD DELIVERY USING A MULTI-STEP DECISION-MAKING FRAMEWORK INCORPORATING DEEP REINFORCEMENT LEARNING.

Shahbazian, R., Pugliese, L. D. P., Guerriero, F., & Macrina, G. (2024). Integrating Machine Learning Into Vehicle Routing Problem: Methods and Applications. IEEE Access, 12, 93087–93115. https://doi.org/10.1109/access.2024.3422479

Simoni, M. D., & Winkenbach, M. (2023). Crowdsourced on-demand food delivery: An order batching and assignment algorithm. Transportation Research Part C: Emerging Technologies, 149, 104055. https://doi.org/10.1016/j.trc.2023.104055

Wang, X., Ji, C., Xu, H., & Guo, K. (2025). Research on Dynamic Optimization of Takeout Delivery Routes Considering Food Preparation Time. Sustainability, 17(6), 2771. https://doi.org/10.3390/su17062771

Wu, Q., Han, J., Yan, Y., Kuo, Y. H., & Shen, Z. J. M. (2025). Reinforcement learning for healthcare operations management: methodological framework, recent developments, and future research directions. Health Care Management Science, 28(2), 298. https://doi.org/10.1007/s10729-025-09699-6

Zhang, J., & Van Woensel, T. (2023). Dynamic vehicle routing with random requests: A literature review. International Journal of Production Economics, 256, 108751. https://doi.org/10.1016/j.ijpe.2022.108751

Zhang, Z., Yang, J., Cao, Z., & Lau, H. C. (2025). Neuro-Ins: A Learning-Based One-Shot Node Insertion for Dynamic Routing Problems. IEEE Transactions on Knowledge and Data Engineering. https://doi.org/10.1109/tkde.2025.3580640

Zou, Z., Wang, J., Huang, Y., & Wu, J. (2025). Multi-Agent Pointer Transformer: Seq-to-Seq Reinforcement Learning for Multi-Vehicle Dynamic Pickup-Delivery Problems. arXiv preprint arXiv:2511.17435.

CHAPTER 6

DECOUPLING COMPENSATION EFFECT ON CURRENT CONTROL PERFORMANCE OF SYNCHRONOUS RELUCTANCE MACHINES

Osman Emre Özçiflikçi[1]

Introduction

Synchronous reluctance machines (SynRMs) are used as an alternative to permanent magnet synchronous machines (PMSMs) (Rigon, Haus, Mercorelli, & Zigliotto, 2025) in applications such as electric vehicles, fans, and pumps (Tang et al., 2025). The absence of magnets in their structure provides a low-cost advantage for SynRMs (Babu, Krishna, & Seshadrinath, 2025). Therefore, SynRMs are a popular type of electrical machine in industry and academia (Niewiara, Gierczyński, Tarczewski, & Grzesiak, 2025; V & A, 2025).

As with other types of electrical machines, field-oriented control (FOC) is widely used in the vector control of SynRMs (Kiliç, 2025; Li, Wang, Zhang, Zhao, & Xu, 2021; Paulraj & Obulesu,

[1] Dr., Kırşehir Ahi Evran University, Electrical-Electronic Engineering, Orcid: 0000-0001-8770-020X

2025). In FOC, Clark and Park transforms are used to model the machine on the -dq axis, and control is achieved via -dq axis currents. The most basic feedback structure of the FOC technique is a closed-loop current control system where the -dq axis currents are controlled. The -dq axis currents measured from the machine are compared with the desired -dq axis currents from the system, and the necessary reference voltages are obtained using PI regulators. The obtained reference voltages and pulse width modulation (PWM) technique are used to generate the necessary switching signals for the inverter (Özçiflikçi, Koç, & Bahçeci, 2025).

When examining the mathematical equations of SynRMs, it can be observed that there are cross-coupling terms where the -dq axes interact with each other. In FOC-based SynRM drives, it is necessary to improve of controller performance by applying decoupling compensation to the cross-coupling terms (Chen, Lin, Liang, & Liao, 2021; Ilioudis, 2025; Zhong, Su, Yang, Sun, & Tan, 2025). The high saliency ratio, especially in SynRM, increases the magnetic coupling between the -dq axes, making decoupling compensation terms more pronounced. This causes decoupling compensation to play an important role in maintaining current control quality.

The purpose of this chapter is to emphasize the importance of applying decoupling compensation in FOC structures for SynRM machines and to comprehensively evaluate the effects of applying or not applying compensation on current control, torque output, and overall dynamic performance. Furthermore, using the parameters of a 1.5 kW SynRM experimentally verified in the literature (Lee, Joo, & Yoon, 2024), simulation studies conducted at different mechanical speed values have comparatively revealed the effects of compensation application on performance.

Mathematical Expressions

By using Clark and Park transformations in electrical machine control systems, the machine equations in the abc frame can be converted to the -dq axis and modeled as in SynRM (1-3) (Boztas & Aydogmus, 2022).

$$V_d = R * I_d + L_d * \frac{dI_d}{dt} - w_e * L_q * I_q \quad (1)$$

$$V_q = R * I_q + L_q * \frac{dI_q}{dt} + w_e * L_d * I_d \quad (2)$$

$$T_e = \frac{3 * p}{2} * (L_d - L_q) * I_d * I_q \quad (3)$$

V_d and V_q are the –dq axis voltages (V), I_d and I_q are the –dq axis currents (A), w_e are the electrical speed (rad/s), p pole pairs, L_d and L_q are the –dq axis inductance values (H) and R is the stator resistance (Ω).

As can be seen from (1,2), the term dependent on the q-axis appears in the V_d equation, while the terms dependent on the d-axis appear on the V_q equation. In the FOC schematic given in Figure 1 as decoupling compensation, (4,5) is applied to compensate for the coupling on the -dq axes, and the voltage values to be modulated are determined (Chen et al., 2021).

$$V_d^* = V_d - w_e * L_q * I_q \quad (4)$$

$$V_q^* = V_q + w_e * L_d * I_d \quad (5)$$

Figure 1 Schematic of proposed FOC based SynRM drive.

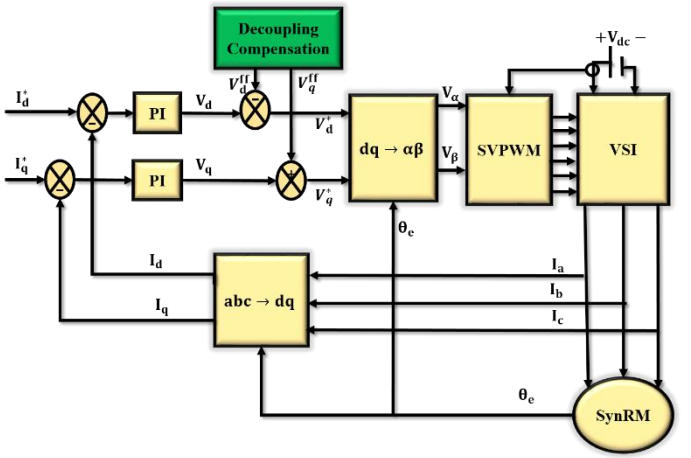

In Figure 1, the other components of the conventionally used FOC-based SynRM drive (space vector PWM (SVPWM), Clark and Park transformations, PI controllers, and Voltage Source Inverter (VSI)) are indicated in gold, while the decoupling compensation block is highlighted in green. The main objective of the chapter is to compare of the drive response with and without the green section to emphasize the importance of implementing decoupling compensation in the SynRM drive.

Simulation Results

Table 1 shows the parameters of the 1.5 kW prototype SynRM and information about the control system (Lee et al., 2024). As can be seen in Table 1, a switching frequency of 10 kHz has been determined for the SVPWM technique in this chapter. Furthermore, I_d^* and I_q^* values have been determined based on the rated current value of 7.5 A_{rms} provided in Table 1. The expected behavior of the SynRM drive is to accurately track the I_d^* and I_q^* references demanded by the system. In this chapter, investigations have been carried out on the behavior of SynRM in the constant torque region. Therefore, as can be seen in Table 1, the SynRM, which has a rated

speed of 3000 rpm, has been operated at mechanical speeds below this value.

In simulation studies, the effects of the decoupling compensation structure are examined when the mechanical speed value is changed using a step function while the I_d and I_q currents are constant, and as a result of step changes in the I_d and I_q currents. The response of the drive is analyzed in cases where decoupling compensation is applied and not applied. First, the step function has been used to change the I_d and I_q currents at different time intervals to analyze both their rise and fall. Accordingly, the I_d and I_q current changes have been compared both at low speed levels (200 rpm) and at high speed levels (2000 rpm) in the constant torque region, with and without compensation applied.

Table 1 Parameters of SynRM and control system (Lee et al., 2024).

Motor Type	SynRM
Rated Power	1.5 kW
DC Link Voltage	311 V
Rated Current	7.5 A_{rms}
Rated Speed	3000 rpm
Rated Torque	4 Nm
Pole Pair	2
Stator resistance	1.3 Ω
d and q axis inductances	$L_d = 78.3\ mH$, $L_q = 20.1\ mH$
Switching Frequency	10 kHz

Figure 2 shows the effects of decoupling compensation at low speed values by determining the mechanical speed value well below the rated speed (200 rpm) using the SynRM parameters given in Table 1. Figure 2 shows the electromagnetic torque, reference I_d and actual I_d currents, reference I_q and actual I_q values, and mechanical speed values. The left column of Figure 2 shows the results for the drive without decoupling compensation applied, while the right column shows the results for the drive with decoupling compensation applied. To examine the effect of I_d and I_q currents on each other at a constant speed, the I_d current changes from 5 A to 3 A in 0.3 seconds and then from 3 A back to 5 A in 0.6 seconds. Similarly, the I_q current changes at 0.2 seconds and 0.5 seconds. In this way, the effects of both axis currents on the drive are analyzed. Interpreting the results obtained from Figure 2, even though there is a delay in the settling time of the I_q current at the start in the drive without decoupling compensation, it generally gives similar results to the drive with decoupling compensation. Accordingly, it can be concluded that the effect of decoupling compensation is not dominant at low speed levels.

Figure 2 Decoupling compensation effect at low speed.

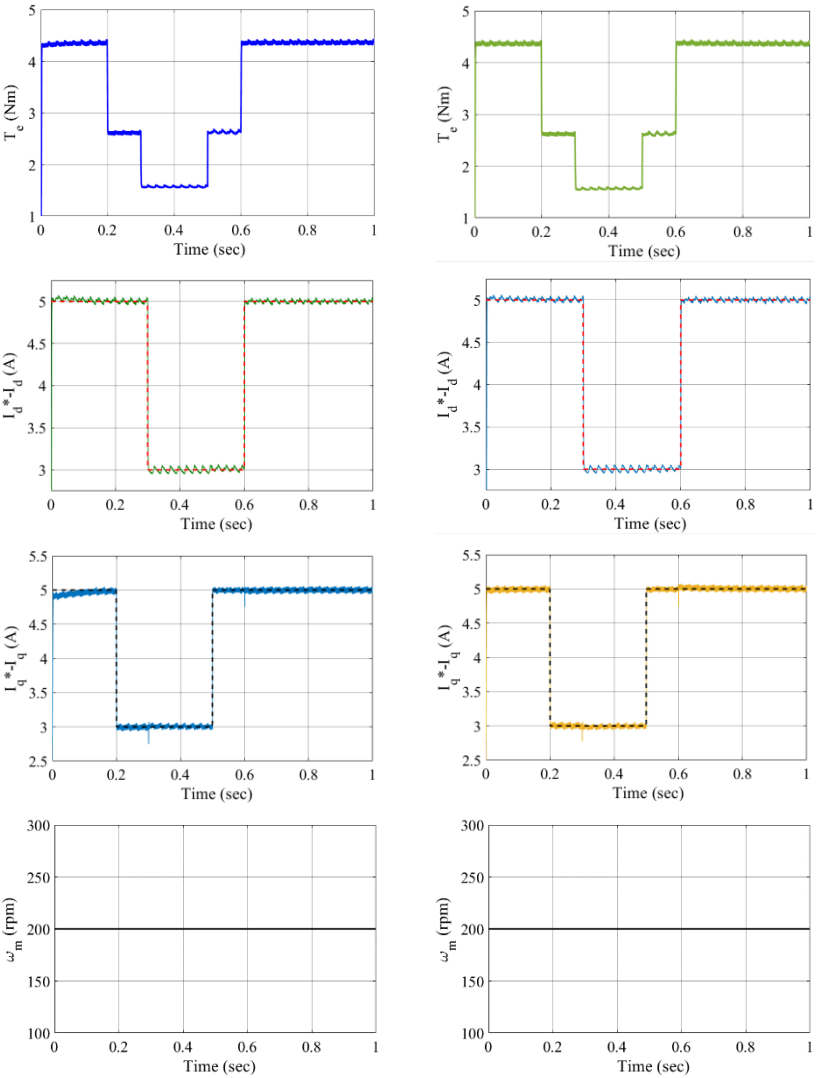

without decoupling compensation

with decoupling compensation

Figure 3 Decoupling compensation effect at high speed.

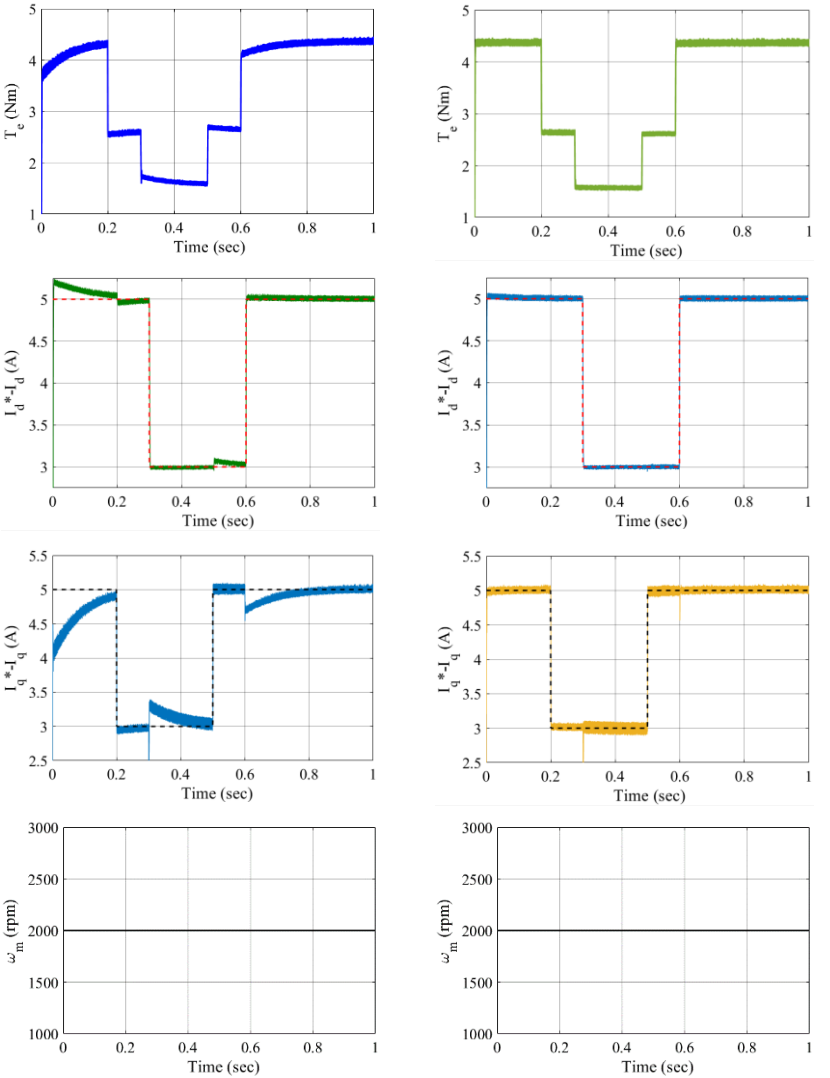

without decoupling compensation

with decoupling compensation

Figure 3 shows that the simulation scenario performed in Figure 2 is applied at a mechanical speed level of 2000 rpm instead of 200 rpm. According to Figure 3, when decoupling compensation is not applied, the drive settles to the reference value much later and the drive performance is significantly lower. Interpreting Figure 3, it can be concluded that applying decoupling compensation at high speed levels is much more important and performance-enhancing for the drive.

Figure 4 Effect of decoupling compensation on speed variation.

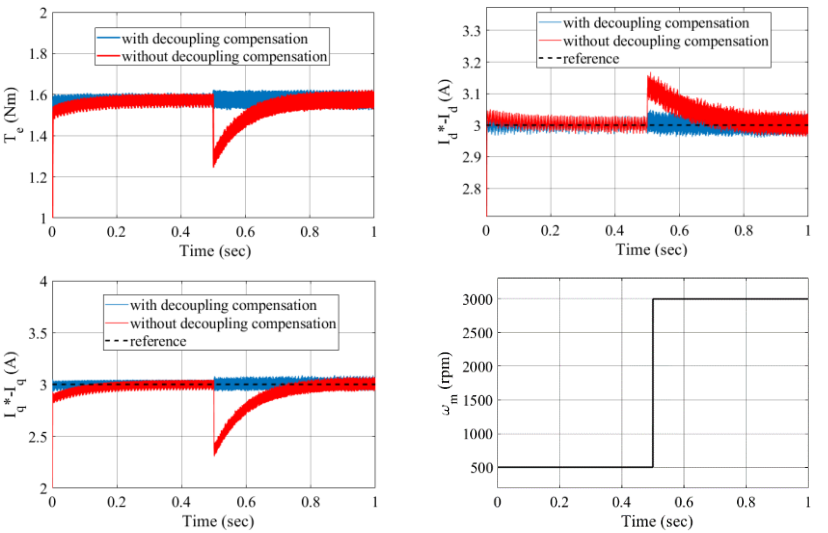

In Figure 4, the reference values for the I_d and I_q currents are set to 3A, and the mechanical speed value is increased from 500 rpm to 3000 rpm in 0.5 seconds using a step function. As can be clearly seen in Figure 4, the control performance of the drive without decoupling compensation is quite low. In quantitative analysis, the actual electromagnetic torque deviated by ~22.5% after the speed change and took time to stabilize at the required torque value. Similarly, the I_q current has deviated by ~20% from the reference value, and the settling time to the reference value has been significantly delayed compared to the drive with decoupling

compensation applied. Examining the I_d current, an overshoot of ~4.8% occurred after the speed change, and the actual I_d value settled to the reference later.

Conclusion

The high performance of SynRM drives, widely used in industry and academia, is an important area of research today. Since SynRMs operate on the principle of generating reluctance torque, their saliency ratios are high. Therefore, it can be anticipated that the application of decoupling compensation is also important. In this book chapter, the performance of drives with and without decoupling compensation applied to SynRMs is compared and evaluated. According to the results, while the application of decoupling compensation does not provide a significant improvement in the drive at low speed levels, it significantly increases the controller performance at high speed levels, both when the currents change and when the speed changes. The results obtained from the simulation studies show that in the drive without decoupling compensation, the electromagnetic torque, I_d and I_q deviated by ~22.5%, ~4.8%, and ~20%, respectively, with the instantaneous change in speed and took longer to settle to the reference values. Since SynRM directly provides torque generation through saliency ratio, the importance of decoupling compensation becomes apparent. Further studies could comparatively investigate the importance and effects of decoupling compensation in PMSMs and SynRM. Additionally, because decoupling compensation terms are dependent on machine parameters, they can cause a decrease in control performance during operation. Therefore, parameter-independent strategies can be improved.

References

Babu, A. C., Krishna, M. S. R., & Seshadrinath, J. (2025). A Semi-Automated ML Architectural Search for Optimal Pipeline Generation for Incipient Stator Inter-turn Fault Diagnosis of SynRM Drive. *IEEE Transactions on Industry Applications*, 1-10. doi: 10.1109/TIA.2025.3619913

Boztas, G., & Aydogmus, O. (2022). Implementation of sensorless speed control of synchronous reluctance motor using extended Kalman filter. *Engineering Science and Technology, an International Journal, 31*, 101066. doi: https://doi.org/10.1016/j.jestch.2021.09.012

Chen, S. G., Lin, F. J., Liang, C. H., & Liao, C. H. (2021). Intelligent Maximum Power Factor Searching Control Using Recurrent Chebyshev Fuzzy Neural Network Current Angle Controller for SynRM Drive System. *IEEE Transactions on Power Electronics, 36*(3), 3496-3511. doi: 10.1109/TPEL.2020.3016709

Ilioudis, V. C. (2025). A Study of MTPA Applied to Sensorless Control of the Synchronous Reluctance Machine (SynRM). *Automation, 6*(1), 11. doi: 10.3390/automation6010011

Kiliç, E. (2025). Deep Reinforcement Learning-Based Controller for Field-Oriented Control of SynRM. *IEEE Access, 13*, 2855-2861. doi: 10.1109/ACCESS.2024.3524156

Lee, H. J., Joo, J. E., & Yoon, Y. D. (2024). Signal Injection Sensorless Control Without Manipulating Convergence Point Based on Symmetrical Auxiliary Angles for Saturated Synchronous Machine. *IEEE Transactions on Industry Applications, 60*(5), 6938-6948. doi: 10.1109/TIA.2024.3416097

Li, C., Wang, G., Zhang, G., Zhao, N., & Xu, D. (2021). Adaptive Pseudorandom High-Frequency Square-Wave Voltage

Injection Based Sensorless Control for SynRM Drives. *IEEE Transactions on Power Electronics, 36*(3), 3200-3210. doi: 10.1109/TPEL.2020.3015704

Niewiara, Ł. J., Gierczyński, M., Tarczewski, T., & Grzesiak, L. M. (2025). An energy-efficient torque optimization strategy with field weakening for a state feedback controller with synchronous reluctance motor drive. *IEEE Transactions on Transportation Electrification*, 1-1. doi: 10.1109/TTE.2025.3634971

Özçiflikçi, O. E., Koç, M., & Bahçeci, S. (2025). Evaluation of Maximum Torque per Ampere Control Method for Interior Permanent Magnet Machine Drives on dSpace with Emphasis on Potential Practical Issues for High Energy Efficiency. *Energies, 18*(15), 4118. doi:10.3390/en18154118

Paulraj, T., & Obulesu, Y. P. (2025). Comprehensive Performance Evaluation of 60 kW PMSM, EESM, and SynRM for Electric Vehicle Traction Under Steady-State and Drive Cycle Conditions. *IEEE Access, 13*, 155916-155939. doi: 10.1109/ACCESS.2025.3606372

Rigon, S., Haus, B., Mercorelli, P., & Zigliotto, M. (2025). Automatic Tuning of Extended Kalman Filter in Sensorless Synchronous Reluctance Motor Drives. *IEEE Open Journal of Power Electronics, 6*, 734-746. doi: 10.1109/OJPEL.2025.3546752

Tang, Q., Jiang, Z., Luo, P., Shen, A., Luo, X., & Xu, J. (2025). SynRM Sensorless MTPA Integrated Control Strategy Based on PWM-Induced Transient Excitation Considering Cross-Saturation Effects. *IEEE Transactions on Power Electronics*, 1-12. doi: 10.1109/TPEL.2025.3623887

V, A., & A, R. (2025). Performance Optimization of Synchronous Reluctance Motor using Adaptive MTPA Curve Fitting with Anti-Windup Current Control. *Results in Engineering, 27*, 106658. doi: https://doi.org/10.1016/j.rineng.2025.106658

Zhong, B., Su, J., Yang, G., Sun, G., & Tan, K. (2025). Unified Optimal Control Method for SynRM in Full-Speed Region Considering Magnetic Saturation. *IEEE Journal of Emerging and Selected Topics in Power Electronics, 13*(1), 675-689. doi: 10.1109/JESTPE.2024.3505297

CHAPTER 7

BEHAVIOR OF LED DRIVERS AGAINST VOLTAGE DIPS: A SIMULATION-BASED STUDY

MURAT DEMİR[1]

1. Introduction

LED-based lighting systems have become a dominant technology in modern power electronics applications and the general lighting industry due to their fundamental advantages such as high efficiency, long lifetime, and low energy consumption [1, 2]. Compliance with international standards such as IEEE 519-2014 [3] and IEC 61000-3-2 [4] is mandatory to ensure these systems operate in harmony with the grid and to limit harmonic current emissions. However, the presence of sensitive semiconductor components and complex driver circuits in these systems increases their vulnerability to short-term voltage dips and other power quality disturbances on the grid [5]. Such transient grid events can cause sudden dips in the DC-link voltage of LED drivers, leading to visible flickering or instantaneous complete blackouts, depending on the immunity level of the driver [6]. The adverse effects of low-frequency flicker on human health and safe modulation limits are defined in IEEE Std

[1] Dr. Öğr. Üyesi, İzmir Bakırçay University, Electrical and Electronics Engineering, Orcid: 0000-0003-4407-9673

1789-2015 [7]. In this context, the IEC 61000-4-11 standard defines internationally recognized reference test scenarios to standardize the immunity of grid-connected equipment against such disturbances [8].

In this study, voltage dip depths of 40%, 70%, and 80% were used as references to examine driver behavior at critical and internationally accepted levels. These levels are the preferred test profiles of the standard and directly correspond to the demanding test conditions specified for equipment in industrial environments where frequent switching events occur, particularly with the introduction of large loads [9, 10]. The selection of these levels ensures that the results obtained are directly comparable with other academic studies in the literature and industrial test reports [1].

There are comprehensive studies in the literature examining the behavior of LED drivers against power quality disturbances. X. Xie and colleagues provided detailed analyses on power factor correction techniques and grid interactions of LED drivers [11]; B. Singh and his team emphasized the system-level importance of the subject by examining the power quality performance of single-stage converters [12]. In the field of experimental studies, S.K. Rönnberg and A. Gil-de-Castro have detailed the immunity differences of different lighting loads against voltage dips and short interruptions [13]. S. Uddin and colleagues evaluated the response of LED lamps to harmonic and power quality events, discussing transient performance criteria [14].

The common conclusion of these studies is that the DC-link capacitor plays a key role in system stability and current regulation, particularly due to its ability to store energy during voltage dips [15]. However, the high costs of experimental testing, difficulties in reproducibility, and the need for specialized test equipment have brought simulation-based approaches to the forefront of power electronics research in recent years [16]. S. Buso and G. Spiazzi

demonstrated the accuracy of digital control and modeling techniques in power electronics [17]; Y. Hu and his team worked on the dynamic modeling of universal input drivers, showing that immunity analysis can be practically performed in a simulation environment [18].

This study aims to advance the current simulation-based approach by analyzing the response of the LED driver based on IEC test profiles without using physical hardware. During the modeling process, a simplified equivalent circuit model based on average values was used, as the effect of microsecond-level switching dynamics on millisecond-level voltage dip events is negligible [17]. This approach reduces simulation complexity, allowing direct focus on the energy balance of the DC-link capacitor and the stability role of the PI controller. The main contribution of the study is to clearly demonstrate the physical limits of controller optimization: despite the PI controller's Anti-windup (AW) strategy, the excessive voltage spike reaching 400 V levels, which occurred in the most challenging 80% dips scenario, could not be prevented by the controller dynamics. This risk was mitigated to manageable levels only by integrating a virtual voltage clamping mechanism (250 V) that models the overvoltage protection (OVP) function into the system. The results obtained provide a solid scientific basis for conducting IEC compliance analyses of LED drivers in a virtual environment and for understanding the necessity of hardware protection structures beyond controller-based solutions, especially during critical transition moments.

2. System Model and Methodology

This section mathematically defines the simplified equivalent circuit of the LED driver, DC-link dynamics, Buck converter model, LED load model, and PI + Anti-windup control structure. The models are created to be suitable for the simplified

system and are used with dip profiles compliant with IEC 61000-4-11.

2.1. LED Driver Equivalent Circuit

The LED driver examined in this study is represented by an "Average Value Model" free from switching frequency dynamics in order to analyze its dynamic behavior under voltage dip scenarios compliant with the IEC 61000-4-11 standard. A standard commercial LED driver consists of PFC (Power Factor Correction), EMI filter, rectifier, DC-link capacitor, and a DC-DC converter stages. However, as shown in similar dip analyses in the literature, during short-term (0–200 ms) voltage dips, the effect of microsecond-level switching dynamics and input filters on the overall energy balance of the system is negligible [18, 19]. Therefore, during the modeling process, the focus was on the system's low-frequency envelope behavior, and switching harmonics were isolated.

The simplified system block diagram is shown in Figure 1, and the basic circuit parameters are summarized in Table 1.

Table 1 Basic components and operating parameters

Parameter	**Description**	**Value**	**Unit**
V_{AC}	Nominal Input Voltage	230	V_{rms}
V_{DC_ref}	Target DC-Link Voltage	210	V
C	DC-Link Capacitor	100	μF
L	Buck Converter Inductor	100	μH
I_{LED_ref}	Target LED Current	2	A
P	Proportional Gain	0.1	—
I	Integral Gain	10	—
AW	Anti-windup Feedback Gain	3	—

Figure 1 Simplified equivalent circuit model of the LED driver

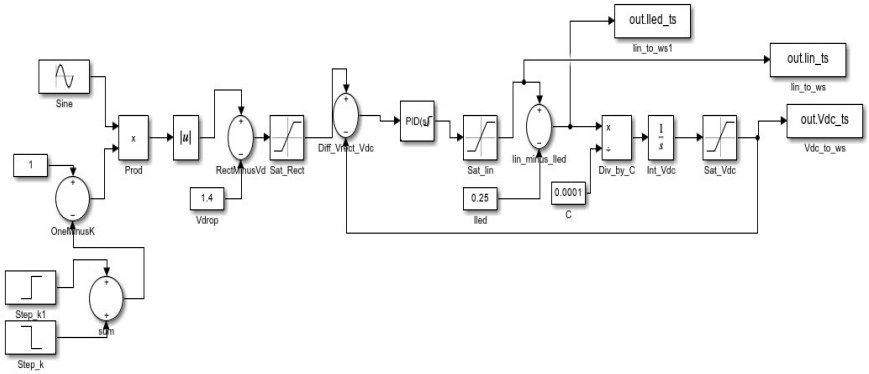

The model consists of an AC-DC full-bridge rectifier, a DC-link capacitor (C) as the main energy storage, a DC-DC converter (Buck converter), and an LED load. In this model, the DC-link capacitor is responsible for supplying energy to the system during voltage dips, and even the slightest change in voltage directly affects the DC-link voltage (V_{DC}).

The rectifier is modeled ideally. The input AC voltage is obtained at the rectifier output as shown in Equation 1. Since the IEC 61000-4-11 test profile directly affects the input signal, this expression changes dynamically during the dip.

$$V_d = \sqrt{2}\,.\,V_{AC}(t) \tag{1}$$

The DC-link voltage is the most critical variable in the system, and the power balance equation on the capacitor is given in Equation 2.

$$C\,\frac{dV_{Dc}}{dt} = i_d(t) - i_{buck}(t) \tag{2}$$

Here, i_d represents the rectifier current drawn from the grid, while i_{buck} represents the average current drawn by the LED driver stage from the DC-link. The rectifier current flows only when the

instantaneous grid voltage is greater than the DC-link voltage ($V_d > V_{DC}$) (Equation 3):

$$i_d(t) = \begin{cases} \frac{V_d(t) - V_{DC}(t)}{R_s}, & V_d(t) > V_{DC}(t) \\ 0, & V_d(t) \leq V_{DC}(t) \end{cases} \quad (3)$$

For the buck converter stage, due to the large difference between the time constant of voltage dips (T_{dip} ≈200 ms) and the time constant of the converter inductor ($\tau = L/R$), the inductor current dynamics are considered quasi-steady. With this approach, an algebraic transfer function is used instead of differential current equations. The voltage across the LED load (V_{LED}) depends on the relationship between the converter duty cycle (D) and the DC-link voltage (Equation 4):

$$V_{led}(t) \approx D(t).V_{DC}(t) \quad (4)$$

The LED string is modeled with an equivalent circuit containing a fixed forward voltage (V_f) and dynamic resistance (r_d). Accordingly, the driver output current (i_{LED}) is obtained using Equation 5:

$$i_{led}(t) = \frac{D(t).V_{DC}(t) - V_f}{r_d} \quad (5)$$

With this modeling approach, the energy discharge characteristic of the DC-link capacitor and the controller's attempt to regulate the current by changing the duty cycle (D) have been efficiently transferred to the simulation environment. The 100 μF DC-link capacitance used in the simulation was deliberately chosen at the limit to clearly observe the rate of energy depletion at IEC dip levels.

2.2. PI Controller Design and Settings

To ensure stable operation of the LED driver both during voltage dips and when the grid recovers, the duty cycle (D(t)) of the

Buck converter is dynamically adjusted by a PI (Proportional–Integral) controller. PI controllers are a standard solution in power electronics applications because they offer zero static error and adjustable transient response [**20**].

The control scheme used in this study aims to regulate the output current around the reference value (I_{ref}) by minimizing the LED current error (e(t)). The block diagram of the control structure is shown in Figure 1. The error signal is defined by Equation 6:

$$e(t) = I_{ref} - i_{led}(t) \tag{6}$$

The unsaturated raw output signal (u(t)) of the PI controller is as shown in Equation 7:

$$\mathrm{u(t)} = \mathrm{K_p e(t)} + \int(\mathrm{K_i e(t)} + \mathrm{K_{aw} e_{aw}(t)})\mathrm{dt} \tag{7}$$

Here, K_p is the proportional gain, K_i is the integral gain, and K_{aw} is the Anti-Windup feedback gain. Due to the physical operating limits of the buck converter, the duty cycle must be in the 0-1 range. Therefore, the controller output is passed through a saturation block (Equation 8):

$$\mathrm{D(t)} = \mathrm{sat(u(t))} = \begin{cases} 1, & \mathrm{u(t)} > 1 \\ \mathrm{u(t)}, & 0 \leq \mathrm{u(t)} \leq 1 \\ 0, & \mathrm{u(t)} < 0 \end{cases} \tag{8}$$

In field applications, especially when the DC-link voltage collapses during a voltage dip, the controller rapidly increases the output (u(t)) to maintain the current, exceeding the physical limit of 1. In the saturation state, the integrator continues to accumulate error, leading to the “wind-up” problem. This situation causes a large overshoot when the grid voltage returns. The AW correction term (e_{aw}) used to prevent this is given in Equation 9:

$$e_{aw} = D(t) - u(t) \tag{9}$$

Thanks to this feedback structure, when the controller reaches saturation, the integrator's overload (wind-up) is dynamically braked, and the system's recovery performance is improved. The controller parameters used are given in Table 1.

2.3. IEC 61000-4-11 Test Profile

The IEC 61000-4-11 standard defines internationally accepted test procedures for evaluating the immunity of equipment connected to low-voltage AC power supplies to short-term voltage dips, interruptions, and voltage fluctuations [8]. The standard classifies test levels in terms of dip depth (%), duration (ms), and phase angle.

In this study, the ideal mains voltage (V_{AC}) is modeled as a function of time as shown in Equation 10.

$$V_{AC}(t) = V_{nom}\, sin(\omega t) \tag{10}$$

Here, V_{nom} is the peak value of the nominal network voltage (311 V). According to IEC 61000-4-11, a voltage dip event is created by reducing the signal amplitude by a factor of k over a specific time interval (Equation 11).

$$v_{AC}(t) = \begin{cases} V_{nom}\sin(\omega t), & t < t0 \\ k.V_{nom}\sin(\omega t), & t0 \le t \le t1 \\ V_{nom}\sin(\omega t), & t > t1 \end{cases} \tag{11}$$

The parameters used in the simulation scenarios are as follows:

- V_{nom} : Nominal input voltage (311 V),
- k: Voltage dip depth (0.6 for 40% dip, 0.3 for 70%, 0.2 for 80%),
- t_0: Start of dip (0.5 s),
- t_1: End of dip (0.7 s),

The dip duration was kept constant at 200 ms in all scenarios, and three different dip levels, as specified by the IEC standard, were tested: 40%, 70%, and 80%. These tests formed the basis for a comprehensive analysis of the LED driver's dynamic immunity response to power grid disturbances of varying severity [8, 13].

3. Simulation Results and Discussion

This section presents the simulation results obtained for the critical 40%, 70%, and 80% voltage dip levels of the IEC 61000-4-11 standard using the methodology and parameters defined in Section 2. The recovery performance of the PI controller and the critical role of DC-link capacitance in the system were evaluated.

3.1. Voltage Sag Response Analysis

Simulations were performed to examine the system response to sag events starting at t=0.5 s and lasting 200 ms (ending at t=0.7 s).

3.1.1. 40% Voltage Dip

This scenario, where the input voltage dips by 40%, represents the least severe impact on the system. As shown in Figure 2, the DC-link voltage (V_{DC}) dipped to approximately 125 V due to the capacitor discharge characteristic. Thanks to the average value model, the net envelope change, free from switching noise, can be observed. At this voltage level, the PI controller increased the duty cycle (D(t)) to minimize the error, but since D(t) remained below the saturation limit of 1, the control loop continued to operate in the linear region. As a result, the deviation in the LED output current was kept at only 11% [21]. This demonstrates that the 100 µF DC-link capacitance and the current controller provide full functional protection against 40% dips. The anti-windup mechanism was not active in this scenario because the controller did not reach saturation

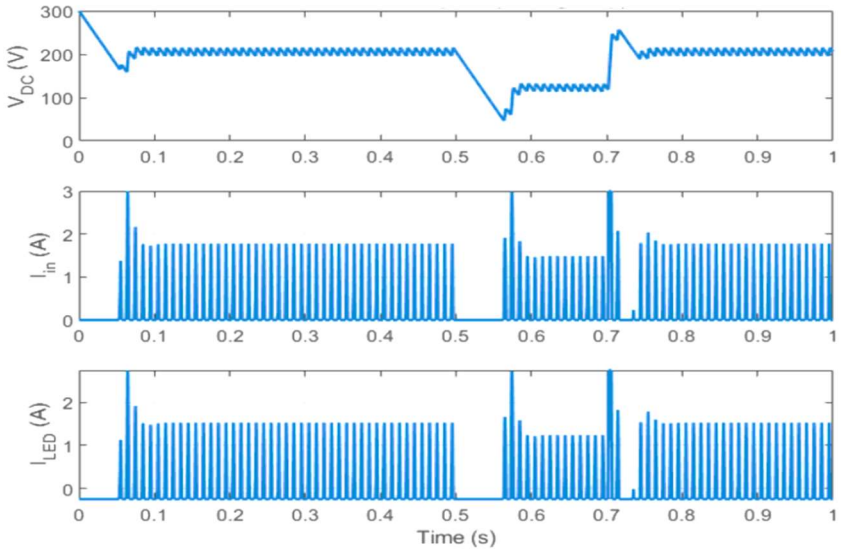

Figure 2 DC-link voltage (V_{DC}) and LED output current (I_{LED}) for a 40% voltage dip

3.1.2. 70% Voltage Dip

In the 70% scenario, where the dip depth increases, the system's energy balance is strained. Figure 3 shows that V_{DC} rapidly dips below the 100 V level. Faced with this deep dip, the PI controller enters saturation by increasing the duty cycle to the physical limit D(t) approximately 1 ($D \approx 1$) to maintain the LED current at the reference value. Due to the insufficient DC-link voltage and the converter reaching saturation, a 44% deviation occurred in the LED current [22]. Although this deviation resulted in noticeable flickering in terms of lighting quality, the system did not lose stability and recovered without entering oscillation after the dip.

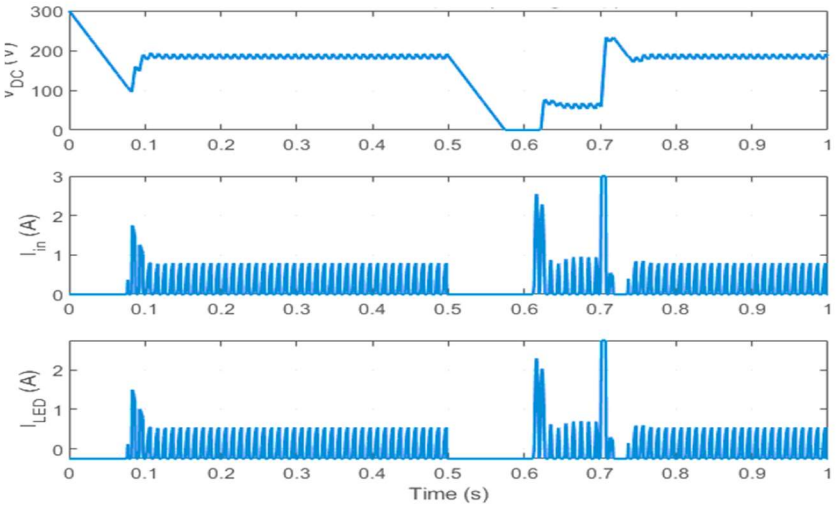

Figure 3. DC-link voltage (V_{DC}) and LED output current (I_{LED}) for a 70% voltage dip

3.1.3. 80% Voltage Dip

In the 80% dip scenario, one of the most demanding tests of the IEC 61000-4-11 standard, the DC-link energy is completely depleted and V_{DC} reaches zero because the input voltage falls below the rectifier conduction threshold (Figure 4). With the interruption of energy flow, the LED current also dips to zero, showing a 100% deviation [23]. This situation is defined in the literature as a critical functional interruption indicating that the device has failed the immunity test [13]. The most critical phase of this scenario is the recovery phase, where the grid voltage returns to its nominal value at t=0.7 s. The high charging current (inrush) drawn from the grid by the discharged capacitor tends to create a dangerous voltage spike approaching 400 V on the DC-link if left uncontrolled. However, the Virtual Overvoltage Protection (OVP) mechanism integrated into the simulation model intervened at this point. As seen in the V_{DC} graph in Figure 4, the voltage rise was successfully clamped at the 250 V level, preventing damage to the driver components.

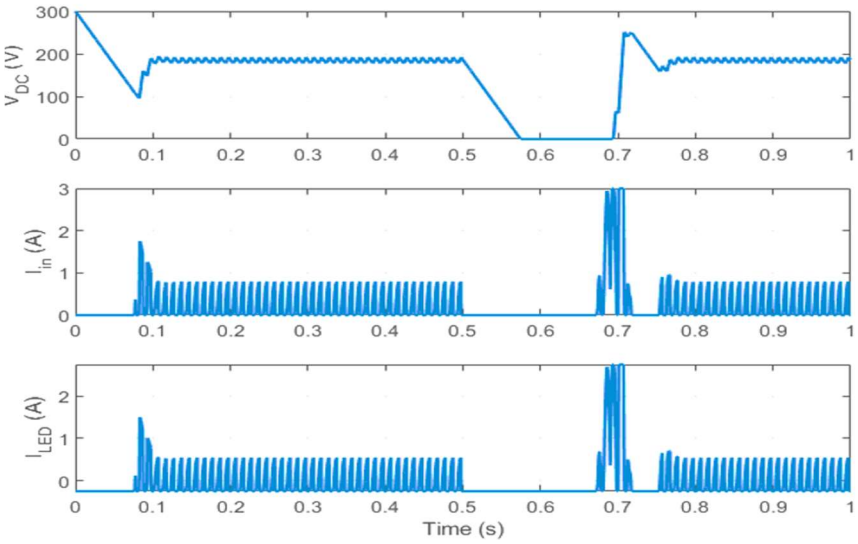

Figure 4. DC-link voltage (VDC) and LED output current (I_{LED}) for an 80% voltage dip

3.2. Immunity Performance Evaluation

The results obtained from three different scenarios are summarized in Table 3. The data in Table 3 confirms the critical role of DC-link capacitance (100 µF) in system immunity [15]. A small increase in dip between 70% and 80% has shifted the system from a partially functional state (44% deviation) to a completely non-functional state (100% deviation). This result scientifically proves that the simplified driver model with a low-capacity DC-link is inadequate for the most demanding conditions of IEC Class 3 [24].

Table 3: LED Driver Response According to Voltage Dip Levels

Dips level	V_{DC} (During Dip)	LED Current Deviation
%40	125	11
%70	100	44
%80	0	100

The most important finding of the analyses is the identification of situations where the controller strategy alone is not sufficient. In the 80% dip scenario, although the PI controller's Anti-Windup feature limited integral accumulation, it could not compensate for the physical lack of energy (DC-link collapse). Furthermore, voltage spikes during recovery are a phenomenon that develops much faster than the bandwidth of the control loop. Therefore, the 250 V active clamping strategy applied in this study has proven the necessity of hardware protection measures (varistors, active OVP circuits, etc.) in the simulation environment. The theoretical peaks produced by an ideal rectifier model have been brought within realistic and safe limits thanks to this protection mechanism [25].

4. Conclusions and Future Work

This study comprehensively examined the behavior of a typical LED driver power stage against 40%, 70%, and 80% voltage dip scenarios defined in the IEC 61000-4-11 standard. The analyses employed an average-value-based circuit model, free from switching dynamics, and a PI + Anti-Windup-based current control structure. This approach reduced simulation complexity while clearly revealing the energy buffering capacity of the DC-link capacitor and the stability limits of the control loop.

Simulation results show that the driver exhibited three different response regions depending on the depth of voltage dip:

Full Functionality (40% Dip): The DC-link voltage remained within safe limits and the controller was able to regulate the current without reaching saturation.

Partial Functionality/Flicker (70% Dip): Energy balance was disrupted, the controller reached saturation, and noticeable fluctuations occurred in the light output; however, the system maintained its stability.

Functional Interruption and Overvoltage Risk (80% Dip): In this most critical scenario, where DC-link energy was completely depleted, the system temporarily lost its functionality.

The most important finding of the study emerged during the grid recovery phase after the 80% dip. Sudden voltage surges (reaching 400 V levels) that threaten hardware safety when left uncontrolled were observed. Simulation results proved that this risk cannot be prevented by controller parameters (PI+AW) alone; it is imperative to integrate a 250 V clamping mechanism that models an active overvoltage protection function into the system. This finding confirms that not only steady-state performance but also hardware protection measures against grid transition events are critical in LED driver design.

In light of the results obtained and within the scope of the study, the following recommendations are made for future research:

Comparison with Detailed Switching Model: Verification of transient regime accuracy by comparing the average value model used in this study with full-switching models that include high-frequency switching dynamics.

Design of Physical Protection Circuits: Design and test the clamping structure idealized in the simulation at the physical circuit level using an inrush current limiter (NTC/Relay), varistor (MOV), or active semiconductor switches.

Advanced Control Strategies: Investigation of the effect of model-based predictive control (MPC) or nonlinear control methods on recovery performance for deep dip scenarios where the PI + AW structure is insufficient [26].

DC-Link Optimization: Optimization of the DC-link capacitance value or investigation of hybrid energy storage (e.g.,

supercapacitor-assisted) architectures to increase energy continuity during critical dip durations.

Photometric Analysis: Detailed experimental measurements of the effect of electrical deviations on light quality as perceived by the human eye (e.g., flicker index).

In conclusion, this study provides a comprehensive evaluation of LED drivers in terms of both control theory and circuit protection requirements in response to IEC voltage dips, establishing an academic reference for reliable driver design.

References

[1] Alonso JM, Viña J, Vaquero DG, Martínez G, Osorio R. Analysis and design of the integrated double buck-boost converter as a high-power-factor driver for power-LED lamps. IEEE Trans Ind Electron. 2012;59(4):1689–97. https://doi.org/10.1109/TIE.2011.2109342

[2] Wang Y, Alonso JM, Ruan X. A review of LED drivers and related technologies. IEEE Trans Ind Electron. 2017;64(7):5754-65. https://doi.org/10.1109/TIE.2017.2677335

[3] IEEE Std 519-2014. IEEE recommended practice and requirements for harmonic control in electric power systems. New York: IEEE; 2014. https://doi.org/10.1109/IEEESTD.2014.6826459

[4] IEC 61000-3-2. Electromagnetic compatibility (EMC) - Part 3-2: Limits - Limits for harmonic current emissions (equipment input current ≤16 A per phase). Geneva: International Electrotechnical Commission; 2018.

[5] Bollen, M.H. (2000) Understanding Power Quality Problems—Voltage Sags and Interruptions. IEEE Press, New York. https://doi.org/10.1109/9780470546840

[6] Gil-de-Castro A, Rönnberg SK, Bollen MH. Light intensity variation (flicker) and harmonic emission related to LED lamps. Electr Power Syst Res. 2017; 146:107–114. Doğru DOI Linki: https://doi.org/10.1016/j.epsr.2017.01.026

[7] IEEE Std 1789-2015. IEEE Recommended Practice for Modulating Current in High-Brightness LEDs for Mitigating Health Risks to Viewers. New York: IEEE; 2015. doi:10.1109/IEEESTD.2015.7118618

[8] IEC 61000-4-11. Electromagnetic compatibility (EMC) – Voltage dips, short interruptions and voltage variations immunity tests. 2nd ed. Geneva: International Electrotechnical Commission; 2017.

[9] IEEE Std 1564-2014. IEEE Guide for Voltage Sag Indices. New York: IEEE; 2014. doi: 10.1109/IEEESTD.2014.6842577

[10] CIGRÉ. Voltage quality in electrical power systems. Paris: CIGRÉ; 1999. Technical Brochure 36.

[11] X. Xie, C. Zhao, L. Zheng and S. Liu, "An Improved Buck PFC Converter With High Power Factor," in IEEE Transactions on Power Electronics, vol. 28, no. 5, pp. 2277-2284, May 2013, doi: 10.1109/TPEL.2012.2214060.

[12] B. Singh, S. Singh, A. Chandra and K. Al-Haddad, "Comprehensive Study of Single-Phase AC-DC Power Factor Corrected Converters With High-Frequency Isolation," in IEEE Transactions on Industrial Informatics,

vol. 7, no. 4, pp. 540-556, Nov. 2011, doi: 10.1109/TII.2011.2166798.

[13] Rönnberg SK, Gil-de-Castro A. Immunity of LED lamps to voltage dips and short interruptions. In: 2014 International Conference on Lightning Protection (ICLP); 2014. p. 1918–21. https://doi.org/10.1109/ICLP.2014.6973441

[14] S. Uddin, H. Shareef, A. Mohamed and M. A. Hannan, "An analysis of harmonics from LED lamps," 2012 Asia-Pacific Symposium on Electromagnetic Compatibility, Singapore, 2012, pp. 837-840, doi: 10.1109/APEMC.2012.6238014.

[15] S. Wang, X. Ruan, K. Yao, S. -C. Tan, Y. Yang and Z. Ye, "A Flicker-Free Electrolytic Capacitor-Less AC–DC LED Driver," in IEEE Transactions on Power Electronics, vol. 27, no. 11, pp. 4540-4548, Nov. 2012, doi: 10.1109/TPEL.2011.2180026.

[16] Rashid MH. Power Electronics Handbook: Devices, Circuits and Applications. 4th ed. Butterworth-Heinemann; 2017. https://doi.org/10.1016/C2016-0-00847-1

[17] Buso, S., & Mattavelli, P. (2015). Digital Control in Power Electronics, 2nd Edition. Synthesis Lectures on Power Electronics, 5(1), 1–229. https://doi.org/10.2200/s00637ed1v01y201503pel007

[18] . Hu, L. Huber and M. M. Jovanović, "Single-Stage, Universal-Input AC/DC LED Driver With Current-Controlled Variable PFC Boost Inductor," in IEEE Transactions on Power Electronics, vol. 27, no. 3, pp. 1579-1588, March 2012, doi: 10.1109/TPEL.2010.2082564.

[19] C. -A. Cheng, H. -L. Cheng and T. -Y. Chung, "A Novel Single-Stage High-Power-Factor LED Street-Lighting

Driver With Coupled Inductors," in IEEE Transactions on Industry Applications, vol. 50, no. 5, pp. 3037-3045, Sept.-Oct. 2014, doi: 10.1109/TIA.2014.2304585.

[20] Åström KJ, Hägglund T. PID controllers: theory, design, and tuning. 2nd ed. Instrument Society of America; 1995. ISBN: 978-1556175169.

[21] M. Martins, M. S. Perdigão, A. M. S. Mendes, R. A. Pinto and J. M. Alonso, "Analysis, Design, and Experimentation of a Dimmable Resonant-Switched-Capacitor LED Driver With Variable Inductor Control," in IEEE Transactions on Power Electronics, vol. 32, no. 4, pp. 3051-3062, April 2017, doi: 10.1109/TPEL.2016.2575918.

[22] D. Gacio, J. M. Alonso, J. Garcia, L. Campa, M. J. Crespo and M. Rico-Secades, "PWM Series Dimming for Slow-Dynamics HPF LED Drivers: the High-Frequency Approach," in IEEE Transactions on Industrial Electronics, vol. 59, no. 4, pp. 1717-1727, April 2012, doi: 10.1109/TIE.2011.2130503.

[23] Y. Qiu, L. Wang, H. Wang, Y. -F. Liu and P. C. Sen, "Bipolar Ripple Cancellation Method to Achieve Single-Stage Electrolytic-Capacitor-Less High-Power LED Driver," in IEEE Journal of Emerging and Selected Topics in Power Electronics, vol. 3, no. 3, pp. 698-713, Sept. 2015, doi: 10.1109/JESTPE.2015.2433918.

[24] Li S, Tan SC, Hui SY. A buck-boost-flyback integrated converter with a single switch for LED driving with low-frequency flicker-free characteristic. IEEE Trans Ind Electron. 2017;65(3):2183-93. https://doi.org/10.1109/TIE.2017.2736484

[25] D. G. Lamar, A. Fernandez, M. Arias, M. Rodriguez and J. Sebastian, "A Unity Power Factor Correction Preregulator with Fast Dynamic Response Based on a Low-Cost Microcontroller," APEC 07 - Twenty-Second Annual IEEE Applied Power Electronics Conference and Exposition, Anaheim, CA, USA, 2007, pp. 186-192, doi: 10.1109/APEX.2007.357513.

[26] M. Arias, D. G. Lamar, F. F. Linera, D. Balocco, A. Aguissa Diallo and J. Sebastián, "Design of a Soft-Switching Asymmetrical Half-Bridge Converter as Second Stage of an LED Driver for Street Lighting Application," in IEEE Transactions on Power Electronics, vol. 27, no. 3, pp. 1608-1621, March 2012, doi: 10.1109/TPEL.2011.2164942.

CHAPTER 8

COMPREHENSIVE DESIGN AND FEA-BASED EVALUATION OF V-SHAPED INTERIOR PMSM FOR SUSTAINABLE E-MOBILITY

CELALETDİN AKGÜL[1]
YÜCEL ÇETİNCEVİZ[2]

Introduction

The widespread consumption of fossil fuels in the transportation, industrial, and energy sectors has led to severe air pollution and climate change, creating a global environmental problem (Helmers ve Marx, 2012: 14). This situation is closely related to increasing energy expenditures and excessive dependence on fossil fuels. As a solution to these issues, electric vehicle (EV) technology has emerged. EVs offer a significant opportunity for a sustainable future due to their potential to reduce emissions, increase energy efficiency, and minimize environmental impact (Alanazi, 2023: 6016).

[1] Lecturer, Kastamonu University, Taskopru Vocational School, Department of Electronics and Automation, Orcid: 0000-0001-7214-9478
[2] Assoc.Prof.Dr., Kastamonu University, Department of Electrical and Electronics Engineering, Orcid: 0000-0001-6834-9442

The widespread adoption of EVs is primarily determined by their low-emission and high-efficiency characteristics (Alanazi, 2023; Gobbi vd., 2024). Within the powertrain system, battery systems and traction inverters are essential components, while the electric motor represents a critical element in the EV ecosystem. One of the primary advantages of electric motors over internal combustion engines (ICEs) is the simplification of the power transmission system (Gobbi vd., 2024). Unlike ICEs, which require complex differentials and multi-speed gearboxes, electric motors can operate efficiently over a wide range of torque and speed, often eliminating the need for such mechanical systems. This significantly reduces mechanical losses caused by friction, thereby improving overall energy efficiency. EVs, with fewer moving parts, provide lighter, more compact, and low-maintenance drive systems, thereby enhancing both performance and reliability (Un-Noor vd., 2017: 1217).

A wide variety of electric motors are used in EVs and industrial applications. These include Induction Motors, Brushed and Brushless DC Motors, Switched Reluctance Motors, and Synchronous Motors (Zeraoulia, Benbouzid ve Diallo, 2006: 1756). Although each type offers distinct advantages and disadvantages, in recent years, Permanent Magnet Synchronous Motor (PMSM) technology has gained significant attention for integration into EV applications. PMSM design is a multidisciplinary and complex process that requires optimization of electromagnetic performance, as well as dimensional and structural parameters. Due to their ease of manufacturing, advantages such as low cost, high durability, and efficiency have made them the preferred traction motor type for many manufacturers; however, PMSMs have gradually replaced them to a large extent (Rimpas vd., 2023; Sieklucki, 2021).

PMSMs are divided into two main categories: inner-rotor and outer-rotor types (Quoc ve Huu, 2024). The selection of rotor type

depends on several factors, including vehicle speed, torque, size, weight, and cooling requirements (Gobbi vd., 2024). For applications requiring high speed and rapid dynamic response, interior-rotor designs are preferred. Based on the rotor configuration, permanent magnets can be mounted on the surface or embedded inside the rotor. Interior Permanent Magnet Synchronous Motors (IPMSMs) are widely preferred in electric vehicle applications due to the mechanical durability of the magnets embedded within the rotor, which counteracts centrifugal force at high speeds. The embedded magnets provide mechanical robustness, efficiency, and high speed capability in motors (Du et al., 2022). IPMSMs additionally generate reluctance torque. The output torque achieved by IPMs is higher than that of SPMs (Dwivedi vd., 2010).

In the design of internally rotor-mounted PMSMs, the geometric shape and position of the magnets within the rotor directly and effectively influence the motor's performance. Various types of magnets are available in this field. Various magnets have been developed, including V-shaped, U-shaped, flat block, spoke-type, and multi-layered configurations (Murali and Ushakumari, 2020; Hwang et al., 2018; Ying et al., 2017). Comparative analyses of IPMSMs show that V-shaped magnets exhibit superior performance compared to other magnet types (Balta et al., 2023; Liu et al., 2016; Yan et al., 2017).

One of the most commonly used permanent magnets in electric motors is NdFeB magnets, due to their high coercivity (Hc), high magnetization (Br), and high maximum energy product (Hirosawa et al., 2017; Vlachou et al., 2024; Genç et al., 2025). The magnetic properties of NdFeB magnets increase motor efficiency, minimize energy losses, and extend the range of electric vehicles due to the energy savings they provide (Desai et al., 2023). The strong magnetic field produced by NdFeB magnets enables compact and lightweight designs in the motor section of electric vehicles,

providing high power and torque density (Desai et al., 2023). The magnetic stability of NdFeB magnets, high temperature resistance, and reliability increase the reliability and lifespan of motor systems, ensuring consistent performance over time (Genç, Todd, & Mumtaz, 2025). All these features make NdFeB magnets an important component in electric vehicle drive systems in terms of efficiency, compactness, and performance.

This study presents an internally rotor-mounted PMSM design operating at a nominal speed of 1100 rpm, featuring 94% efficiency and a nominal output power of 1.4 kW. The magnet placement embedded in the rotor adopts a structure that is mechanically robust and capable of stable operation. During the design process, numerous criteria such as electromagnetic performance, torque, structural integrity, and cost were addressed using a holistic approach. To evaluate the accuracy of the motor design, finite element analysis (FEA) data was used for verification.

Design Requirements and Analytical Sizing

Motor design for electric motors requires specific design criteria in terms of operating conditions, expected performance levels, and efficiency requirements. Among these criteria, high starting torque, compact physical structure, high power density, wide speed-torque range, and high efficiency are paramount. The design parameters determined according to the design criteria are presented in detail in Table 1.

Table 1. Initial Design Parameters of the PMSM

DC Supply Voltage	48 V
Motor Output Power	1400 W
Motor Torque	12.15 Nm
Motor Speed	1100 RPM
Efficiency	%85
Current Density	<6
Slot Fill Factor	% 40 - % 60

In the PMSM design process, the initial step is to calculate the output gear ratio. This ratio determines the motor's design dimensions and performance parameters. The basic formulas and methods of PMSM design are discussed in detail in the equations. The connection between the motor's power, performance characteristics, and rotor diameter and length parameters ($D_{is}^2 l$) is the calculation of the air gap power (S_{gap}). This calculation forms the basis for the subsequent stages of the design process (Gürdal, 2001).

$$S_{gap} = m * E_{ph} * I_{ph} \quad (1)$$

The input apparent power (S) is expressed in Equation (2) (Gürdal, 2001).

$$S = m * V_{ph} * I_{ph} = \frac{P_{out}}{\eta_d * \cos(\varphi)} \quad (2)$$

In addition, considering an m-phase machine with one circuit per phase, the developed kVA (S) from the armature design is obtained from the induced electromotive force (E_{ph}) and the phase current (I_{ph}) in the armature (Gürdal, 2001).

$$S = m\left(\sqrt{2} * f * \phi * T_{ph} * K_w\right)\left(I_{ph}\right)x10^{-3}kVA \quad (3)$$

By noting that $f = pn_s/2$, $I_z = I_{ph}$ (since there is only one circuit per phase), and $Z = 2mT_{ph}$, Equation (4) can be rearranged as follows (Gürdal, 2001).

$$S = \frac{\pi}{2\sqrt{2}}(p\phi)(I_z Z)n_s * K_w x10^{-3} \quad (4)$$

The total magnetic flux in the air gap of the machine is referred to as the total magnetic loading. The average flux density in the air gap of the machine is known as the *specific magnetic loading* (B_{avg}). Accordingly, it is expressed in Equations (5) and (6) (Gürdal, 2001).

$$\text{Total Magnetic Loading} = p\phi \quad Wb \quad (5)$$

and

$$B_{avg} = \frac{p\phi}{\pi * D * L} \; T \tag{6}$$

The total ampere-conductors distributed around the armature (or stator) periphery are referred to as the *total electric loading*. The number of armature (or stator) ampere-conductors per meter of the air-gap periphery is known as the *specific electric loading* (*ac*). Accordingly, it is expressed in Equations (7) and (8) (Gürdal, 2001).

$$specific\ electric\ loading \; = I_z Z \; amper - \text{Conductor} \tag{7}$$

and

$$ac = \frac{I_z * Z}{\pi * D} \; amper - \text{Conductor}/m \tag{8}$$

By substituting the values of *(pΦ)* and *(I_zZ)* from Equations (6) and (8) into Equation (4), the following equation is obtained (Gürdal, 2001).

$$S = \frac{\pi}{2\sqrt{2}}\left(\pi * D * L * B_{avg}\right)(\pi * D * ac) n_s K_w x 10^{-3} \tag{9}$$

$$S = \left(1.11 * \pi^2 * B_{avg} * ac * K_w x 10^{-3}\right) D^2 L n_s \tag{10}$$

$$S = C_o * D^2 * L * n_s \tag{11}$$

Equation (11) represents the output equation of an AC machine, while Equation (12), denoted as C_o, is known as the output coefficient (Gürdal, 2001).

$$C_o = 1.11 * \pi^2 * B_{avg} * ac * K_w x 10^{-3} \tag{12}$$

The value of D^2L for AC machines is obtained from Equation (11). The next step in the calculation involves decomposing it into the *D* and *L* components.

The pole pitch (τ_p) is the physical distance between two adjacent poles corresponding to 180 electrical degrees. For the stator

or rotor, the pole pitch is related to the machine diameter (D) and the number of pole pairs (p) and is expressed by Equation (12) below (Boldea ve Tutelea, 2009; Boldea ve Nasar, 2010; Gieras, 2009; Pyrhonen vd., 2013; Lipo, 2017; Izanlo vd., 2020).

$$\tau_p = \frac{\pi * D}{p} \tag{13}$$

The aspect ratio (λ) is an important parameter that must fall within a specific range to achieve an optimal motor design. For a PMSM with two pole pairs, the aspect ratio should be between 0.6 and 3 to ensure efficient operation and the desired motor characteristics. The relationship between the aspect ratio and the pole pitch is given in Equation (13) (Boldea ve Nasar, 2010).

$$\lambda = \frac{L}{\tau_p} = \frac{p * L}{\pi * D} \qquad 0.6 < \lambda < 3 \tag{14}$$

When the aspect ratio is assigned a value between 0.6 and 3, the proportional relationship between D and L can be determined (Boldea ve Nasar, 2010). From the value of D^2L, the individual values of D and L are then obtained. In Equation (14), the inner diameter of the stator is expressed as follows.

$$D = \frac{p * L}{\lambda * \pi} \tag{15}$$

The induced phase voltage expressed in Equation (15) is determined by the number of turns per phase (w_a), the frequency (f), and the magnetic flux per pole (Φ). Furthermore, Equation (16) states that the magnetic flux per pole depends on the average air-gap flux density (B_g), the pole pitch (τ_p), and the stack (core) length. By combining these two equations, the number of turns per phase can be calculated (Kartal ve Arabul, 2022).

$$E = \frac{2\pi}{\sqrt{2}} * k_w * w_a * f * \phi \tag{16}$$

The flux per pole is calculated as shown in Equation (17) (Kartal ve Arabul, 2022).

$$\phi = \frac{2}{\pi} * B_{g*}\tau_p \tag{17}$$

The number of turns per phase is calculated as shown in Equation (18) (Soleimani ve Gholamian, 2013).

$$wa = \frac{E}{4.44*f*\phi*k_w} \tag{18}$$

The total number of conductors is calculated as shown in Equation (19) (Pyrhonen vd., 2013; Soleimani ve Gholamian, 2013).

$$Z = 2 * m * a \tag{19}$$

The number of conductors per slot is calculated as shown in Equation (20) (Pyrhonen vd., 2013; Soleimani ve Gholamian, 2013).

$$Z_o = \frac{Z}{N_s} \tag{20}$$

Here, Z_o is the number of conductors per slot, Z is the total number of conductors, and N_s is the number of stator slots.

The phase current is obtained as shown in Equation (21) (Gürdal, 2001).

$$I_{ph} = \frac{S}{3*V_{ph}*cos\phi*\eta} \tag{21}$$

Copper losses are proportional to the square of the current density, and the temperature rise is dependent on these losses. The stator current density is selected within the range of 3–6.5 A/mm² to ensure efficiency without exceeding the permissible temperature limits (Pyrhonen vd., 2013). The conductor cross-sectional area is calculated according to these values, as shown in Equation (22) (Soleimani ve Gholamian, 2013).

$$A_{con} = \frac{I_s}{J} \tag{22}$$

The slot fill factor varies depending on the design requirements and constraints of the electrical machine. Generally, a slot fill factor between 0.4 and 0.6 is considered suitable for most applications (Meier, 2008). The calculation of the slot area is given in Equation (23).

$$A_{sl} = \frac{A_{con} * Z_o}{k_{fill}} \tag{23}$$

The detailed design of the stator slot can be developed based on the slot pitch. The structure of the stator slot is shown in Figure 1.

Figure 1 Stator Slot

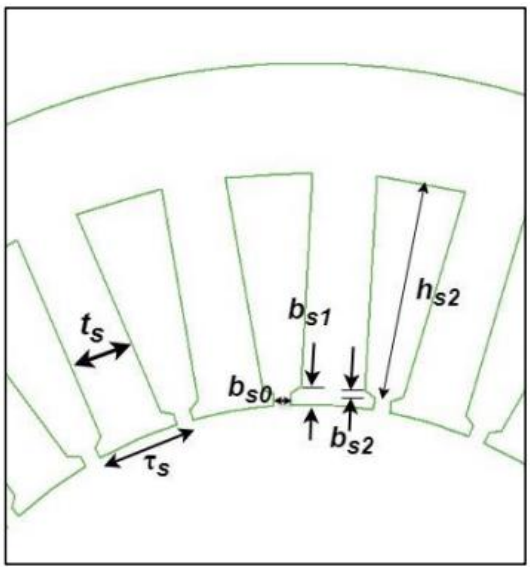

As shown in Equations (24–29), variations in slot dimensions affect motor performance parameters, including efficiency, air-gap flux density, cogging torque, flux path, and machine weight (Liu, 2015).

$$t_s \approx (0.4 - 0.6)\tau_p \quad (24)$$

$$d_s \approx (3 - 7)t_s \quad (25)$$

$$b_s = \tau_p - t_s \quad (26)$$

$$b_{s0} \approx (0.1 - 0.5)b_s \quad (27)$$

$$d_{s0} \approx (0.1 - 0.5)b_s \quad (28)$$

$$d_{s1} \approx (0.1 - 0.5)b_s \quad (29)$$

To determine the stator tooth width, the total air-gap flux must first be calculated. This calculation is given in Equation (30) (Ammar, 2023).

$$\phi_{total} = B_g * \pi * D * L \quad (30)$$

The flux under the pole is determined as shown in Equation (31) (Ammar, 2023).

$$\phi_p = \frac{\phi_{total}}{2} \quad (31)$$

The stator tooth flux is given in Equation (32) (Ammar, 2023).

$$\phi_{st} = B_{st} * W_{st} * L * k_i \quad (32)$$

The stator tooth width is calculated as shown in Equation (33) (Ammar, 2023).

$$W_{st} = \frac{\phi_{st}}{B_{st} * L * k_i} \quad (33)$$

The stacking factor (k_i) in motor design varies between 0.8 and 0.99 (Yulianto vd., 2021).

The width of the stator yoke is expressed as follows (Yulianto vd., 2021).

$$W_{sy} = \frac{\phi_p}{2*B_{st}*L*k_i} \quad (34)$$

In electric motors, the air gap is a critical design parameter that directly affects the passage of magnetic flux. The accurate determination of the air gap significantly influences the motor's efficiency, torque, manufacturability, and overall performance.

$$\mathrm{g} = 3.10^{-3}\left(\sqrt{\frac{2p}{2}}\right).\tau_p \quad (35)$$

The air-gap estimation based on the pole pitch approach is calculated as a function of geometric parameters such as the number of poles and the pole pitch, as given in Equation (35) (Cetinceviz, 2025).

Rationale and Characteristics of the Designed Motor

The pole-slot configuration has a direct impact on the electromagnetic performance in electric motor design. As the number of poles increases, significant variations occur in the electromagnetic torque and output voltage frequency. It has been observed that a higher pole count increases magnetic saturation between the stator and rotor, thereby reducing efficiency. For this reason, a 10-pole configuration was selected within the 6- to 12-pole range.

In PMSM designs intended for EV applications, the topology defined by the direction of magnetic flux plays a crucial role in motor performance. Depending on the orientation of the magnetic flux with respect to the rotation axis, the flux topology is classified into two categories: axial flux and radial flux. Radial-switched PMSM is widely used in low and medium power systems due to its high efficiency, torque-to-weight ratio, and robust reliability. With its compact size and robust construction, it is widely used in electric vehicles, pumps, and industrial drives (Samanta et al. 2025). In this

motor topology, the magnetic flux passes perpendicular to the axis of rotation through the air gap between the rotor and stator to achieve energy conversion.

Radial flux motors offer efficient acceleration and high traction performance in electric vehicles due to their high torque density (El Hadraoui et al., 2022; Nye et al., 2025). These motors stand out for their consistent performance characteristics and generally provide effective cooling in heat distribution due to their cylindrical geometry (Zadorozhniuk et al., 2024). Production processes have been standardised and assembly operations simplified due to the long-standing use of radial flux topology. Electric vehicle manufacturers prefer them because they are suitable in terms of production and cost.

PMSMs are divided into two different designs: internal rotor and outer rotor. The determination of the rotor type in electric motor design depends on various factor parameters such as speed, torque, size, cooling system, and weight. In applications requiring high speed and dynamic response, internal rotor configurations are found to be more suitable.

There are two types of rotors in PM machines: surface-mounted (SM) and interior- mounted (IM). In high-speed operations, PMs must be fixed in the rotor against high centrifugal forces. In IPM topology, magnet strength, which remains constant in the motor and ensures stable operation, is frequently used in high-speed applications (Xing et al., 2010; Dong et al., 2016).

The V-shaped magnet arrangement in PMSM design offers various performance advantages such as high torque density, low torque ripple, and a wide speed range (Lin et al., 2025). The V-shaped magnet structure concentrates the magnetic flux within the rotor, achieving a high magnetic flux density in the air gap and demonstrating high starting torque and rapid acceleration

performance. The V-shaped magnet placement improves the demagnetization resistance capability by increasing the magnetic salience ratio and ensures the motor's operation in the constant power region (Zadorozhniuk et al., 2024). The embedding of magnets within the motor provides resistance to centrifugal forces and demagnetization, while the combined use of magnetic torque and reluctance torque optimizes torque efficiency (Hahlbeck and Gerling, 2008).

Figure 2 a) Surface-Mounted PMSM (SPMSM) and b) Interior PMSM (IPMSM) (Kilmartin, 2016)

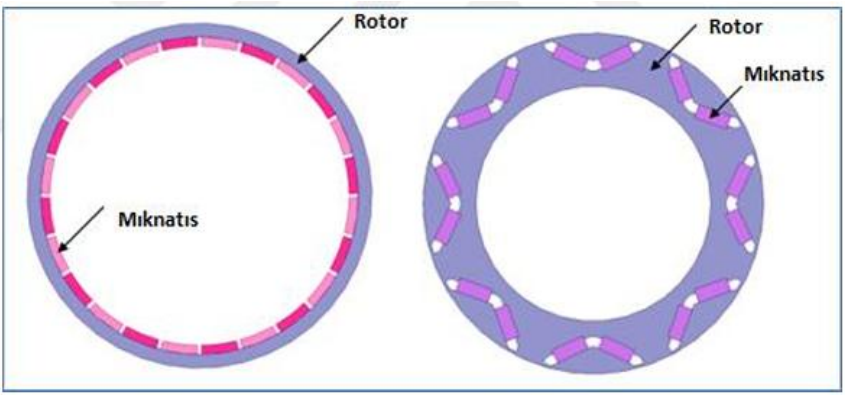

Source: (Kilmartin, 2016)

One of the factors affecting efficiency in electric motor design is core losses. To reduce these losses, silicon steel sheets with low core loss (W/kg) properties are widely used. In this study, JFE 35JN270 grade silicon steel was used in the motor laminations for the rotor and stator cores in the PMSM design. This material is highly suitable for PMSM designs in terms of efficiency due to its high magnetic permeability and low hysteresis loss. The B-H characteristic curve shown in Figure 3 demonstrates that this material provides low magnetic field strength (H) and high magnetic flux density (B).

Figure 3 B–H Curve of 35JN270

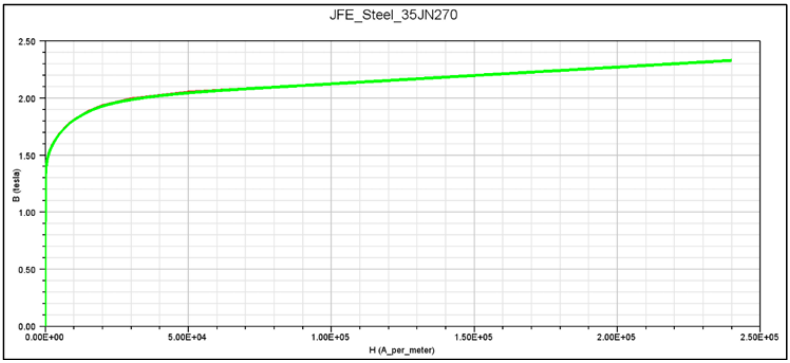

The core material in PMSM demonstrates effective magnetic performance without reaching magnetic saturation in applications requiring high efficiency. The JFE 35JN270 core material contributes to the motor's efficiency through its saturation characteristics and low core loss.

Figure 4 B–H Curve of 35JN270

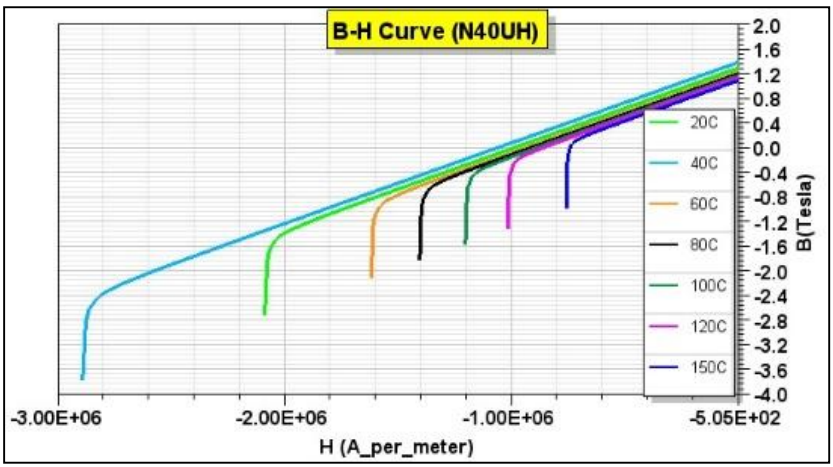

Due to the high power density, N40UH grade neodymium magnet material has been preferred in the PMSM design within the rotor. The B–H characteristics of the magnet and core materials are presented in Figure 4.

Table 2 Final Design Parameters of the Model

	Parameter	Value	Unit
Motor Specifications	Number of Poles, *p*	10	-
	Motor Output Power, *P*	1.4	kW
	Frequency, *f*	91.67	Hz
	Voltage, V	48	V
Motor Specifications	Rated Speed, ω_m	1100	rpm
	Rated Current, *I*	19.7	A
	Rated Torque	12.15	Nm
	Motor Stack Length, L_p	30.49	mm
	Number of Slots, N_s	39	-
Rotor	Rotor Outer Diameter, *Dro*	111.19	mm
	Rotor Inner Diameter, *Dri*	75.02	mm
	Air-Gap Length, g	1	-
Magnet	Magnet Thickness, *hm*	2.92	mm
	Magnet Length, *lm*	27.74	mm
	Type of Magnet	N40UH	-
	Relative Permeability of Magnet, μr	1.03	-
Winding	Connection Type	Star	-
	Winding Type	Distributed	-
	Number of Winding Layers	2	-
	Wire Diameter, *Dtel*	1.94	mm
	Number of Turns per Stator Phase, *Nt*	8	-
	Number of Parallel Wires, *ntel*	3	-
Stator	Number of Slots per Pole per Phase, *q*	1.3	-
	Stator Inner Diameter, *Dsi*	112.2	mm
	Stator Outer Diameter, *Dso*	191	mm
	Lamination Thickness	0.35	mm
	Stacking Factor, *kyf*	0.95	-
	Winding Factor, *ksf*	0.954	-
	Tooth Tip Thickness, *hs0*	1.1	mm
	Slot Tooth Tip Radius, *hs1*	1.21	mm
	Slot Height, *hs2*	26.7	mm
	Oluk açıklığı, *Bs0*	2	mm
	Stator Tooth Width, *wst*	5.9	mm

The general geometric dimensions of the designed motor, the core material, the materials used for the magnet construction, and the details of the stator winding connections are presented in Table 2.

2D Magnetic and Performance Analysis Using Finite Element Analysis

FEA is a numerical method used to solve complex electromagnetic field problems and circuit parameters. The primary purpose of employing FEA in analyzing electric motors is to evaluate magnetic saturation levels in various regions, such as the stator and rotor cores, teeth, and slots, and to verify the accuracy of the motor design model.

Before performing the motor analysis, the model is divided into small mesh elements, a process known as meshing. The key consideration in this step is to refine the model into smaller, more precise elements to improve the accuracy of the analysis results.

Figure 5 Motor Modelling Process

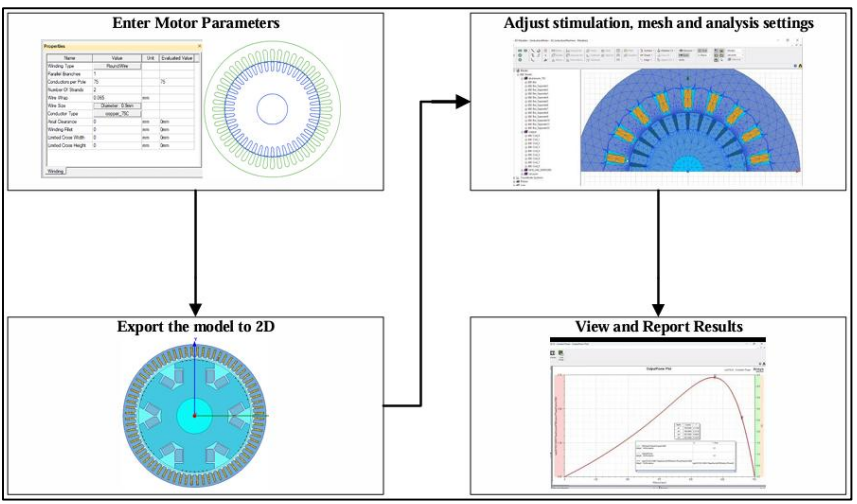

Electromagnetic problems in electrical machines are typically solved in either two or three dimensions, depending on the

nature of the problem. Two-dimensional models generally represent radial-flux PMSMs, and under typical conditions, simulations can be completed within a few minutes. To date, numerous two-dimensional analytical methods with varying levels of accuracy have been proposed and integrated into motor design and performance analysis processes.

In this study, ANSYS Maxwell software was utilized for the motor design and electromagnetic analysis processes. Initially, the basic parameters of the motor were defined through the RMxprt interface, and then the model was transferred to the 2D analysis environment. After the model transfer, a meshing process was applied to the geometry, enabling detailed electromagnetic analyses. During this process, the model was divided into small mesh elements and solved, thereby increasing the accuracy of the analysis results. Once the excitation conditions, mesh density, and analysis settings were finalized, the results were visualized and reported. All these steps were carried out in a systematic workflow to ensure a reliable evaluation of the motor's electromagnetic performance.

Figure 6 presents the results of the magnetic flux density distribution obtained after the Multi-Objective Genetic Algorithm (MOGA) optimization. In the two-dimensional finite element analysis, at a simulation time of 20.52478 ms, the motor speed was 1100 rpm, and the rotor position was determined to be 146.078946°. According to the analysis results obtained at this time step, the average flux density in the stator was 1.608 T, the flux density in the stator teeth was 1.629 T, and 1.9 T at the tooth tips. The flux density in the magnet region was measured as 0.931 T, while it was 1.37 T in the stator yoke and between 0.6 and 0.8 T in the rotor region. Additionally, the flux density between the magnets was determined to be 2.2 T and 2.157 T at the magnet edges.

Figure 6 Magnetic Flux Density Distribution of the Motor After Optimization

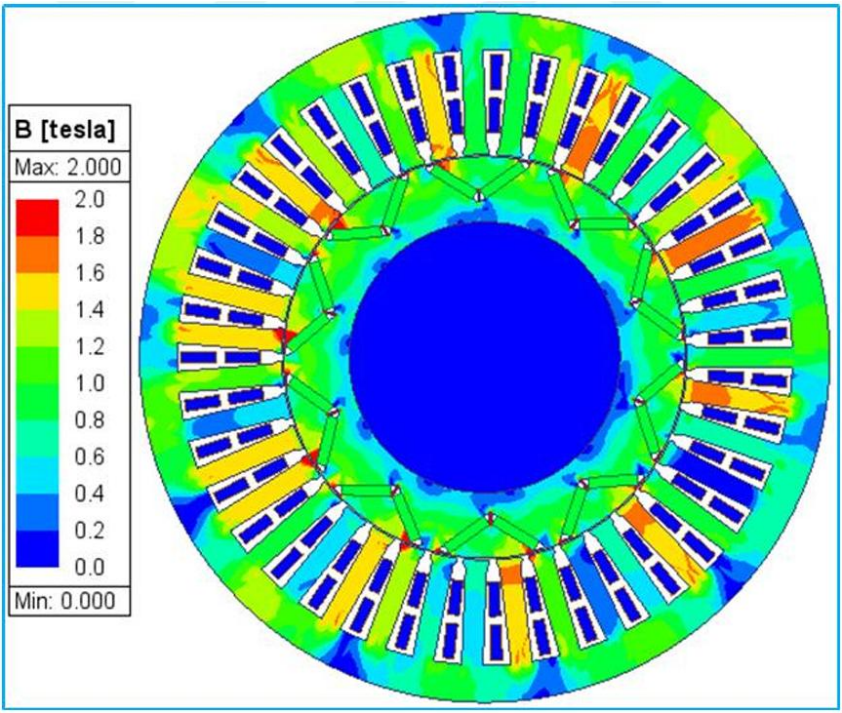

It was observed that the flux densities in the stator teeth remained below the magnetic saturation level of the silicon steel sheets used. Localized high flux densities were observed at the tooth tips, especially at corner transitions; however, these values were found to be insignificant (Soyaslan, 2020).

The magnetic flux paths of the 39-slot, 10-pole model obtained after MOGA optimization are examined in Figure 7. Post-optimization analysis revealed that the maximum magnetic vector potential in the magnets was 0.016 Wb/m.

Figure 7 Magnetic Vector Potential Distribution of the Motor After Optimization

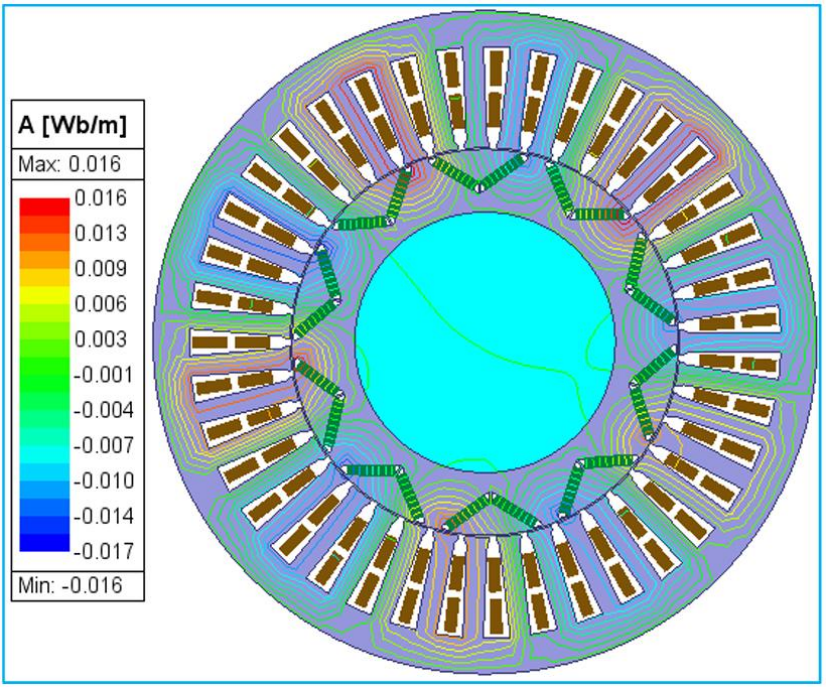

Figure 8 shows the average magnetic flux density distribution in the air gap of the motor under full-load conditions. The figure depicts the magnetic flux distribution resulting from the interaction between the rotor and stator. Based on the obtained data, the magnetic flux density in the air gap varies between approximately 0.25 T and 1.8 T, with an average value of 0.7901 T. This distribution indicates that the air gap flux density of the motor using Nd-based permanent magnets falls within the typical range of 0.7 T to 1.0 T. The average value obtained within this range indicates that the motor's magnet configuration and electromagnetic circuit design have been properly optimized.

Figure 8 Average Magnetic Flux Density Distribution in the Air Gap Under Full Load

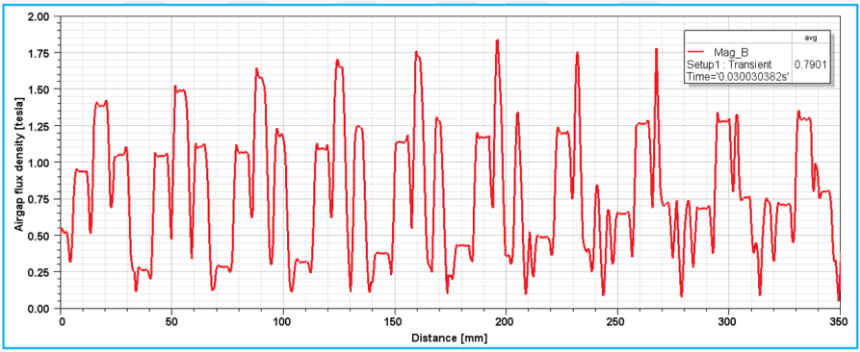

Figure 9 shows the change in stator currents over time. The phase current waveforms obtained after MOGA optimization show significant phase shift and amplitude imbalance between phases. The current waveforms exhibit sharp transitions resembling square waves and amplitude irregularities.

Figure 9 Variation of Stator Current Over Time

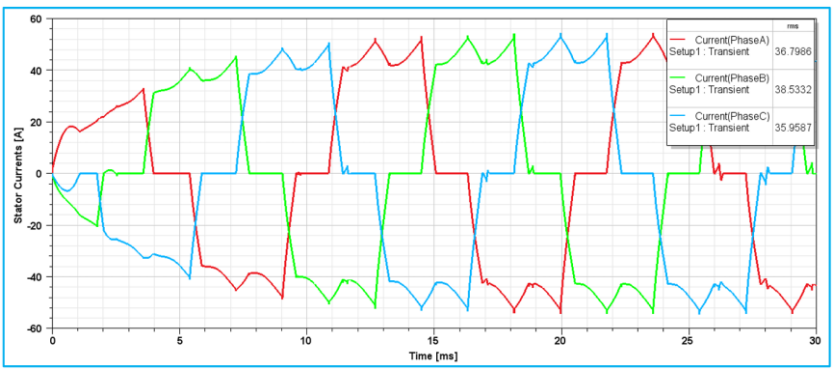

The calculated RMS current values for each phase were determined as 36.79 A for Phase A, 38.53 A for Phase B, and 35.95 A for Phase C. This graph indicates that sudden changes and fluctuations occur in the phase currents during the system's transient operating conditions. These fluctuations are attributed to sudden

variations in load conditions or the dynamic response characteristics of the system.

Figure 10 Torque–Time Graph

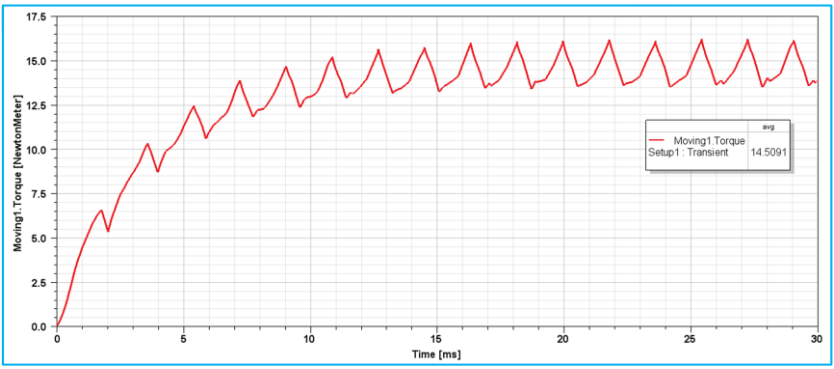

Figure 10 presents the torque–time graph obtained from the FEA. In the design optimized using the MOGA, the torque exhibits an increase and then stabilizes through periodic oscillations after approximately 5 ms. The smaller amplitude of these oscillations indicates that the motor shows a more stable performance. The average torque value was calculated as 14.5091 Nm.

Conclusion

In this study, the electromagnetic performance of the PMSM design developed for EV applications was comprehensively evaluated through analytical calculations and FEA. The developed model was optimized to achieve an output power of 1.4 kW, a nominal torque of 12.15 Nm, and an efficiency target of 94%. By employing NdFeB-based N40UH magnets and low-loss JFE Steel 35JN270 silicon steel sheets, high energy density and low core losses were achieved.

In the two-dimensional electromagnetic analyses conducted using ANSYS Maxwell, the average flux density on the stator teeth was measured as 1.629 T, 1.37 T in the yoke region, and between 0.6–0.8 T in the rotor core. The average torque value was obtained

as 14.5091 Nm, while the average air-gap flux density between the rotor and stator was determined to be 0.7901 T. In the three-phase system current analysis, the RMS current per phase was found to be approximately within the range of 36–38 A.

The PMSM design demonstrated excellent electromagnetic performance characterized by high torque density, well-distributed magnetic flux, and low losses. It was concluded that the proposed design can provide stable and efficient driving performance under varying load and speed conditions typically encountered in EV applications.

References

Helmers, E., & Marx, P. (2012). Electric cars: technical characteristics and environmental impacts. *Environmental Sciences Europe*, *24*(1), 14. https://doi.org/10.1186/2190-4715-24-14

Alanazi, F. (2023). Electric vehicles: benefits, challenges, and potential solutions for widespread adaptation. *Applied sciences*, *13*(10), 6016. https://doi.org/10.3390/app13106016

Gobbi, M., Sattar, A., Palazzetti, R., & Mastinu, G. (2024). Traction motors for electric vehicles: Maximization of mechanical efficiency–A review. *Applied Energy*, *357*, 122496. https://doi.org/10.1016/j.apenergy.2023.122496

Un-Noor, F., Padmanaban, S., Mihet-Popa, L., Mollah, M. N., & Hossain, E. (2017). A comprehensive study of key electric vehicle (EV) components, technologies, challenges, impacts, and future direction of development. *Energies*, *10*(8), 1217. https://doi.org/10.3390/en10081217

Zeraoulia, M., Benbouzid, M. E. H., & Diallo, D. (2006). Electric motor drive selection issues for HEV propulsion systems: A comparative study. *IEEE Transactions on Vehicular Technology*, *55*(6), 1756-1764. https://doi.org/10.1109/vppc.2005.1554571

Rimpas, D., Kaminaris, S. D., Piromalis, D. D., Vokas, G., Arvanitis, K. G., & Karavas, C. S. (2023). Comparative review of motor technologies for electric vehicles powered by a hybrid energy storage system based on multi-criteria analysis. *Energies*, *16*(6), 2555. https://doi.org/10.3390/en16062555

Sieklucki, G. (2021). *Optimization of Powertrain in EV. Energies 2021, 14, 725*. https://doi.org/10.3390/en14030725

Quoc, V. D., & Huu, H. B. (2024). Modeling of Surface-mounted Permanent Magnet Synchronous Motors with Inner and Outer Rotor

Types. *International Journal of Engineering, Transactions C: Aspects*. https://doi.org/10.5829/ije.2024.37.12c.11

Du, G., Li, N., Zhou, Q., Gao, W., Wang, L., & Pu, T. (2022). Multi-physics comparison of surface-mounted and interior permanent magnet synchronous motor for high-speed applications. *Machines*, *10*(8), 700. https://doi.org/10.3390/machines10080700

Dwivedi, S. K., Laursen, M., & Hansen, S. (2010, July). Voltage vector based control for PMSM in industry applications. In 2010 IEEE International Symposium on Industrial Electronics (pp. 3845-3850). IEEE. https://doi.org/10.1109/isie.2010.5637742

Murali, N., & Ushakumari, S. (2020, November). Performance comparison between different rotor configurations of PMSM for EV application. In *2020 IEEE REGION 10 CONFERENCE (TENCON)* (pp. 1334-1339). IEEE. https://doi.org/10.1109/tencon50793.2020.9293844

Hwang, M. H., Han, J. H., Kim, D. H., & Cha, H. R. (2018). Design and analysis of rotor shapes for IPM motors in EV power traction platforms. *Energies*, *11*(10), 2601. https://doi.org/10.3390/en11102601

Ying, H., Huang, S., & Xu, D. (2017). A high-speed low-noise rotor topology for EV/HEV PMSM. *CES Transactions on Electrical Machines and Systems*, *1*(4), 354-359. https://doi.org/10.23919/tems.2017.8241356

Balta, B. A., Ayçiçek, E., Aydeniz, M. G., & Dedecan, H. Performance Comparison of Permanent Magnet Synchronous Motor with Different Magnet Configuration Used in Electric Vehicle. *Balkan Journal of Electrical and Computer Engineering*, *12*(4), 364-368. https://doi.org/10.17694/bajece.1559038

Liu, X., Chen, H., Zhao, J., & Belahcen, A. (2016). Research on the performances and parameters of interior PMSM used for electric

vehicles. *IEEE Transactions on Industrial Electronics*, *63*(6), 3533-3545. https://doi.org/10.1109/tie.2016.2524415

Yan, J., Yang, K., Zhang, S., Feng, Y., Chen, Y., & Yang, H. (2017). Comparative investigation of inset-type and V-type IPMSM for a light electric vehicle. *International Journal of Applied Electromagnetics and Mechanics*, *54*(4), 515-524. https://doi.org/10.3233/jae-170001

Genç, K., Todd, I., & Mumtaz, K. (2025). Influence of heat treatment on microstructure and magnetic properties of laser powder bed fusion generated NdFeB magnets. *Progress in Additive Manufacturing*, 1-17. https://doi.org/10.1007/s40964-024-00941-1

Hirosawa, S., Nishino, M., & Miyashita, S. (2017). Perspectives for high-performance permanent magnets: applications, coercivity, and new materials. *Advances in Natural Sciences: Nanoscience and Nanotechnology*, *8*(1), 013002. https://doi.org/10.1088/2043-6254/aa597c

Vlachou, V. I., Sakkas, G. K., Xintaropoulos, F. P., Pechlivanidou, M. S. C., Kefalas, T. D., Tsili, M. A., & Kladas, A. G. (2024). Overview on permanent magnet motor trends and developments. *Energies*, *17*(2), 538. https://doi.org/10.20944/preprints202312.1678.v1

Desai, R., Holmukhe, R., Chopade, D., Ambekar, R., Pangare, N., Kadam, R., Chaudhari, P., Pare, M., & Mehta, H. (2023). *A FEA Study of the Optimal Magnetic Material for IPMSM Design in EV Applications*. *Tuijin Jishu / Journal of Propulsion Technology, 44*(6). https://doi.org/10.52783/tjjpt.v44.i6.3142

Gürdal, O. (2001). *Elektrik makinalarının tasarımı*. Atlas Yayın Dağıtım.

Izanlo, A., Gholamian, S. A., & Abdollahi, S. E. (2020). Optimal design of a permanent magnet synchronous motor for high efficiency and low cogging torque. *International Journal on Electrical*

Engineering and Informatics, *12*(2), 173-186. https://doi.org/10.15676/ijeei.2020.12.2.1

Boldea, I., & Tutelea, L. N. (2009). *Electric machines: steady state, transients, and design with MATLAB*. CRC press.

Boldea, I., & Nasar, S. A. (2010). The induction machines design handbook. *(No Title)*.

Pyrhonen, J., Jokinen, T., & Hrabovcova, V. (2013). *Design of rotating electrical machines*. John Wiley & Sons.

Lipo, T. A. (2017). *Introduction to AC machine design*. John Wiley & Sons.

Gieras, J. F. (2009). *Permanent magnet motor technology: design and applications*. CRC press.

Kartal, E. T., & Arabul, F. K. (2022). A comparison between IM and IPMSM with the same stator core for EV and performance analysis of IPMSM. *Avrupa Bilim ve Teknoloji Dergisi*, (38), 165-172. https://doi.org/10.31590/ejosat.1108129

Soleimani, K. M., & Gholamian, S. A. (2013). Optimum design of a three-phase permanent magnet synchronous motor for industrial applications.

Meier, F. (2008). *Permanent-magnet synchronous machines with non-overlapping concentrated windings for low-speed direct-drive applications* (Doctoral dissertation, KTH).

Liu, H. (2015). Design of high-efficiency rare-earth permanent magnet synchronous motor and drive system.

Ammar, A. O. M. O. (2023). Design and performance evaluation of V-shape PMSM in automotive oil pump systems.

Yulianto, K., Yusivar, F., & Sudiarto, B. (2021, June). The Influence of Magnet Number and Dimension on Torque Characteristics in the

Interior Permanent Magnet Synchronous Motor (PMSM). In *IOP Conference Series: Materials Science and Engineering* (Vol. 1158, No. 1, p. 012006). IOP Publishing. https://doi.org/10.1088/1757-899x/1158/1/012006

Cetinceviz, Y. (2025). Optimal Design, Electromagnetic–Thermal Analysis and Application of In-Wheel Permanent Magnet BLDC Motor for E-Mobility. *Applied Sciences*, *15*(6), 3258. https://doi.org/10.3390/app15063258

Samanta, P., Mitikiri, S. B., Sahay, P. K., & Srinivas, V. L. (2025). A comparative review of radial and axial Flux PMSMs: Innovations in topology, design, and control. *Franklin Open*, 100341. https://doi.org/10.1016/j.fraope.2025.100341

Nye, M., D'Arpino, M., & Di Noia, L. P. (2025). Accuracy of Core Losses Estimation in PMSM: A Comparison of Empirical and Numerical Approximation Models. *Energies*, *18*(17), 4494. https://doi.org/10.3390/en18174494

El Hadraoui, H., Zegrari, M., Chebak, A., Laayati, O., & Guennouni, N. (2022). A multi-criteria analysis and trends of electric motors for electric vehicles. *World Electric Vehicle Journal*, *13*(4), 65. https://doi.org/10.3390/wevj13040065

Zadorozhniuk, D., Lindh, P., Allahyari, A., Petrov, I., & Pyrhönen, J. (2024, September). Surface vs. Embedded Magnets in Permanent Magnet Outer Rotor Synchronous Motors. In the *2024 International Conference on Electrical Machines (ICEM)* (pp. 1-7). IEEE. https://doi.org/10.1109/icem60801.2024.10700150

Dong, J., Huang, Y., Jin, L., & Lin, H. (2016). Comparative study of surface-mounted and interior permanent-magnet motors for high-speed applications. *IEEE Transactions on Applied Superconductivity*, *26*(4), 1-4. https://doi.org/10.1109/tasc.2016.2514342

Xing, J., Wang, F., Wang, T., & Zhang, Y. (2010). Study on anti-demagnetization of magnet for high speed permanent magnet

machine. *IEEE Transactions on Applied Superconductivity*, *20*(3), 856-860. https://doi.org/10.1109/tasc.2009.2039121

Kilmartin, J. (2016). *Effects of the Pole-Slot Combination on a Surface Permanent Magnet Generator for Wind Applications* (Doctoral dissertation, Flinders University, School of Computer Science, Engineering and Mathematics).

Lin, H. N., Seangwong, P., Fernando, N., Siritaratiwat, A., & Khunkitti, P. (2025). Torque Capability Enhancement of Commercial Interior Permanent Magnet Motors using T-Shaped Notched and Merged Barrier Rotor Topology. *Results in Engineering*, 105108. https://doi.org/10.1016/j.rineng.2025.105108

Jeong, H., & Baek, J. (2020). Design of a three-phase V-shaped interior permanent magnet synchronous motor for an air conditioning compressor of an electric vehicle. *Applied Sciences*, *10*(24), 8785. https://doi.org/10.3390/app10248785

Zhou, J., Cheng, M., Yu, W., & Hua, W. (2023). Analysis of torque ripple in V-shape interior permanent magnet machine based on general airgap field modulation theory. *Energies*, *16*(12), 4586. https://doi.org/10.3390/en16124586

Hahlbeck, S., & Gerling, D. (2008, September). Design Considerations for Rotors with Embedded V-Shaped Permanent Magnets. In *2008 18th International Conference on Electrical Machines* (pp. 1-4). IEEE. https://doi.org/10.1109/icelmach.2008.4800192

Soyaslan, M. (2020). *Asansör tahrik sistemleri için dıştan rotorlu sürekli mıknatıslı bir senkron motor tasarımı* (Doctoral dissertation, Doktora Tezi, Sakarya Uygulamalı Bilimler Üniversitesi).

CHAPTER 9

ARTIFICIAL INTELLIGENCE APPLIED TO ELECTRIC VEHICLE BATTERY TECHNOLOGY

MUHAMMED TAN[1]

Introduction

The Software-Defined or AI-Defined Vehicle presents a new ecosystem for Battery Intelligence. The electric vehicle (EV) represents not one, but two, technological revolutions running in parallel: the profound shift in energy storage and propulsion (electrification) and the wholesale reinvention of a vehicle's intelligence and architecture (digitalization) (Cavus, Dissanayake, & Bell, 2025; H. Lin, Yan, & Cheng, 2023). The catalyst that fuses these two streams by transforming a piece of hardware into a dynamic, intelligent, and interconnected platform is artificial intelligence (AI). This convergence, underpinned by machine learning, deep learning, and reinforcement learning, is creating a fundamental paradigm shift from a mechanically-centric design to that of a Software-Defined Vehicle (SDV) (W. A. Ali, Fanti, Roccotelli, & Ranieri, 2023; Cavus et al., 2025; Naseri et al., 2023).

[1] Assist. Prof., Kastamonu University, Faculty of Engineering and Architecture, Dept. of Electrical and Electronics Engineering, Orcid: 0000-0003-0825-1325

In this new paradigm, the vehicle's functions are progressively decoupled from their underlying physical hardware, enabling intelligent, adaptive, and evolutionary vehicle systems. AI-driven data-centric architectures allow for real-time analytics, continuous feature deployment, and evolutionary capabilities, often delivered via over-the-air (OTA) updates (Babaei, Riahinia, Ebadati E, & Azimi, 2025; Che, Wang, Yao, & Gu, 2025; Chougule, Chaudhari, Ghorpade, & Zennaro, 2024). This transition is not merely semantic; it provides the essential tools to tackle the most persistent challenges that have historically hindered EV adoption: range anxiety, battery degradation, and grid instability (Ahmed, Zheng, Amine, Fathiannasab, & Chen, 2021; Arévalo, Ochoa-Correa, & Villa-Ávila, 2024; Sumanasena et al., 2023; Venkatesh Kumar et al., 2024).

The AI impact is highly perceptible and quantifiable. Across the literature, the application of AI-driven strategies is already linked to significant performance and lifecycle improvements, including approximately 20% increases in battery lifespan (Afzal et al., 2023; Sudhapriya & Jaisiva, 2025), significant improvements in state-of-charge (SOC) estimation accuracy (less than 1% errors) (Arévalo et al., 2024; Zafar et al., 2023), and reductions in unplanned downtime owing to early fault detection and proactive interventions (Bahheti et al., 2024; Cavus et al., 2025). Furthermore, AI-powered energy management and smart charging optimization have shown that it is capable of 10-30% gains in energy efficiency and 13-70% reductions in charging costs depending on the system and scenario, with the highest savings reported based on dynamic pricing and optimal scheduling (Arévalo et al., 2024; S. Li et al., 2022; Mishra, Choubey, Devarasetty, Sharma, & Misra, 2024; Shern et al., 2024; Udeogu & Lim, 2022; Zhong, Liu, Liu, Fan, & Tang, 2025). This book chapter explores the application of AI in the heart of the modern EV: the battery.

The Intelligent BMS: From Static Rules to Digital Twins

As the primary enabler of the Software-Defined Vehicle ecosystem described previously, the Battery Management System (BMS) acts as the vehicle's electronic brain responsible for the safety, longevity, and performance of its most expensive and complex component. This task is extraordinarily difficult due to the complex, non-linear, and time-varying electrochemical physics of lithium-ion batteries. The AI-driven solutions for BMS are not just models; they are often deployed within a Digital Twin framework, which serves as the core architecture for unifying sensor data, AI prognostics, and real-time control (Wu, Widanage, Yang, & Liu, 2020).

This integration is illustrated in Figure 1, which depicts the Digital Twin framework where real-time sensor data informs a virtual replica for continuous optimization.

Figure 1. Digital Twin framework for Battery Management Systems

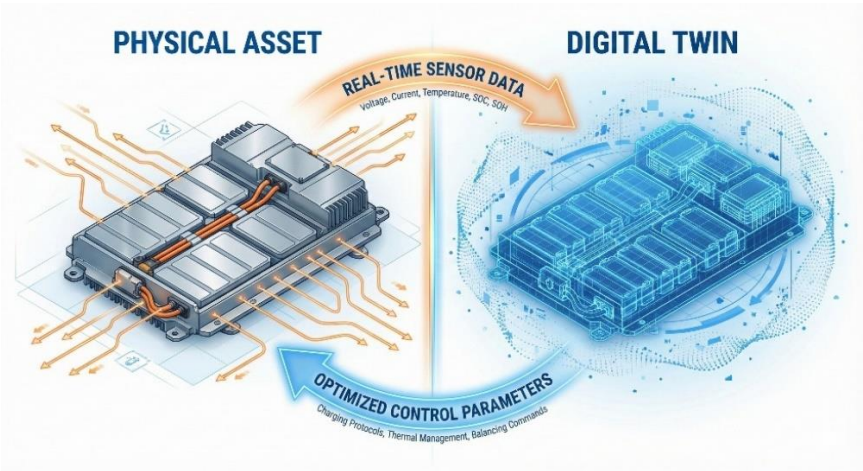

Source: Created with our descriptive prompt by a generative AI (GenAI) tool.

Beyond Rule-Based Limitations

Traditional BMS architectures, which have dominated the industry, are fundamentally static. They rely on fixed algorithms,

such as Coulomb counting for state-of-charge (SOC) estimation or predefined lookup tables for operational limits (Krishna et al., 2024; Sancarlos et al., 2021; Yilmaz, Cinar, & Yazici, 2025). These methods lack robustness as they struggle to adapt to the realities of battery aging, environmental changes, and the stochastic nature of real-world driving scenarios (Cavus et al., 2025; Ghalkhani & Habibi, 2023; Lipu et al., 2024). Such conventional methods struggle because they attempt to apply linear rules to the complex, non-linear electrochemical physics of a lithium-ion battery. Coulomb counting, for instance, is notoriously susceptible to sensor drift, accumulating significant errors over time, while lookup tables simply cannot capture the dynamic behavior of a cell under load (Krishna et al., 2024; Sancarlos et al., 2021).

Figure 2. Synthetic SOC Estimation Error: Rule-Based Drift vs. Deep Learning Precision

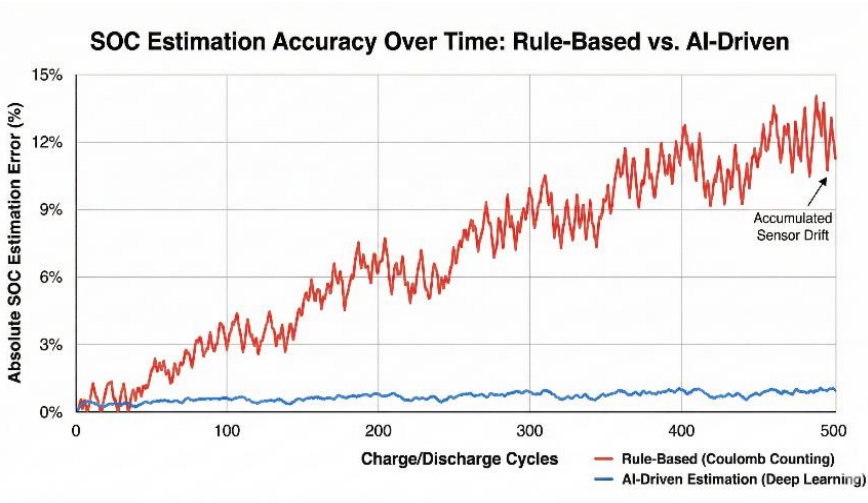

Source: Generated with our prompt for a representative scenario by a GenAI tool.

The qualitative magnitude of this limitation is visualized in Figure 2, which hypothetically contrasts the accumulated error drift of a traditional rule-based approach against the sustained stability of

an AI-driven estimation model over 500 cycles using a characteristic synthetic data for demonstration purposes only.

AI transforms the BMS from this static, rule-based guardian into a predictive, self-learning platform. By leveraging machine learning (ML), deep learning (DL), and reinforcement learning (RL), an intelligent BMS can dynamically adjust its control strategies in real-time, adapting to battery degradation, unique usage patterns, and external conditions to improve safety, reliability, and lifespan (Cavus et al., 2025; Ghalkhani & Habibi, 2023; Wu et al., 2020).

High-Fidelity State Estimation: The Core of Intelligent BMS

The most critical task of any BMS is to answer three fundamental questions: How much energy is left (State of Charge, SOC)? What is the battery's current condition (State of Health, SOH)? And how long will it last (Remaining Useful Life, RUL)? AI-driven estimation provides a profound leap in the accuracy of these vital metrics.

Deep learning models, particularly Long Short-Term Memory (LSTM) networks, hybrid Convolutional Neural Networks (CNNs), and Gaussian Process Regression (GPR), have proven exceptionally adept at this task (M. K. Khan et al., 2024; Sultan, Eladl, Hassan, & Gamel, 2025; Tripp-Barba, Aguilar-Calderón, Urquiza-Aguiar, Zaldívar-Colado, & Ramírez-Noriega, 2025). Unlike their conventional counterparts, these models are designed to capture the complex, non-linear, and time-dependent relationships within battery data (voltage, current, temperature) that are opaque to traditional physics-based models (M. K. Khan et al., 2024; S. L. Lin, 2024; Obuli Pranav et al., 2024).

The performance gains are definitive. Multiple studies focusing on LSTM-based and hybrid models report low estimation errors for SOC, SOH, and RUL often achieving percentage errors as low as 1% (Cheng, Wang, & He, 2021; Fasahat & Manthouri, 2020;

U. Khan, Kirmani, Rafat, Rehman, & Alam, 2024; P. Li et al., 2020; Zhao, Liu, Zhou, Ming, & Wu, 2025). This high-fidelity estimation is often operationalized within a Digital Twin framework. This approach uses AI models (such as TCN-LSTM) to power a real-time, adaptive virtual replica of the physical battery, enabling continuous model updates and system-wide optimization with reported RMSEs as low as 0.8–1.1% (Zhao et al., 2025). This leap in estimation accuracy is not merely a speculative exercise; it translates directly into concrete economic and operational value:

- *Higher Vehicle Residual Value:* Accurate, verifiable SOH and RUL data effectively create a de facto "battery health certificate." This reduces the uncertainty and risk for a second-hand EV buyer, directly supporting higher resale value (X. Chen et al., 2023; Sylvestrin et al., 2025).
- *Enhanced Second-Life Viability:* The trillion-dollar market for second-life batteries (e.g., for stationary grid storage) depends entirely on the ability to reliably assess the SOH and RUL of retired EV packs. Precise ML-based predictions are the key enabler for this circular economy, maximizing the battery's lifecycle value (X. Chen et al., 2023; Sultan et al., 2025; Sylvestrin et al., 2025).
- *New Business Models:* High-fidelity, real-time state estimation is the technological backbone for new mobility concepts like Battery-as-a-Service (BaaS). Such predictive models could make dynamic leasing, battery swapping, and pay-per-use schemes for EVs technologically and financially viable (Cavus et al., 2025; Sylvestrin et al., 2025; Zhao et al., 2025).

Predictive Thermal Management and Safety

Beyond estimation, the primary directive of a BMS is to ensure safety. AI is shifting this function from reactive damage

control to proactive, predictive thermal management. The goal is to prevent thermal runaway (TR) before it occurs.

Deep learning models, including hybrid LSTM-CNNs and Graph Neural Networks (GNNs), are being used to create spatiotemporal forecasts of a battery's temperature profile (Das Goswami, Abdisobbouhi, et al., 2024; Das Goswami, Mastrogiorgio, et al., 2024). By analyzing real-time voltage, current, and temperature data, these models can identify abnormal heat generation and predict the onset of thermal runaway with remarkable foresight, in some cases providing early warnings up to 27 minutes before a critical TR event (D. Li et al., 2022; Ma, Huo, Wang, & Zhang, 2023). Figure 3 theoretically illustrates this predictive warning scenario with typical battery operation, decomposition and breakdown temperatures.

Figure 3. AI Early Warning vs. Physical Breakdown Stages

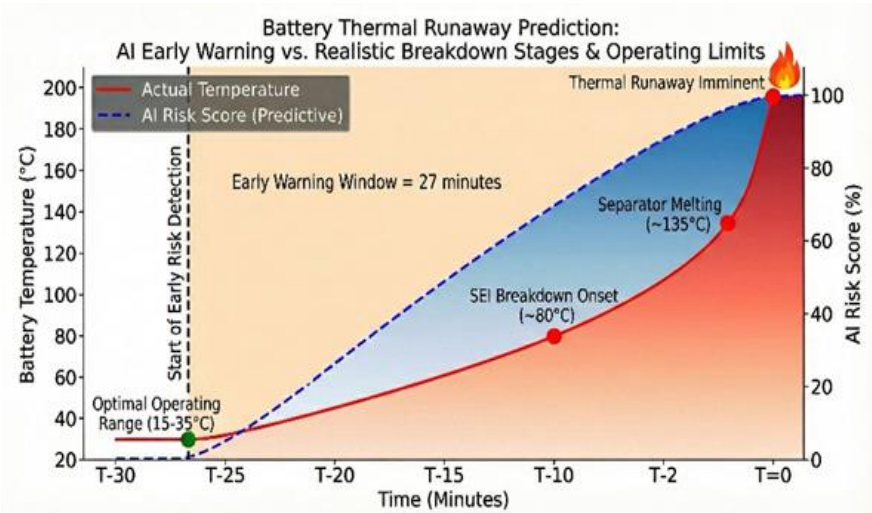

Source: Generated with an iterative GenAI prompt descriptive of the TR process.

A synthetic representation of this capability (see Fig. 3) exemplifies how a prediction or forecast-based AI risk score can detect anomalies significantly earlier than traditional physical

thresholds such as the Solid Electrolyte Interphase (SEI) layer decomposition or the separator melting temperatures offering a crucial time window for proactive intervention. This predictive window is transformative, enabling proactive interventions such as targeted cooling, isolating faulty cells, or optimizing charging protocols that have been shown to reduce TR occurrence and severity by as much as 78% and 93%, respectively (Hemakumar et al., 2024).

Other ML models, such as Random Forests, are used to pinpoint the exact location of faulty cells from optimized sensor data, while Generative Adversarial Networks (GANs) can detect subtle charging anomalies that signal a cell at risk (Daniels, Kumar, & Prabhakar, 2025; H. Li et al., 2024; Tran et al., 2022).

Adaptive Charging and Lifespan Extension

Finally, the intelligent BMS optimizes how the battery is charged, moving from a static "dumb" charger to a dynamic, personalized strategy. Reinforcement Learning (RL) is the primary tool for this application (Yalçın & Herdem, 2024).

RL models excel at developing adaptive, real-time charging policies that learn from users' usage patterns, the battery's current SOH, and dynamic grid pricing (Cavus et al., 2025; Gu, Qian, & Yang, 2025; Sultanuddin et al., 2023). The result is a personalized strategy that navigates the complex trade-off between user convenience, charging speed, and battery health.

The consensus from recent studies shows this approach yields a dual benefit. First, it directly minimizes battery degradation by avoiding harmful charging patterns, leading to measurable reductions in capacity fade (Hu, Yuan, Su, & Ou, 2023; Liu et al., 2025; Wang, Wang, & Fu, 2025; Yalçın & Herdem, 2024). Second, it optimizes the economic and environmental impact of charging. By intelligently shifting charging to off-peak or renewable-rich periods,

RL-based strategies would reduce user costs by up to 70% while simultaneously flattening grid load, a critical function for grid stability (Lee, Lee, & Kim, 2020; S. Li et al., 2022; Sultanuddin et al., 2023; Tuchnitz, Ebell, Schlund, & Pruckner, 2021).

Future Frontiers: Generative AI, Privacy, and Trust

While the intelligent BMS architectures described in the previous section demonstrate the immense potential of AI to optimize performance and safety, their widespread deployment within the Software-Defined Vehicle ecosystem faces grand challenges that define the future research agenda (Ghalkhani & Habibi, 2023).

The Data Challenge and Generative AI: A critical hurdle is the scarcity of real-world fault data. Generative AI (GANs) has revolutionized fault diagnosis for motors and gearboxes (M. Chen, Shao, Dou, Li, & Liu, 2023; Lang et al., 2022), and holds immense promise for battery systems as well. These models can create high-fidelity, synthetic fault data to train robust diagnostic models without waiting for catastrophic failures to occur in the field (Shaker, Pietro Rosati Papini, Saveriano, & Liang, 2024; Zhang et al., 2025).

Privacy and Federated Learning: As BMSs become cloud-connected within the Internet of Electric Vehicles (IoEV), data privacy is paramount. Federated Learning (FL) is emerging as the standard for fleet-wide intelligence. FL allows vehicles to collaboratively train improved SOC/SOH models without sharing sensitive raw data, ensuring privacy while leveraging the collective wisdom of the fleet (Yan et al., 2024; Yilmaz et al., 2025). This decentralized architecture is visualized in Figure 4, which demonstrates how individual vehicles compute local model updates (gradients) and share only these mathematical parameters with the central cloud, keeping the sensitive raw user data securely locked within the vehicle.

Figure 4. Privacy-Preserving Federated Learning Architecture

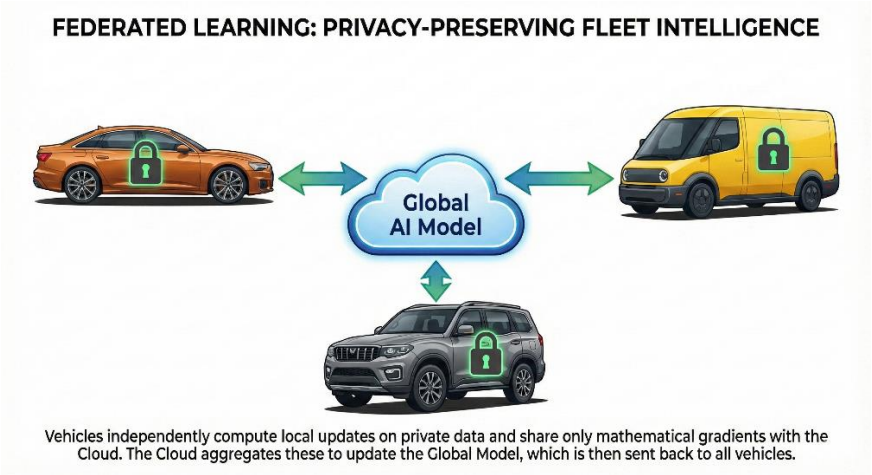

Source: Generated with a GenAI tool to illustrate the Federated Learning concept.

Trust and XAI: While the predictive safety measures discussed in the predictive thermal safety section offer immense value, the 'black box' nature of deep learning remains a barrier to safety certification. The integration of Explainable AI (XAI) is essential to provide engineers and regulators with interpretable insights into why a BMS makes a specific prediction, bridging the gap between high-accuracy AI and verifiable safety (S. Ali et al., 2023; Nkechinyere Njoku, Ifeanyi Nwakanma, & Kim, 2024).

Conclusion

The battery is the heart of the electric vehicle, and AI has become its pacemaker. By moving from static rules to predictive intelligence, AI-driven BMSs are extending lifespans, enhancing safety, and unlocking new economic value. As the industry moves from Software Defined Vehicle toward the AI-Defined Vehicle, the intelligent battery stands as the most mature and impactful application of this technological revolution.

The key takeaways of this book chapter on AI applied to Electric Vehicle Battery Technology are as follows:

- *Paradigm Shift:* The transition from Software-Defined Vehicles (SDVs) to AI-Defined Vehicles has potential to transform the battery from a simple stationary chemical component into an intelligent, data-generating platform managed by AI.
- *Precision Estimation:* Deep Learning models (e.g., LSTMs) and Digital Twin frameworks have reduced State-of-Charge (SOC) and State-of-Health (SOH) estimation errors to nearly 1%, potentially paving the way to novel business models that can rely on such accurate forecasts.
- *Proactive Safety:* AI enables a shift from reactive protection to predictive safety, capable of forecasting thermal runaway events minutes before they occur by analyzing non-linear voltage and temperature anomalies.
- *Fleet Intelligence:* Federated Learning allows EV fleets to collaboratively train robust AI models without sharing sensitive user data, solving the dual challenge of data privacy and model scalability.

References

Afzal, M. Z., Aurangzeb, M., Iqbal, S., Pushkarna, M., Rehman, A. U., Kotb, H., … Bereznychenko, V. (2023). A novel electric vehicle battery management system using an artificial neural network-based adaptive droop control theory. International Journal of Energy Research, 2023, 1–15. https://doi.org/10.1155/2023/2581729

Ahmed, M., Zheng, Y., Amine, A., Fathiannasab, H., & Chen, Z. (2021). The role of artificial intelligence in the mass adoption of electric vehicles. Joule, 5(9), 2296–2322. https://doi.org/10.1016/j.joule.2021.07.012

Ali, S., Abuhmed, T., El-Sappagh, S., Muhammad, K., Alonso-Moral, J. M., Confalonieri, R., … Herrera, F. (2023). Explainable Artificial Intelligence (XAI): What we know and what is left to attain Trustworthy Artificial Intelligence. Information Fusion, 99, 101805. https://doi.org/10.1016/j.inffus.2023.101805

Ali, W. A., Fanti, M. P., Roccotelli, M., & Ranieri, L. (2023). A Review of Digital Twin Technology for Electric and Autonomous Vehicles. Applied Sciences (Switzerland), 13(10), 5871. https://doi.org/10.3390/app13105871

Arévalo, P., Ochoa-Correa, D., & Villa-Ávila, E. (2024). A Systematic Review on the Integration of Artificial Intelligence into Energy Management Systems for Electric Vehicles: Recent Advances and Future Perspectives. World Electric Vehicle Journal, 15(8), 364. https://doi.org/10.3390/wevj15080364

Babaei, P., Riahinia, N., Ebadati E, O. M., & Azimi, A. (2025). Towards a Data-Driven Digital Twin AI-Based Architecture for Self-Driving Vehicles. IET Intelligent Transport Systems, 19(1). https://doi.org/10.1049/itr2.70017

Bahheti, M., Shankarnarayan, V. K., Durairajan, S., Chandak, S., Gurunathan, T., & Chandrasekar, P. (2024). AI-Powered Predictive Maintenance for Electric Vehicle Fleets. 2024 Asian Conference on Intelligent Technologies (ACOIT), 1–6. IEEE. https://doi.org/10.1109/ACOIT62457.2024.10939072

Cavus, M., Dissanayake, D., & Bell, M. (2025). Next Generation of Electric Vehicles: AI-Driven Approaches for Predictive Maintenance and Battery Management. Energies, 18(5), 1041. https://doi.org/10.3390/en18051041

Che, H., Wang, S., Yao, L., & Gu, Y. (2025). A comprehensive perspective on electric vehicles as evolutionary robots. Frontiers in Robotics and AI, 12. https://doi.org/10.3389/frobt.2025.1499215

Chen, M., Shao, H., Dou, H., Li, W., & Liu, B. (2023). Data Augmentation and Intelligent Fault Diagnosis of Planetary Gearbox Using ILoFGAN under Extremely Limited Samples. IEEE Transactions on Reliability, 72(3), 1029–1037. https://doi.org/10.1109/TR.2022.3215243

Chen, X., Chen, Z., Zhang, M., Wang, Z., Liu, M., Fu, M., & Wang, P. (2023). A remaining useful life estimation method based on long short-term memory and federated learning for electric vehicles in smart cities. PeerJ Computer Science, 9, 1–26. https://doi.org/10.7717/peerj-cs.1652

Cheng, G., Wang, X., & He, Y. (2021). Remaining useful life and state of health prediction for lithium batteries based on empirical mode decomposition and a long and short memory neural network. Energy, 232, 121022. https://doi.org/10.1016/j.energy.2021.121022

Chougule, S. B., Chaudhari, B. S., Ghorpade, S. N., & Zennaro, M. (2024). Exploring Computing Paradigms for Electric Vehicles: From Cloud to Edge Intelligence, Challenges and Future Directions. World

Electric Vehicle Journal, 15(2), 39. https://doi.org/10.3390/wevj15020039

Daniels, R. K., Kumar, V., & Prabhakar, A. (2025). A comparative study of data-driven thermal fault prediction using machine learning algorithms in air-cooled cylindrical Li-ion battery modules. Renewable and Sustainable Energy Reviews, 207, 114925. https://doi.org/10.1016/j.rser.2024.114925

Das Goswami, B. R., Abdisobbouhi, Y., Du, H., Mashayek, F., Kingston, T. A., & Yurkiv, V. (2024). Advancing battery safety: Integrating multiphysics and machine learning for thermal runaway prediction in lithium-ion battery module. Journal of Power Sources, 614, 235015. https://doi.org/10.1016/j.jpowsour.2024.235015

Das Goswami, B. R., Mastrogiorgio, M., Ragone, M., Jabbari, V., Shahbazian-Yassar, R., Mashayek, F., & Yurkiv, V. (2024). A combined multiphysics modeling and deep learning framework to predict thermal runaway in cylindrical Li-ion batteries. Journal of Power Sources, 595, 234065. https://doi.org/10.1016/j.jpowsour.2024.234065

Fasahat, M., & Manthouri, M. (2020). State of charge estimation of lithium-ion batteries using hybrid autoencoder and Long Short Term Memory neural networks. Journal of Power Sources, 469, 228375. https://doi.org/10.1016/j.jpowsour.2020.228375

Ghalkhani, M., & Habibi, S. (2023). Review of the Li-Ion Battery, Thermal Management, and AI-Based Battery Management System for EV Application. Energies, 16(1), 185. https://doi.org/10.3390/en16010185

Gu, S., Qian, K., & Yang, Y. (2025). Optimization of Electric Vehicle Charging and Discharging Strategies Considering Battery Health State: A Safe Reinforcement Learning Approach. World Electric Vehicle Journal, 16(5), 286. https://doi.org/10.3390/wevj16050286

Hemakumar, V. S., Chakravarthy, V. J., Surendranath, S., Gundu, V., Ramkumar Prabhu, M., & Hari Chandra Prasad, S. (2024). A multi-scale modeling approach for predicting and mitigating thermal runaway in electric vehicle batteries. Thermal Science and Engineering Progress, 56, 103029. https://doi.org/10.1016/j.tsep.2024.103029

Hu, H., Yuan, W. W., Su, M., & Ou, K. (2023). Optimizing fuel economy and durability of hybrid fuel cell electric vehicles using deep reinforcement learning-based energy management systems. Energy Conversion and Management, 291, 117288. https://doi.org/10.1016/j.enconman.2023.117288

Khan, M. K., Houran, M. A., Kauhaniemi, K., Zafar, M. H., Mansoor, M., & Rashid, S. (2024). Efficient state of charge estimation of lithium-ion batteries in electric vehicles using evolutionary intelligence-assisted GLA–CNN–Bi-LSTM deep learning model. Heliyon, 10(15), e35183. https://doi.org/10.1016/j.heliyon.2024.e35183

Khan, U., Kirmani, S., Rafat, Y., Rehman, M. U., & Alam, M. S. (2024). Improved deep learning based state of charge estimation of lithium ion battery for electrified transportation. Journal of Energy Storage, 91, 111877. https://doi.org/10.1016/j.est.2024.111877

Krishna, G., Singh, R., Gehlot, A., Almogren, A., Altameem, A., Ur Rehman, A., & Hussen, S. (2024). Advanced battery management system enhancement using IoT and ML for predicting remaining useful life in Li-ion batteries. Scientific Reports, 14(1), 30394. https://doi.org/10.1038/s41598-024-80719-1

Lang, W., Hu, Y., Gong, C., Zhang, X., Xu, H., & Deng, J. (2022). Artificial Intelligence-Based Technique for Fault Detection and Diagnosis of EV Motors: A Review. IEEE Transactions on

Transportation Electrification, 8(1), 384–406. https://doi.org/10.1109/TTE.2021.3110318

Lee, J., Lee, E., & Kim, J. (2020). Electric vehicle charging and discharging algorithm based on reinforcement learning with data-driven approach in dynamic pricing scheme. Energies, 13(8), 1950. https://doi.org/10.3390/en13081950

Li, D., Liu, P., Zhang, Z., Zhang, L., Deng, J., Wang, Z., … Sauer, D. U. (2022). Battery Thermal Runaway Fault Prognosis in Electric Vehicles Based on Abnormal Heat Generation and Deep Learning Algorithms. IEEE Transactions on Power Electronics, 37(7), 8513–8525. https://doi.org/10.1109/TPEL.2022.3150026

Li, H., Chen, G., Yang, Y., Shu, B., Liu, Z., & Peng, J. (2024). Adversarial learning for robust battery thermal runaway prognostic of electric vehicles. Journal of Energy Storage, 82, 110381. https://doi.org/10.1016/j.est.2023.110381

Li, P., Zhang, Z., Xiong, Q., Ding, B., Hou, J., Luo, D., … Li, S. (2020). State-of-health estimation and remaining useful life prediction for the lithium-ion battery based on a variant long short term memory neural network. Journal of Power Sources, 459, 228069. https://doi.org/10.1016/j.jpowsour.2020.228069

Li, S., Hu, W., Cao, D., Dragicevic, T., Huang, Q., Chen, Z., & Blaabjerg, F. (2022). Electric Vehicle Charging Management Based on Deep Reinforcement Learning. Journal of Modern Power Systems and Clean Energy, 10(3), 719–730. https://doi.org/10.35833/MPCE.2020.000460

Lin, H., Yan, Y., & Cheng, Q. (2023). Future Role of Artificial Intelligence in Advancing Transportation Electrification. Journal of Intelligent and Connected Vehicles, 6(3), 183–186. https://doi.org/10.26599/JICV.2023.9210020

Lin, S. L. (2024). Deep learning-based state of charge estimation for electric vehicle batteries: Overcoming technological bottlenecks. Heliyon, 10(16), e35780. https://doi.org/10.1016/j.heliyon.2024.e35780

Lipu, M. S. H., Miah, M. S., Jamal, T., Rahman, T., Ansari, S., Rahman, M. S., … Shakib, M. N. (2024). Artificial Intelligence Approaches for Advanced Battery Management System in Electric Vehicle Applications: A Statistical Analysis towards Future Research Opportunities. Vehicles, 6(1), 22–70. https://doi.org/10.3390/vehicles6010002

Liu, W., Yao, P., Wu, Y., Duan, L., Li, H., & Peng, J. (2025). Imitation reinforcement learning energy management for electric vehicles with hybrid energy storage system. Applied Energy, 378, 124832. https://doi.org/10.1016/j.apenergy.2024.124832

Ma, Z., Huo, Q., Wang, W., & Zhang, T. (2023). Voltage-temperature aware thermal runaway alarming framework for electric vehicles via deep learning with attention mechanism in time-frequency domain. Energy, 278, 127747. https://doi.org/10.1016/j.energy.2023.127747

Mishra, S., Choubey, A., Devarasetty, S. V., Sharma, N., & Misra, R. (2024). An innovative multi-head attention model with BiMGRU for real-time electric vehicle charging management through deep reinforcement learning. Cluster Computing, 27(7), 9993–10023. https://doi.org/10.1007/s10586-024-04494-4

Naseri, F., Gil, S., Barbu, C., Cetkin, E., Yarimca, G., Jensen, A. C., … Gomes, C. (2023). Digital twin of electric vehicle battery systems: Comprehensive review of the use cases, requirements, and platforms. Renewable and Sustainable Energy Reviews, 179, 113280. https://doi.org/10.1016/j.rser.2023.113280

Nkechinyere Njoku, J., Ifeanyi Nwakanma, C., & Kim, D. S. (2024). Explainable Data-Driven Digital Twins for Predicting Battery States

in Electric Vehicles. IEEE Access, 12, 83480–83501. https://doi.org/10.1109/ACCESS.2024.3413075

Obuli Pranav, D., Babu, P. S., Indragandhi, V., Ashok, B., Vedhanayaki, S., & Kavitha, C. (2024). Enhanced SOC estimation of lithium ion batteries with RealTime data using machine learning algorithms. Scientific Reports, 14(1), 16036. https://doi.org/10.1038/s41598-024-66997-9

Sancarlos, A., Cameron, M., Abel, A., Cueto, E., Duval, J. L., & Chinesta, F. (2021). From ROM of Electrochemistry to AI-Based Battery Digital and Hybrid Twin. Archives of Computational Methods in Engineering, 28(3), 979–1015. https://doi.org/10.1007/s11831-020-09404-6

Shaker, B., Pietro Rosati Papini, G., Saveriano, M., & Liang, K. Y. (2024). Generating Synthetic Vehicle Data Using Decentralized Generative Adversarial Networks. IEEE Access, 12, 138076–138085. https://doi.org/10.1109/ACCESS.2024.3428369

Shern, S. J., Sarker, M. T., Ramasamy, G., Thiagarajah, S. P., Al Farid, F., & Suganthi, S. T. (2024). Artificial Intelligence-Based Electric Vehicle Smart Charging System in Malaysia. World Electric Vehicle Journal, 15(10), 440. https://doi.org/10.3390/wevj15100440

Sudhapriya, K., & Jaisiva, S. (2025). Implementation of artificial intelligence techniques in electric vehicles for battery management system. International Journal of Low-Carbon Technologies, 20, 590–604. https://doi.org/10.1093/ijlct/ctaf022

Sultan, Y. A., Eladl, A. A., Hassan, M. A., & Gamel, S. A. (2025). Enhancing electric vehicle battery lifespan: integrating active balancing and machine learning for precise RUL estimation. Scientific Reports, 15(1), 777. https://doi.org/10.1038/s41598-024-82778-w

Sultanuddin, S. J., Vibin, R., Rajesh Kumar, A., Behera, N. R., Pasha, M. J., & Baseer, K. K. (2023). Development of improved reinforcement learning smart charging strategy for electric vehicle fleet. Journal of Energy Storage, 64, 106987. https://doi.org/10.1016/j.est.2023.106987

Sumanasena, V., Gunasekara, L., Kahawala, S., Mills, N., De Silva, D., Jalili, M., … Jennings, A. (2023). Artificial Intelligence for Electric Vehicle Infrastructure: Demand Profiling, Data Augmentation, Demand Forecasting, Demand Explainability and Charge Optimisation. Energies, 16(5), 2245. https://doi.org/10.3390/en16052245

Sylvestrin, G. R., Maciel, J. N., Amorim, M. L. M., Carmo, J. P., Afonso, J. A., Lopes, S. F., & Ando Junior, O. H. (2025). State of the Art in Electric Batteries' State-of-Health (SoH) Estimation with Machine Learning: A Review. Energies, 18(3), 746. https://doi.org/10.3390/en18030746

Tran, M. K., Panchal, S., Chauhan, V., Brahmbhatt, N., Mevawalla, A., Fraser, R., & Fowler, M. (2022). Python-based scikit-learn machine learning models for thermal and electrical performance prediction of high-capacity lithium-ion battery. International Journal of Energy Research, 46(2), 786–794. https://doi.org/10.1002/er.7202

Tripp-Barba, C., Aguilar-Calderón, J. A., Urquiza-Aguiar, L., Zaldívar-Colado, A., & Ramírez-Noriega, A. (2025). A Systematic Mapping Study on State Estimation Techniques for Lithium-Ion Batteries in Electric Vehicles. World Electric Vehicle Journal, 16(2), 57. https://doi.org/10.3390/wevj16020057

Tuchnitz, F., Ebell, N., Schlund, J., & Pruckner, M. (2021). Development and Evaluation of a Smart Charging Strategy for an Electric Vehicle Fleet Based on Reinforcement Learning. Applied

Energy, 285, 116382. https://doi.org/10.1016/j.apenergy.2020.116382

Udeogu, C. U., & Lim, W. (2022). Improved Deep Learning-Based Energy Management Strategy for Battery-Supercapacitor Hybrid Electric Vehicle With Adaptive Velocity Prediction. IEEE Access, 10, 133789–133802. https://doi.org/10.1109/ACCESS.2022.3232062

Venkatesh Kumar, C., Chaturvedi, A., Arvin Tony, A., Srinivas, P. V. V. S., Ranjit, P. S., Rastogi, R., … Rajaram, A. (2024). AI-IOT-Based Adaptive Control Techniques for Electric Vehicles. Electric Power Components and Systems, 1–19. https://doi.org/10.1080/15325008.2024.2304685

Wang, H., Wang, X., & Fu, Z. (2025). Energy Management Strategy for Optimal Charge Depletion of Plug-In FCHEV Based on Multiconstrained Deep Reinforcement Learning. IEEE Transactions on Transportation Electrification, 11(1), 1077–1090. https://doi.org/10.1109/TTE.2024.3400020

Wu, B., Widanage, W. D., Yang, S., & Liu, X. (2020). Battery digital twins: Perspectives on the fusion of models, data and artificial intelligence for smart battery management systems. Energy and AI, 1, 100016. https://doi.org/10.1016/j.egyai.2020.100016

Yalçın, S., & Herdem, M. S. (2024). Optimizing EV Battery Management: Advanced Hybrid Reinforcement Learning Models for Efficient Charging and Discharging. Energies, 17(12), 2883. https://doi.org/10.3390/en17122883

Yan, S., Fang, H., Li, J., Ward, T., O'connor, N., & Liu, M. (2024). Privacy-Aware Energy Consumption Modeling of Connected Battery Electric Vehicles Using Federated Learning. IEEE Transactions on Transportation Electrification, 10(3), 6663–6675. https://doi.org/10.1109/TTE.2023.3343106

Yilmaz, M., Cinar, E., & Yazici, A. (2025). Federated Learning-Based State of Charge Estimation in Electric Vehicles Using Federated Adaptive Client Momentum. IEEE Access, 13, 72128–72141. https://doi.org/10.1109/ACCESS.2025.3563188

Zafar, M. H., Mansoor, M., Abou Houran, M., Khan, N. M., Khan, K., Raza Moosavi, S. K., & Sanfilippo, F. (2023). Hybrid deep learning model for efficient state of charge estimation of Li-ion batteries in electric vehicles. Energy, 282, 128317. https://doi.org/10.1016/j.energy.2023.128317

Zhang, H., Niyato, D., Zhang, W., Zhao, C., Du, H., Jamalipour, A., … Pei, Y. (2025). The Role of Generative Artificial Intelligence in Internet of Electric Vehicles. IEEE Internet of Things Journal, 12(6), 6208–6232. https://doi.org/10.1109/JIOT.2024.3511961

Zhao, K., Liu, Y., Zhou, Y., Ming, W., & Wu, J. (2025). Digital Twin-Supported Battery State Estimation Based on TCN-LSTM Neural Networks and Transfer Learning. CSEE Journal of Power and Energy Systems, 11(2), 567–579. https://doi.org/10.17775/CSEEJPES.2024.00900

Zhong, D., Liu, B., Liu, L., Fan, W., & Tang, J. (2025). Artificial Intelligence Algorithms for Hybrid Electric Powertrain System Control: A Review. Energies, 18(8), 2018. https://doi.org/10.3390/en18082018

CHAPTER 10

EV SAFETY AND MAINTENANCE PROCESSES

YÜCEL ÇETİNCEVİZ[1]
MUHAMMED TAN[2]

Introduction

The global automotive industry is undergoing its most significant transformation in a century, shifting from vehicles powered by internal combustion engines (ICEVs) to electric vehicles (EVs). This transition, driven by environmental and technological imperatives, extends far beyond the consumer experience; it fundamentally redefines the occupational risk landscape for the millions of technicians who diagnose, service, and repair these machines. For decades, automotive safety protocols have been built around the well-understood physicochemical hazards of ICEVs: managing flammable liquid fuels, mitigating exposure to toxic exhaust emissions, and handling high-temperature mechanical components (da Costa et al., 2025; Krzyżewska & Chruzik, 2023; Y. Liu et al., 2021). While these risks remain, the advent of the EVs introduces a new and distinct set of hazards rooted in high-potential

[1] Assoc. Prof. Dr., Kastamonu University, Department of Electrical and Electrical Engineering, Orcid: 0000-0001-6834-9442
[2] Assist. Prof., Kastamonu University, Department of Electrical and Electrical Engineering, Orcid: 0000-0003-0825-1325

electrical energy and the volatile chemistry of advanced battery systems. Figure 1 illustrates the key structural differences between ICEV and Battery EV (BEV) powertrains, emphasizing the presence of high-voltage components such as inverters, battery packs, and electric motors that replace combustion-based systems.

Figure 1 Comparison between Traditional Internal Combustion Engine Vehicle (ICEV) and Battery Electric Vehicle (BEV)

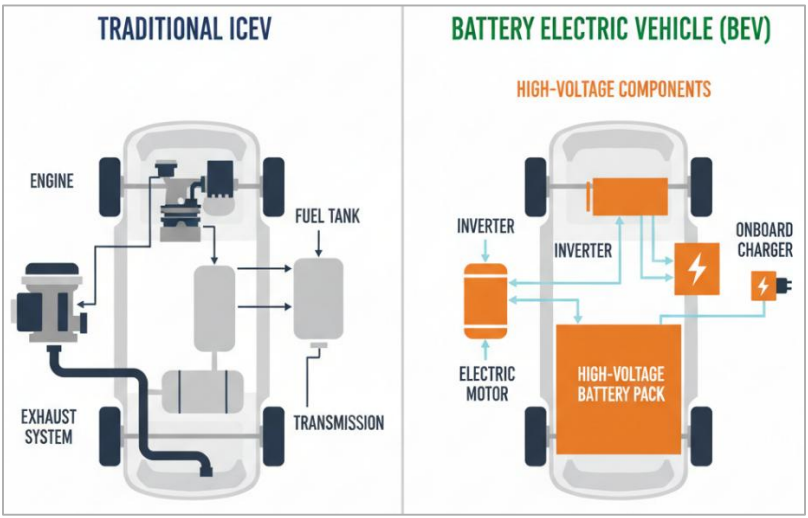

The New Hazard Landscape of Electric Vehicles

The primary occupational hazards unique to EV maintenance include the risk of severe electrical shock from high-voltage DC systems, the potential for thermal runaway and subsequent fire or explosion in lithium-ion batteries, and exposure to hazardous gases like hydrogen fluoride (HF) during battery incidents (Di Liberto, Borchiellini, Fruhwirt, & Papurello, 2025), (Dorsz & Lewandowski, 2021), (Jia et al., 2024). These dangers stand in stark contrast to the fuel-related fires and combustion byproducts characteristic of ICEVs. Concurrently, other, more subtle risks have emerged. The near-silent operation of EVs at low speeds, for example, presents a

novel acoustic hazard in busy workshop environments, increasing the risk of collisions between personnel and moving vehicles (M. del C. Pardo-Ferreira, Rubio-Romero, Galindo-Reyes, & Lopez-Arquillos, 2020), (M. C. Pardo-Ferreira, Torrecilla-García, de las Heras-Rosas, & Rubio-Romero, 2020). Furthermore, the increased mass of EVs, largely due to their battery packs, may lead to higher generation of non-exhaust particulate matter from tire and brake wear, impacting air quality within service centers (Y. Liu et al., 2021), (da Costa et al., 2025). As illustrated in Figure 2, these evolving occupational hazards demonstrate a paradigm shift from traditional fire and exhaust risks to high-voltage, chemical, and environmental exposures unique to electric vehicle technologies.

Figure 2 Occupational hazard transition in the automotive industry from ICEV to EV

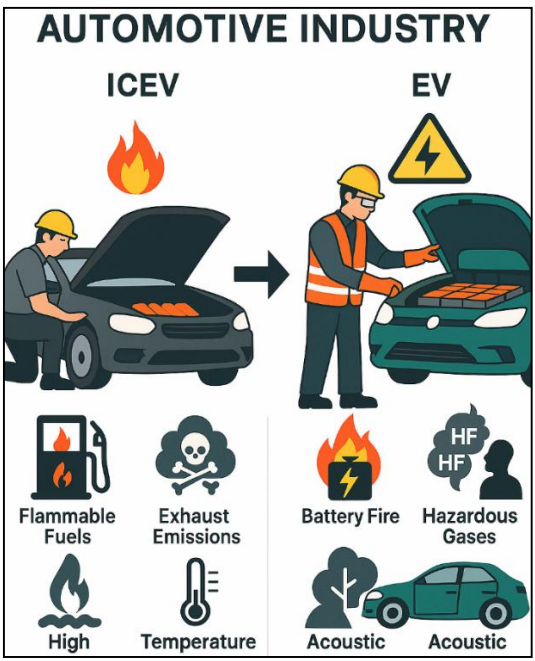

This chapter provides a comprehensive, science-based overview of the key safety challenges and hazard management

protocols essential for the modern automotive service industry. It moves from the foundational principles of high-voltage electrical safety and battery chemistry to the practical application of safe work processes, specialized equipment, and emergency response. By synthesizing the latest research and international standards, this chapter aims to provide a universally applicable guide for technicians, safety managers, first responders, and engineers operating in this rapidly evolving field.

High-Voltage Systems: The Electrical Hazard and Its Human Impact

The defining feature of an EV's powertrain is its high-voltage (HV) direct current (DC) architecture, typically operating between 400 and 800 volts, with future systems poised to exceed 1,000 volts. This level of electrical potential presents a lethal hazard that demands a complete paradigm shift from the 12V DC systems of traditional vehicles. Managing this risk requires a dual understanding: first, of the robust engineering controls and safety protocols designed to isolate this energy, and second, of the severe physiological consequences should these defenses be breached.

Engineering Controls and Safety Protocols for HV Systems

To ensure technician safety, a multi-layered system of engineering controls and procedural protocols is mandated by international standards, including UNECE R100, FMVSS 305, and the functional safety standard ISO 26262 (Grebtsov et al., 2024; Kurian & Abbasian, 2025; Lian, Zeng, Ye, Zhao, & Wei, 2018; Wöhrl, Geisbauer, Nebl, Lott, & Schweiger, 2021). The fundamental principle of this framework is to ensure that the HV system can be rapidly and reliably isolated and de-energized before any service work commences. These standards mandate that, in the event of a crash or manual service disconnect, the voltage at any accessible point must be reduced to below 60V DC within five seconds (Kurian

& Abbasian, 2025), (Wöhrl et al., 2021). Figure 3 provides a concise overview of the multi-layered high-voltage safety architecture in EVs, highlighting Lockout/Tagout (LOTO) procedures, main contactors, capacitor discharge circuits, and insulation monitoring as the core engineering barriers that protect technicians from electrical hazards.

Figure 3 A visual summary of the multi-layered safety system for HV EV systems

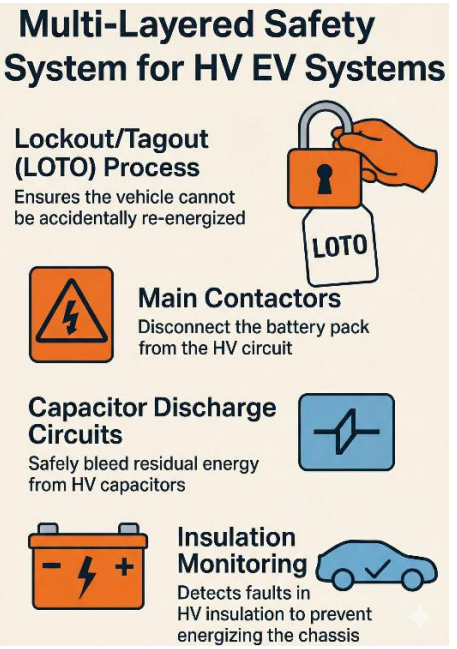

This is achieved through several key engineering controls integrated into the vehicle's design:

- **Main Contactors:** These are high-power relays that physically disconnect the battery pack from the rest of the HV circuit, acting as the primary line of defense (Chandran, Hennen, Arkkio, & Belahcen, 2022; Muram,

Pop, & Javed, 2024), (Jiang, Diao, Zhang, Zhang, & Li, 2021).

- **Capacitor Discharge Circuits:** HV systems contain capacitors that can store a dangerous charge even after the battery is disconnected. Pre-charge and discharge circuits are designed to safely bleed this residual energy, often by routing it through motor windings or dedicated resistors (Chandran et al., 2022; Kurian & Abbasian, 2025), (Yang, Yang, & Zhang, 2021).

- **Insulation Monitoring and Galvanic Isolation:** The vehicle's Battery Management System (BMS) continuously monitors the insulation resistance between the HV circuit and the vehicle chassis. A drop in resistance triggers a fault condition, isolating the system to prevent the chassis from becoming energized (Chandran et al., 2022; Jiang et al., 2021; Wöhrl et al., 2021)

- **Interlock Loops and Physical Barriers:** A low-voltage interlock circuit runs through all HV components. If any component is disconnected without following the proper procedure, this loop is broken, and the main contactors open automatically. This is supplemented by physical barriers, such as distinctively colored orange conduits and warning labels, to prevent inadvertent contact (Grebtsov et al., 2024; Muram et al., 2024).

Building upon these engineering controls is the procedural cornerstone of HV safety: the **Lockout/Tagout (LOTO)** process. Adapted from industrial electrical safety, LOTO ensures that the vehicle cannot be accidentally re-energized while under service. However, LOTO for EVs must be modified from traditional applications, as a battery pack cannot be fully "de-energized" at its

source (Grebtsov et al., 2024; Rosewater, 2023; Wöhrl et al., 2021). The process involves switching off the vehicle, disconnecting the 12V battery, removing the manual service disconnect, and then verifying with a calibrated voltmeter that there is zero potential between HV lines and between each line and the chassis. Only after this verification can work begin.

The Physiological Consequences of High-Voltage DC Shock

The stringent nature of these protocols is a direct reflection of the severe medical consequences of high-voltage DC electric shock. Unlike the lower-voltage shocks that might be survivable, contact with an EV's HV system can inflict devastating, multi-system trauma that is often life-threatening and can lead to permanent disability (Ahmed et al., 2021; Dechent et al., 2020; Shih, Shahrokhi, & Jeschke, 2017). The severity is determined by the voltage, the current's path through the body, and the duration of contact. Figure 4 illustrates the primary physiological effects of high-voltage DC shock.

Figure 4 An overview of the major physiological consequences of high-voltage DC shock

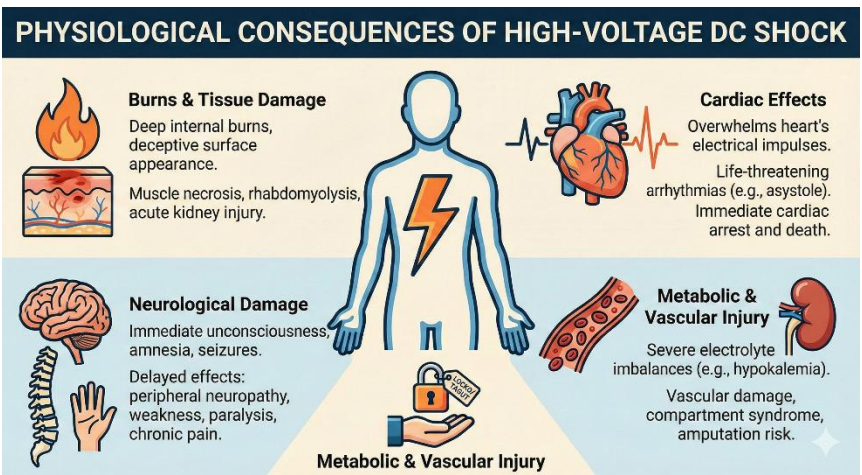

Key physiological effects include:

- **Burns and Tissue Damage:** High-voltage DC shock causes deep internal burns, which may appear deceptively minor on the skin's surface at the entry and exit points (Boyd, Hartman, Sood, & Walroth, 2019; Dechent et al., 2020). The current can cause extensive muscle necrosis (tissue death) deep within the body, leading to a condition called rhabdomyolysis. This releases large amounts of myoglobin into the bloodstream, which can cause acute kidney injury and failure (Baker, Binda, Nozari, & Baker, 2024; Boyd et al., 2019).

- **Cardiac Effects:** The heart's rhythm is controlled by precise electrical impulses. A high-voltage DC shock can overwhelm this system, causing life-threatening arrhythmias. While alternating current (AC) is more likely to induce ventricular fibrillation, high-voltage DC is particularly associated with asystole (cardiac standstill) (Spies & Trohman, 2006; Waldmann et al., 2018). Both can result in immediate cardiac arrest and death, especially if the current's path crosses the chest (Ahmed et al., 2021; Ogbuka, Avera, & King, 2023).

- **Neurological Damage:** The central and peripheral nervous systems are profoundly vulnerable. A shock can cause immediate unconsciousness, amnesia, and seizure-like activity. Delayed and long-term effects are common, including peripheral neuropathy (nerve damage in the limbs), muscle weakness, sensory loss, and even paralysis (Biering, Kærgaard, Carstensen, & Nielsen, 2023; Boudier-Revéret, Hsiao, Shyu, & Chang, 2020; Dechent et al., 2020). Cognitive deficits and chronic pain syndromes can persist long after the initial injury (Khor et al., 2023; Rådman, Nilsagård, Jakobsson, Ek, & Gunnarsson, 2016).

- **Metabolic and Vascular Injury:** The shock can trigger severe electrolyte imbalances, such as hypokalemia (low

potassium), which can itself lead to paralysis or cardiac complications (Baker et al., 2024). Furthermore, damage to blood vessels can result in compartment syndrome, a condition where swelling in a confined space (like a limb) cuts off blood supply, requiring emergency surgical intervention to prevent amputation (Andrews, 2012; Baker et al., 2024).

Any individual who experiences a high-voltage electrical shock requires immediate and comprehensive medical evaluation, even if they appear unharmed externally. The risk of delayed cardiac or neurological events necessitates a period of careful observation in a hospital setting.

The Heart of the Hazard: Battery Pack Safety and Thermal Runaway

The lithium-ion battery pack is the heart of the modern electric vehicle, providing the energy density required for acceptable range and performance. However, this dense concentration of electrochemical energy also represents the vehicle's most significant and unique chemical hazard. The primary risk associated with these batteries is **thermal runaway**, a violent and self-sustaining chain reaction that can lead to fire, explosion, and the release of toxic gases. Understanding the science behind this phenomenon and the protocols for managing compromised battery packs is paramount for ensuring safety.

The Science of Thermal Runaway: Causes and Mitigation

Thermal runaway is initiated when a battery cell is subjected to conditions that are outside its safe operating window. These triggers, broadly categorized as abuse conditions, lead to a rapid, uncontrolled increase in internal temperature. Figure 5 illustrates the progression from initial trigger (mechanical, electrical, or thermal

abuse) to Solid Electrolyte Interphase (SEI) breakdown, gas venting with rapid heat escalation, and final propagation to adjacent cells.

Figure 5 A step-by-step illustration of the lithium-ion battery thermal runaway process

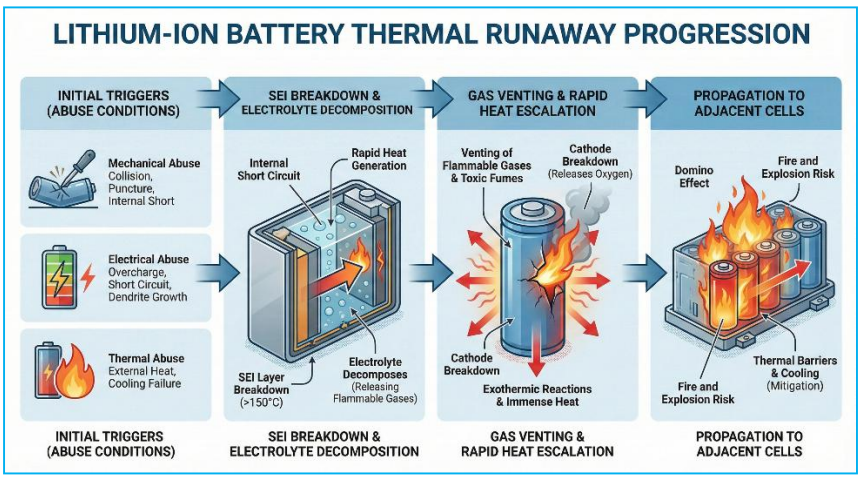

The primary causes are:

- **Mechanical Abuse:** Physical damage to the battery, such as from a vehicle collision or puncture during service, can cause an internal short circuit by bringing the anode and cathode into direct contact (Feng et al., 2018; Ren et al., 2021; Tran et al., 2022).

- **Electrical Abuse:** Overcharging, over-discharging, or an external short circuit can cause excessive current flow and heat generation, leading to the breakdown of internal components (Abada et al., 2018; Song, Zheng, Xiao, Wang, & Long, 2022; Zhou et al., 2025). The growth of lithium dendrites—microscopic, needle-like structures that can form during improper charging—is a common cause of internal short circuits (Feng et al., 2018; Tran et al., 2022).

- **Thermal Abuse:** Exposing the battery to external heat sources or allowing it to overheat due to a failure in the vehicle's cooling system can initiate the same decomposition reactions (Jindal & Bhattacharya, 2019; J. Zhang, Zhang, Sun, & Wang, 2018).

Once triggered, a sequence of exothermic (heat-releasing) chemical reactions begins, starting with the breakdown of the SEI layer on the anode. SEI decomposition generally begins at 80°C, but rapid escalation occurs after 150-200°C, beyond which, flammable gases are released. This is followed by the breakdown of the cathode material, releasing oxygen, which then feeds the combustion of the flammable electrolyte gases. This process generates immense heat, often leading to the thermal runaway propagating to adjacent cells in a domino effect (Abada et al., 2018; Feng et al., 2018; Ren et al., 2021).

Mitigation strategies are therefore designed at every level of the battery's construction and management:

- **Material Level:** Research is focused on developing more stable materials, such as non-flammable electrolytes, flame-retardant separators that resist puncture, and cathode chemistries (like Lithium Iron Phosphate, LFP) that are inherently less prone to thermal decomposition than higher-energy chemistries (like Nickel Manganese Cobalt, NMC) (Feng, Ren, He, & Ouyang, 2020; Song et al., 2022; Wu et al., 2025; Zhou et al., 2025).
- **Cell and Module Level:** Engineering solutions are employed to prevent propagation between cells. These include thermal barriers or insulating materials, phase-change materials that absorb heat, and robust cooling systems (liquid or immersion cooling) to dissipate heat

effectively (B. Liu et al., 2023; Rui et al., 2021; Zuo, Li, Liang, Wang, & Ouyang, 2025).

- **System Level:** The Battery Management System (BMS) is the brain of the battery pack. It continuously monitors voltage, current, and temperature for each cell. Advanced BMS algorithms can detect the early signs of a fault, isolate the problematic section of the pack, and trigger warnings for the driver and service technicians. Modern systems increasingly use AI-driven prognostics to predict failures before they occur (Choi et al., 2025; Hong et al., 2023; Shahid & Agelin-Chaab, 2022; X. Zhang, Chen, Zhu, & Gao, 2023).

Managing Damaged and Compromised Battery Packs

While prevention is the primary goal, technicians and recovery services must be prepared to handle battery packs that have already been compromised, whether through a collision, an internal fault, or improper handling. This is a high-risk activity that requires specialized procedures.

- **Handling and Personnel:** Only personnel with specific high-voltage training should handle damaged battery packs. They must use insulated, voltage-proof tools and wear appropriate Personal Protective Equipment (PPE) to protect against both electrical and chemical hazards (Beghi, Braghin, & Roveda, 2023; Villagrossi & Dinon, 2023; Wöhrl et al., 2021). Whenever possible, robotic or human-robot collaborative systems should be used for disassembly to minimize human exposure (Kay, Farhad, Mahajan, Esmaeeli, & Hashemi, 2022; Villagrossi & Dinon, 2023).

- **Deactivation and Discharge:** Before removal or disassembly, the pack must be electrically isolated from the vehicle. If deemed safe, the pack should be discharged to a stable voltage. However, over-discharging certain cell types can create its own hazards, such as swelling and gas generation, so manufacturer guidelines must be strictly followed (Lee, Kim, & Lee, 2023; Wöhrl et al., 2021; Zorn et al., 2022).

- **Storage and Isolation:** A damaged battery pack must be treated as unstable. It should be stored in a designated, well-ventilated "quarantine" area, ideally outdoors and away from any flammable materials or structures to contain any potential fire or toxic gas release (Wöhrl et al., 2021). For packs deemed at high risk of thermal runaway, storage in specialized fire-resistant containers or emergency enclosures is recommended (Cui, Liu, Han, Sun, & Cong, 2022; Wöhrl et al., 2021).

- **Diagnostics and Monitoring:** Advanced diagnostic tools are essential to assess the state of a compromised pack. The BMS data is the first source of information. Beyond that, technicians can use tools that analyze voltage inconsistencies, internal resistance, and other parameters to identify faulty cells (Kang, Duan, Zhou, Shang, & Zhang, 2020; Wójcik & Przystałka, 2025; G. Xu et al., 2022). Real-time, wireless data transmission from the pack would be a significant safety advancement, allowing service teams to assess its condition remotely before approaching (Wöhrl et al., 2021; Wójcik & Przystałka, 2025).

A Framework for Safe Work Processes

Effective safety management in an EV service environment extends beyond understanding specific high-risk hazards. It requires a holistic framework that categorizes all workshop activities according to their level of risk and establishes clear, repeatable Standard Operating Procedures (SOPs) for each. This ensures that every individual who interacts with the vehicle—from sales staff and detailers to master technicians—is equipped with the appropriate level of knowledge and follows the correct safety protocols. A globally applicable risk assessment model provides the foundation for this framework, ensuring that safety is not just reserved for high-voltage work but is integrated into every aspect of the vehicle's lifecycle.

A Universal Risk Assessment Model for EV Service Tasks

While many advanced risk assessment methodologies like Failure Mode and Effects Analysis (FMEA) and Fault Tree Analysis (FTA) are used to evaluate technical hazards in EVs, particularly related to battery systems (Gusti et al., 2025; Mohd Tohir & Martín-Gómez, 2023; Zhao et al., 2024), there is a need for a simpler, task-based model for daily workshop operations. A globally applicable model can be structured as a tiered or matrix-based system that classifies tasks based on the potential for exposure to EV-specific hazards. Figure 6 provides a visual overview of this safety protocol, illustrating the required equipment and isolation procedures relative to the risk level.

Figure 6 The proposed three-tiered risk assessment framework illustrating the progression from low-risk tasks to HV operations

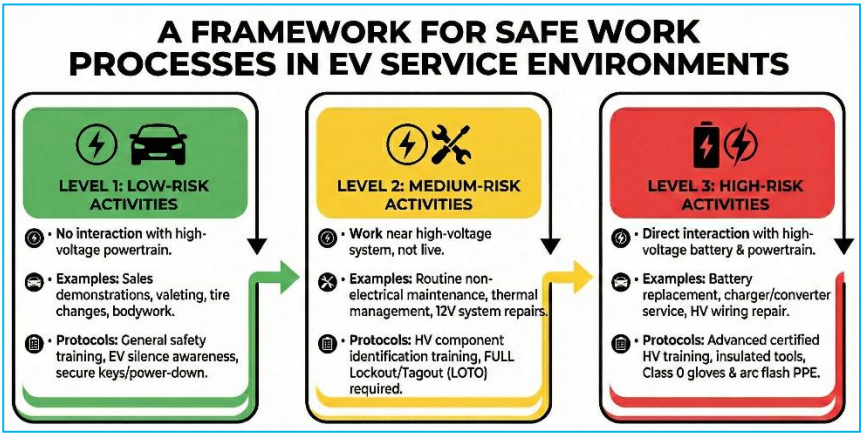

A proposed three-tiered risk model could be structured as follows:

- **Level 1: Low-Risk Activities.** These are tasks that do not involve interaction with the high-voltage powertrain or its direct control systems. The primary risks are general occupational hazards and the EV-specific acoustic risk.

    1. *Examples:* Vehicle sales demonstrations, interior and exterior cleaning (valeting), tire changes, and bodywork repairs on non-powertrain areas.

    2. *Required Protocols:* General workplace safety training, specific awareness training on the silent nature of EVs, and procedures for ensuring the vehicle is powered down and the keys are secured to prevent unexpected movement (Beşiktaşli & Yurtcu, 2025; Chombo, Laoonual, & Wongwises, 2021).

- **Level 2: Medium-Risk Activities.** These tasks involve working on or near the high-voltage system but do not require the system to be live. The primary risk is accidental energization or contact with residual voltage if proper procedures are not followed.

    1. *Examples:* Routine maintenance on non-electrical systems (brakes, suspension), service of the vehicle's thermal management system, and repairs on the 12V auxiliary electrical system.

    2. *Required Protocols:* All Level 1 protocols, plus specific training on identifying HV components. Crucially, these tasks require the full de-energization and Lockout/Tagout (LOTO) procedure to be performed before work begins (Beşiktaşli & Yurtcu, 2025; Gusti et al., 2025).

- **Level 3: High-Risk Activities.** These are tasks that involve direct interaction with the high-voltage battery and powertrain components, and may include live-system diagnostics. The risk of severe electrical shock, arc flash, or triggering a battery fault is significant.

    1. *Examples:* Diagnosing and replacing a battery pack, servicing the onboard charger or DC-DC converter, and repairing damaged high-voltage wiring.

    2. *Required Protocols:* All Level 1 and 2 protocols. These tasks must only be performed by technicians with advanced, certified HV training. They require the use of

specialized insulated tools, diagnostic equipment, and the full range of Personal Protective Equipment (PPE), including Class 0 insulating gloves and arc flash protection (Chen, Li, & Yang, 2022; Muram et al., 2024).

This model provides a clear framework for assigning work, defining training requirements, and ensuring that safety measures are proportional to the risk of the task at hand. While a globally standardized version of this model is still evolving, its principles are foundational to safe workshop management (Chen et al., 2022; Chombo et al., 2021; Gusti et al., 2025).

Safety in Routine Maintenance: The Importance of the 12V System

Even when performing medium-risk tasks that do not directly involve the HV system, specific safety protocols are essential. The vehicle's 12V auxiliary battery, while not a high-voltage threat itself, acts as the control system for the entire vehicle, including the high-voltage main contactors (Bisschop, Willstrand, & Rosengren, 2020). Failure to properly manage the 12V system can lead to unexpected energization of the HV circuit.

The required safety protocols for any routine maintenance or repair, even on non-electrical systems, must therefore include:

- **Vehicle Deactivation:** Ensure the vehicle is fully powered down, the ignition is off, and the key fob is stored at a safe distance away to prevent passive activation (Bisschop et al., 2020).
- **Disconnect the 12V Battery:** Before any work begins, the ground cable of the 12V battery should be disconnected. This is a critical step that prevents the

accidental closing of the HV contactors and activation of other vehicle systems (Bisschop et al., 2020).

- **Allow for System Discharge:** While the most significant capacitor discharge happens in the HV system (which should already be confirmed safe via LOTO), it is good practice to wait a few minutes after disconnecting all power to ensure all auxiliary systems are fully discharged (Bisschop et al., 2020). Figure 7 illustrates the sequential execution of these isolation steps, highlighting the necessary protective equipment and the verification process to ensure a "zero energy" state.

Figure 7 Standard Operating Procedure for Equipment Selection and Vehicle Isolation (LOTO)

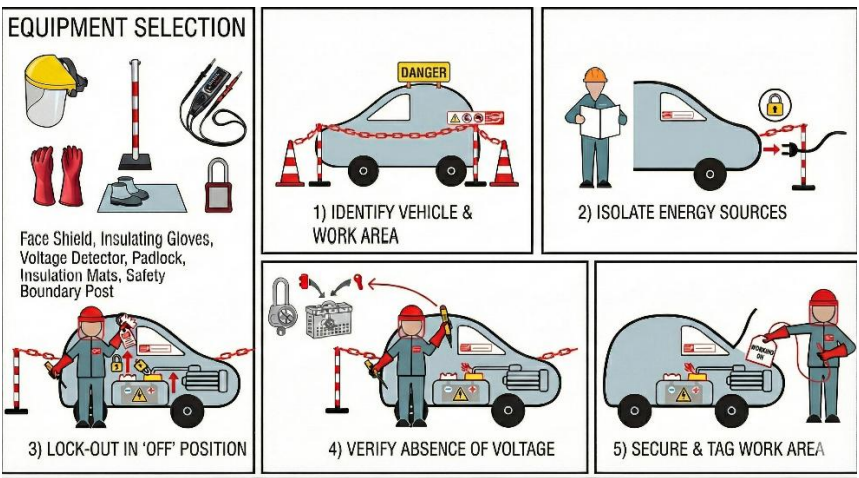

- **Mark the Vehicle:** Clearly mark the vehicle as being under service to alert other personnel that its systems are disconnected and it should not be operated (Bisschop et al., 2020). As depicted in Figure 8, this involves establishing a physical perimeter with clear warning

signage to prevent unauthorized access to the high-risk zone.

Figure 8 Safe Work Station Setup and Perimeter Delineation

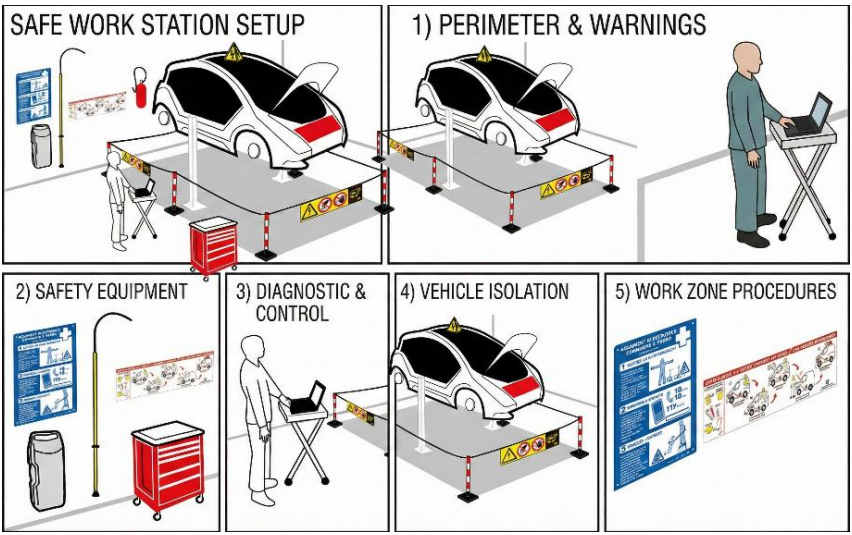

Adherence to these simple but critical steps ensures that technicians are protected from accidental activation of the high-voltage system, even when their primary task is unrelated to the powertrain.

The Technician's Defenses: Specialized Tools, Equipment, and Personal Protective Equipment (PPE)

Safe interaction with high-voltage electric vehicle systems is contingent upon a triad of physical defenses: specialized insulated tools to prevent the flow of electricity, advanced diagnostic equipment to assess the state of the system without direct exposure, and certified Personal Protective Equipment (PPE) to shield the technician from harm in the event of an unforeseen incident. The efficacy of these defenses is not arbitrary; it is defined by rigorous material science and governed by international standards that specify their performance under high-voltage DC conditions.

Essential Insulated Tools and Diagnostic Equipment

Standard workshop tools are conductors of electricity and become an extension of a live circuit if they make contact. Therefore, any hand tool used on or near an EV's high-voltage system must be specifically designed and certified for electrical work. The primary international standard governing these tools is **IEC 60900**, which mandates that tools be tested to withstand 10,000V AC and are rated for safe use on live circuits up to 1,000V AC and 1,500V DC (Borghei & Ghassemi, 2021; C. Li et al., 2022; Riba, Moreno-Eguilaz, & Bogarra, 2023). These tools feature robust, multi-layered insulation made from high-grade polymers, ensuring both dielectric strength and mechanical durability (Haque et al., 2021; Riba et al., 2023; Saleem & Akbar, 2022). The essential kit for an EV technician includes:

- Insulated screwdrivers, pliers, and cutters.
- Insulated socket sets and torque wrenches.
- A calibrated, CAT III or CAT IV rated multimeter with insulated probes for voltage verification.

Alongside these hand tools, advanced diagnostic equipment is crucial for safely assessing the health of the HV insulation system without invasive procedures. This equipment allows technicians to detect degradation or faults that could lead to system failure or create a shock hazard. Key diagnostic tools include:

- **Insulation Resistance Testers (Megohmmeters):** These devices apply a known DC voltage to the system and measure the resistance of the insulation. A low reading indicates a potential breach in the insulation, which could energize the vehicle's chassis (Biswas et al., 2024; Borghei & Ghassemi, 2021; Takada et al., 2017).

- **Partial Discharge (PD) Detectors:** Partial discharges are small electrical sparks that occur in voids or defects within an insulation material. They are an early indicator of insulation breakdown. Non-contact PD detectors can identify these events through their electromagnetic or acoustic signatures, allowing for predictive maintenance [S5-3, S5-10, S5-12].

- **Thermal Imaging Cameras:** These cameras can identify hotspots in the battery pack, wiring, or power electronics that may indicate high resistance connections or failing components, often a precursor to a more serious failure (Biswas et al., 2024; Ivanov, Sadykov, Yaroslavsky, Golenishchev-Kutuzov, & Galieva, 2021).

Personal Protective Equipment (PPE) and Governing Standards

While tools and procedures are the first lines of defense, PPE is the last and most critical barrier protecting the technician. The selection and maintenance of PPE for HV work are non-negotiable. Figure 9 visualizes this critical safety ensemble, highlighting the specific items such as insulating gloves, face shields, and mats that form the barrier between the technician and high-voltage hazards.

The essential categories of PPE include:

- **Insulating Gloves:** These are the most critical piece of PPE. They are typically made of rubber or a synthetic elastomer and are rated by class for the voltage they can protect against (Class 0 gloves, rated for 1,000V AC / 1,500V DC, are standard for EV work). They must be protected from mechanical damage by leather over-gloves and must be visually inspected for damage and be air-tested before every use. Standards like **ASTM D120**

and **EN 60903** govern their testing and certification (Angalane & Kasinathan, 2022; Borghei & Ghassemi, 2021; C. Li et al., 2022; Riba et al., 2023).

Figure 9 Essential Personal Protective Equipment (PPE) and safety tools for high-voltage interventions

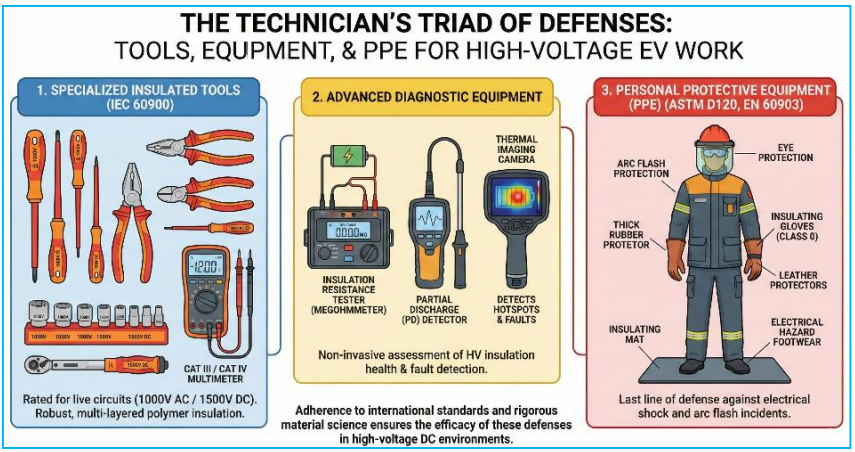

- **Electrical Hazard Footwear and Insulating Mats:** Dielectric footwear prevents the technician from completing a circuit to the ground. For added protection, insulating rubber mats should be used on the floor of the work area to provide an additional layer of isolation (Borghei & Ghassemi, 2021; C. Li et al., 2022; Riba et al., 2023).

- **Arc Flash Protection:** An arc flash is a violent electrical explosion that can occur during a short circuit, releasing intense heat, light, and a pressure wave. For high-risk procedures, technicians must wear arc-rated clothing and a face shield to protect against severe burns and injury (Angalane & Kasinathan, 2022; Borghei & Ghassemi, 2021; Riba et al., 2023).

- **Eye Protection:** Safety glasses are mandatory for all tasks to protect against projectiles and chemical splashes.

The materials used in these tools and PPE are at the forefront of polymer science research. Materials like cross-linked polyethylene (XLPE), polypropylene (PP), and various epoxy resins are continually being improved. The addition of nanocomposite materials can significantly enhance dielectric strength, thermal stability, and resistance to "tracking"—the formation of a conductive path across the surface of an insulator (Bjurström et al., 2024; Haque et al., 2021; Paramane et al., 2020; Pleşa, Noţingher, Schlögl, Sumereder, & Muhr, 2016; Riba et al., 2023). As EV systems push towards higher voltages, ongoing innovation in these materials and the standards that govern them will be essential for maintaining technician safety (Angalane & Kasinathan, 2022; C. Li et al., 2022; Shahsavarian et al., 2021).

When Prevention Fails: Emergency Response and Incident Management

While robust engineering and diligent workshop procedures are designed to prevent incidents, it is imperative that first responders and recovery services are prepared for worst-case scenarios involving electric vehicle collisions and fires. EV incidents present a unique combination of hazards—high-voltage electricity, volatile battery chemistry, and the potential for re-ignition—that differ significantly from those of traditional vehicles. Effective management requires specialized knowledge, protocols, and equipment to ensure the safety of both the responders and the public.

Protocols for First Responders and Recovery Services

A significant challenge in the field is the gap between the rapid pace of EV adoption and the level of specific training provided to emergency personnel. Surveys have revealed that many first

responders, particularly outside of specialized firefighting units, lack adequate preparedness for handling EV incidents (J. Liu, Xu, Shi, Barnett, & Jones, 2023; Stave & Carlson, 2017).

Best practices and established protocols for managing EV incidents are therefore centered on a systematic approach to hazard identification and mitigation: Figure 10 outlines this systematic 5-stage protocol, guiding responders from initial vehicle identification through to post-incident quarantine.

Figure 10 The 5-stage emergency response protocol for electric vehicle incidents

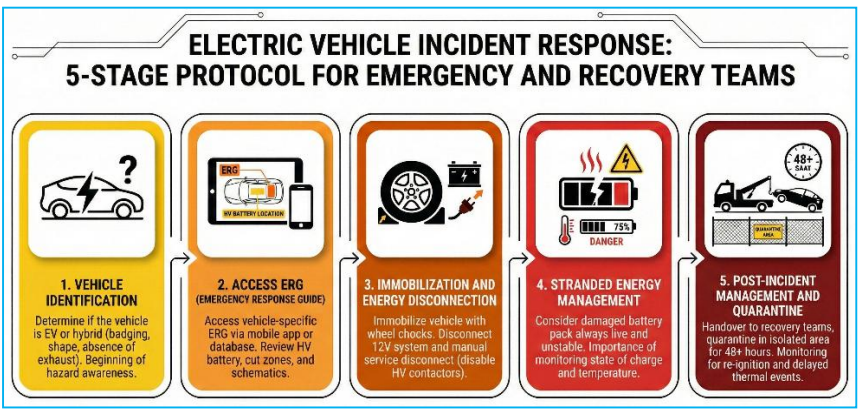

- **Vehicle Identification:** The first and most critical step is to identify the vehicle as an EV or hybrid. This is done through badging, vehicle shape, or the absence of an exhaust pipe. This immediately shifts the incident response mindset to consider electrical and battery hazards.

- **Accessing Emergency Response Guides (ERGs):** Once identified, responders must access the vehicle-specific ERG. These guides, often available through mobile apps or databases, provide crucial schematics showing the

location of the high-voltage battery, disconnect loops, and cut zones for extrication, helping responders avoid contact with energized components (Wöhrl et al., 2021; B. Zhang, Tanim, & Black, 2025).

- **Immobilization and De-energization:** The vehicle must be immobilized (e.g., with wheel chocks) and the 12V system disconnected to deactivate the HV contactors. If safe and accessible, the manual service disconnect should also be operated.

- **Managing Stranded Energy:** A key concern in a post-crash scenario is "stranded energy"—the electrical energy remaining in a damaged battery pack that cannot be safely discharged (Wöhrl et al., 2021; B. Zhang, Bewley, Tanim, & Walker, 2022). A damaged pack must always be treated as live and unstable. Real-time access to the battery's state of charge and temperature data at the scene would be a major safety advancement, but is not yet widely available (Wöhrl et al., 2021; B. Zhang et al., 2025).

- **Post-Incident Handling:** After the initial incident is controlled, the vehicle must be handed over to recovery services with clear communication about its state. The vehicle should be stored in a secure, isolated area for a quarantine period (typically 48 hours or more) to monitor for delayed thermal events or re-ignition (Bisschop et al., 2020; Wöhrl et al., 2021).

The Science of Suppressing Lithium-Ion Battery Fires

Figure 11 shows lithium-ion batteries used in an EV. Whether used in cars or electronic devices, lithium-ion batteries can catch fire if improperly manufactured or damaged, or if the software that

operates the battery is not designed correctly. A lithium-ion battery fire is not a typical Class A or B fire; it is a thermal and chemical event. The goal of suppression is not just to extinguish the visible flames but to cool the battery cells below their thermal runaway threshold to halt the internal chain reaction.

Figure 11 Lithium-ion batteries used in an EV

Source: (Pollard, 30.11.2025)

Extensive full-scale fire testing has led to a consensus on the most effective extinguishing agents and strategies:

- **Water and Water Mist:** Water is consistently identified as the most effective agent for suppressing lithium-ion battery fires, primarily due to its high heat capacity and cooling effect (Ghiji et al., 2020; J. Xu et al., 2020; L. Zhang et al., 2021). Applying large, continuous volumes of water directly to the battery pack is the primary strategy. Water mist systems are particularly effective, as the smaller droplets have a larger surface area, leading to more efficient heat absorption and cooling (Ji, Liu, Qi,

Zhang, & Zhang, 2023; Majeed et al., 2024; L. Zhang et al., 2021).

- **Water with Additives:** Additives like surfactants (e.g., F-500) can enhance water's effectiveness by breaking surface tension and allowing it to penetrate deeper into the battery module, improving cooling and reducing the total volume of water needed (Ghiji et al., 2020; Tang, Yuan, Thomas, & Soles, 2023; Ubaldi et al., 2024).

- **Other Agents:**

    1. *Gaseous agents* (e.g., CO_2, $C_6F_{12}O$) can suppress flames by displacing oxygen but provide little to no cooling effect, making re-ignition highly likely (Majeed et al., 2024; L. Zhang et al., 2020).

    2. *Dry powders* can also extinguish flames but similarly fail to address the underlying thermal issue (X. Li et al., 2023; Yuan et al., 2021).

    3. *Fire blankets* can be effective for containing a fire in its early stages and preventing its spread to surroundings, but they do not extinguish the internal reaction (Ji et al., 2023; Tang et al., 2023).

    4. *Novel agents* like liquid nitrogen and hydrogels show promise for their exceptional cooling properties, but their practical application in a dynamic roadside incident is challenging (Ping et al., 2024; Wang et al., 2025).

A critical consideration in EV firefighting is the potential for toxic gas release, especially in confined spaces like underground parking garages where concentrations of hydrogen fluoride can reach lethal levels (Chang et al., 2025; Ubaldi et al., 2024). Furthermore, the runoff water from firefighting is often highly toxic and contaminated with heavy metals and chemicals from the battery, requiring environmental remediation (Ubaldi et al., 2024; Wang et al., 2025). Figure 12 summarizes these suppression strategies, highlighting the primary role of cooling agents and the associated safety and environmental risks.

Figure 12 Overview of suppression agents, strategies, and critical considerations for EV lithium-ion battery fires

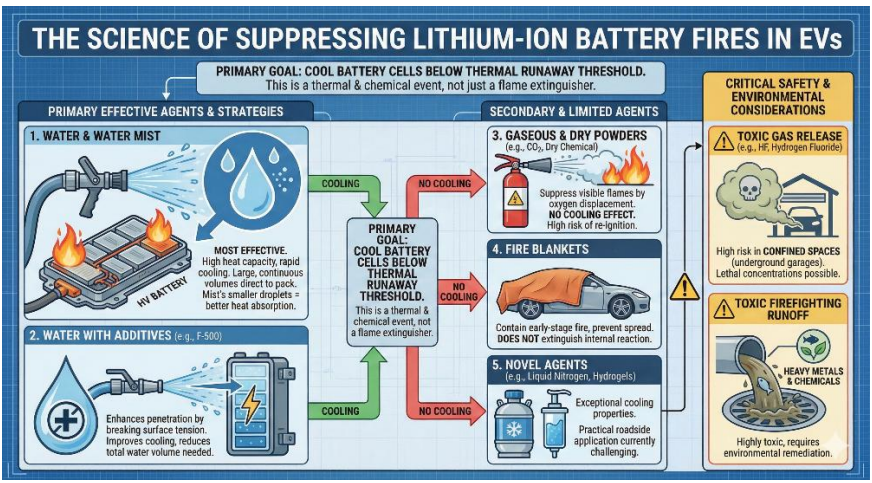

Conclusion: Navigating the Future of Electric Vehicle Safety

The electrification of the automotive fleet represents a monumental leap forward in technology, but it also establishes a new and complex frontier for occupational safety. The transition from managing the risks of hydrocarbon fuels to mitigating the hazards of high-voltage electricity and dense electrochemical energy storage

requires a fundamental evolution in training, technology, and safety culture. As this chapter has detailed, a robust safety framework for the EV era is built on a multi-layered, science-based approach that addresses every stage of the vehicle's service lifecycle.

The core principles of this framework are now well-established. They begin with a deep understanding of the primary hazards: the immediate, lethal threat of high-voltage DC shock and the persistent, volatile danger of thermal runaway in lithium-ion batteries. They are put into practice through a combination of advanced engineering controls integrated into the vehicle, stringent and repeatable safe work protocols like Lockout/Tagout, and the diligent use of specialized insulated tools and personal protective equipment governed by international standards. This proactive system is backed by responsive emergency protocols for first responders, who face the unique challenge of managing these complex hazards in uncontrolled incident scenes.

However, the field is far from static. The rapid pace of innovation in battery chemistry, powertrain architecture, and vehicle design presents ongoing challenges and defines the key areas for future research and development. Several open questions remain critical to ensuring the long-term safety of this new automotive ecosystem:

- **Standardization of Training and Protocols:** While best practices exist, there remains a pressing need for globally harmonized and standardized training curricula and certification for technicians and first responders. How can these programs be scaled effectively to address the current knowledge gaps and ensure a consistent level of competency worldwide?
- **Adapting to New Technologies:** As manufacturers push towards higher-voltage systems (800V and beyond) and

introduce new battery chemistries (such as solid-state batteries), how must safety protocols, diagnostic tools, and PPE evolve to manage these new risks? Current standards may need significant revision to address these emerging challenges.

- **Improving Real-Time Diagnostics and Data Access:** The lack of real-time battery health data during service or an emergency is a major safety liability. Future research must focus on developing secure and reliable methods to transmit critical battery status information to technicians and responders, enabling more informed and safer interventions.

- **Addressing End-of-Life and Second-Life Safety:** The safety challenges of EVs do not end when the vehicle is retired. The handling, dismantling, and repurposing of end-of-life battery packs present a new and growing set of risks that require dedicated safety protocols and risk assessment frameworks.

In summary, ensuring safety in the age of the electric vehicle is a continuous process of research, adaptation, and education. By building upon the foundational principles outlined in this chapter and proactively addressing the challenges of tomorrow, the automotive industry can ensure that this technological revolution is not only sustainable but also safe for all who work within it.

References

Abada, S., Petit, M., Lecocq, A., Marlair, G., Sauvant-Moynot, V., & Huet, F. (2018). Combined experimental and modeling approaches of the thermal runaway of fresh and aged lithium-ion batteries. *Journal of Power Sources*, *399*, 264–273. https://doi.org/10.1016/j.jpowsour.2018.07.094

Ahmed, J., Stenkula, C., Omar, S., Ghanima, J., Bremtun, F. F., Bergan, J., … Ghanima, W. (2021). Patient outcomes after electrical injury – a retrospective study. *Scandinavian Journal of Trauma, Resuscitation and Emergency Medicine*, *29*(1), 114. https://doi.org/10.1186/s13049-021-00920-3

Andrews, C. (2012). Towards solving enigmas in electrical injury. *Critical Care*, *16*(1), 117. https://doi.org/10.1186/cc11209

Angalane, S. K., & Kasinathan, E. (2022). A review on polymeric insulation for high-voltage application under various stress conditions. *Polymer Composites*, *43*(8), 4803–4834. https://doi.org/10.1002/pc.26793

Baker, M. B., Binda, D. D., Nozari, A., & Baker, W. E. (2024). The Silent Threat of Hypokalemia after High Voltage Electrical Injuries: A Case Study and Review of the Literature. *Journal of Clinical Medicine*, *13*(10), 2852. https://doi.org/10.3390/jcm13102852

Beghi, M., Braghin, F., & Roveda, L. (2023). Enhancing Disassembly Practices for Electric Vehicle Battery Packs: A Narrative Comprehensive Review. *Designs*, *7*(5), 109. https://doi.org/10.3390/designs7050109

Beşiktaşli, E., & Yurtcu, A. (2025). Evaluation of Electric Vehicles and Charging Stations in terms of Occupational Health and Safety. *Amesia*, *6*(1), 1–15. https://doi.org/10.54559/amesia.1729996

Biering, K., Kærgaard, A., Carstensen, O., & Nielsen, K. J. (2023). Unconsciousness and amnesia after cross-body electric shocks not involving the head–A prospective cohort study. *PLoS ONE*, *18*(4 April), e0283957. https://doi.org/10.1371/journal.pone.0283957

Bisschop, R., Willstrand, O., & Rosengren, M. (2020). Handling Lithium-Ion Batteries in Electric Vehicles: Preventing and Recovering from Hazardous Events. *Fire Technology*, *56*(6), 2671–2694. https://doi.org/10.1007/s10694-020-01038-1

Biswas, B., Du, B. X., Florkowski, M., Hammarström, T., Judd, M. D., Kołtunowicz, W., … Stone, G. (2024). Trends in Diagnostics and Monitoring of High-Voltage Insulation. *IEEE Electrical Insulation Magazine*, *40*(4), 6–26. https://doi.org/10.1109/MEI.2024.10568085

Bjurström, A., Edin, H., Hillborg, H., Nilsson, F., Olsson, R. T., Pierre, M., … Hedenqvist, M. S. (2024). A Review of Polyolefin-Insulation Materials in High Voltage Transmission; From Electronic Structures to Final Products. *Advanced Materials*, *36*(52). https://doi.org/10.1002/adma.202401464

Borghei, M., & Ghassemi, M. (2021). Insulation Materials and Systems for More- A nd All-Electric Aircraft: A Review Identifying Challenges and Future Research Needs. *IEEE Transactions on Transportation Electrification*, *7*(3), 1930–1953. https://doi.org/10.1109/TTE.2021.3050269

Boudier-Revéret, M., Hsiao, M. Y., Shyu, S. G., & Chang, M. C. (2020). Injury of Corticospinal tract and Corticoreticular pathway caused by high-voltage electrical shock: a case report. *BMC Neurology*, *20*(1), 130. https://doi.org/10.1186/s12883-020-01707-2

Boyd, A. N., Hartman, B. C., Sood, R., & Walroth, T. A. (2019). A voltage-based analysis of fluid delivery and outcomes in burn patients with electrical injuries over a 6-year period. *Burns*, *45*(4), 869–875. https://doi.org/10.1016/j.burns.2018.08.020

Chandran, A. R., Hennen, M. D., Arkkio, A., & Belahcen, A. (2022). Safe Turn-Off Strategy for Electric Drives in Automotive Applications. *IEEE Transactions on Transportation Electrification*, *8*(1), 9–22. https://doi.org/10.1109/TTE.2021.3104461

Chang, C., Zhang, J., Yuan, S., Wang, K., Zhang, Y., Wu, D., & Qian, X. (2025). Comparative study on fire suppression of NCA18650 lithium-ion battery by several fire extinguishing agents. *Journal of Thermal Analysis and Calorimetry*, *150*(15), 11767–11779. https://doi.org/10.1007/s10973-024-13362-7

Chen, J., Li, K., & Yang, S. (2022). Electric Vehicle Fire Risk Assessment Based on WBS-RBS and Fuzzy BN Coupling. *Mathematics*, *10*(20), 3799. https://doi.org/10.3390/math10203799

Choi, S., Lee, K., Kim, J., Oh, S., Joo, J., Bae, E., … Kim, M. (2025). Early Detection and Suppression of Thermal Runaway in Large-Format Lithium-Ion Batteries: Insights from Experimental Analysis. *Energies*, *18*(1), 155. https://doi.org/10.3390/en18010155

Chombo, P. V., Laoonual, Y., & Wongwises, S. (2021). Lessons from the electric vehicle crashworthiness leading to battery fire. *Energies*, *14*(16), 4802. https://doi.org/10.3390/en14164802

Cui, Y., Liu, J., Han, X., Sun, S., & Cong, B. (2022). Full-scale experimental study on suppressing lithium-ion battery pack fires from electric vehicles. *Fire Safety Journal*, *129*, 103562. https://doi.org/10.1016/j.firesaf.2022.103562

da Costa, V. B. F., Bitencourt, L., Dias, B. H., Soares, T., de Andrade, J. V. B., & Bonatto, B. D. (2025). Life cycle assessment comparison of electric and internal combustion vehicles: A review on the main challenges and opportunities. *Renewable and Sustainable Energy Reviews*, *208*, 114988. https://doi.org/10.1016/j.rser.2024.114988

Dechent, D., Emonds, T., Stunder, D., Schmiedchen, K., Kraus, T., & Driessen, S. (2020). Direct current electrical injuries: A systematic review of case reports and case series. *Burns*, *46*(2), 267–278. https://doi.org/10.1016/j.burns.2018.11.020

Di Liberto, E., Borchiellini, R., Fruhwirt, D., & Papurello, D. (2025). A Review of Safety Measures in Battery Electric Buses. *Fire*, *8*(4), 159. https://doi.org/10.3390/fire8040159

Dorsz, A., & Lewandowski, M. (2021). Analysis of Fire Hazards Associated with the Operation of Electric Vehicles in Enclosed Structures. *Energies*, *15*(1), 11. https://doi.org/10.3390/en15010011

Feng, X., Ouyang, M., Liu, X., Lu, L., Xia, Y., & He, X. (2018). Thermal runaway mechanism of lithium ion battery for electric vehicles: A review. *Energy Storage Materials*, *10*, 246–267. https://doi.org/10.1016/j.ensm.2017.05.013

Feng, X., Ren, D., He, X., & Ouyang, M. (2020). Mitigating Thermal Runaway of Lithium-Ion Batteries. *Joule*, *4*(4), 743–770. https://doi.org/10.1016/j.joule.2020.02.010

Ghiji, M., Novozhilov, V., Moinuddin, K., Joseph, P., Burch, I., Suendermann, B., & Gamble, G. (2020). A review of lithium-ion battery fire suppression. *Energies*, *13*(19), 5117. https://doi.org/10.3390/en13195117

Grebtsov, D. K., Kubasov, M. K., Bernatskii, E. R., Beliauski, P. A., Kokorenko, A. A., Isokjanov, S. S., … Morozova, S. M. (2024). Electric Vehicle Battery Technologies: Chemistry, Architectures, Safety, and Management Systems. *World Electric Vehicle Journal*, *15*(12), 568. https://doi.org/10.3390/wevj15120568

Gusti, A. P., Waskito, D. H., Kaleg, S., Bowo, L. P., Pratama, A., Maulani, D. R., … Wiguna, I. K. C. P. (2025). A Systematic Literature Review of Risk Assessment Methodologies for Battery

Electric Vehicles. *Automotive Experiences*, *8*(1), 46–71. https://doi.org/10.31603/AE.12835

Haque, S. K. M., Ardila-Rey, J. A., Umar, Y., Mas'ud, A. A., Muhammad-Sukki, F., Jume, B. H., … Bani, N. A. (2021). Application and suitability of polymeric materials as insulators in electrical equipment. *Energies*, *14*(10), 2758. https://doi.org/10.3390/en14102758

Hong, J., Wang, Z., Qu, C., Ma, F., Xu, X., Yang, J., … Hou, Y. (2023). Fault Prognosis and Isolation of Lithium-Ion Batteries in Electric Vehicles Considering Real-Scenario Thermal Runaway Risks. *IEEE Journal of Emerging and Selected Topics in Power Electronics*, *11*(1), 88–99. https://doi.org/10.1109/JESTPE.2021.3097827

Ivanov, D. A., Sadykov, M. F., Yaroslavsky, D. A., Golenishchev-Kutuzov, A. V., & Galieva, T. G. (2021). Non-contact methods for high-voltage insulation equipment diagnosis during operation. *Energies*, *14*(18), 5670. https://doi.org/10.3390/en14185670

Ji, C., Liu, Y., Qi, P., Zhang, Z., & Zhang, S. (2023). Simulation Investigation of Water Spray on Suppressing Lithium-Ion Battery Fires. *Fire Technology*, *59*(3), 1221–1246. https://doi.org/10.1007/s10694-022-01302-6

Jia, Z., Wang, Z., Sun, Z., Liu, P., Zhu, X., & Sun, F. (2024). A Data-Driven Approach for Battery System Safety Risk Evaluation Based on Real-World Electric Vehicle Operating Data. *IEEE Transactions on Transportation Electrification*, *10*(3), 5660–5676. https://doi.org/10.1109/TTE.2023.3324450

Jiang, L., Diao, X., Zhang, Y., Zhang, J., & Li, T. (2021). Review of the charging safety and charging safety protection of electric vehicles. *World Electric Vehicle Journal*, *12*(4), 184. https://doi.org/10.3390/wevj12040184

Jindal, P., & Bhattacharya, J. (2019). Review—Understanding the Thermal Runaway Behavior of Li-Ion Batteries through Experimental Techniques. *Journal of The Electrochemical Society*, *166*(10), A2165–A2193. https://doi.org/10.1149/2.1381910jes

Kang, Y., Duan, B., Zhou, Z., Shang, Y., & Zhang, C. (2020). Online multi-fault detection and diagnosis for battery packs in electric vehicles. *Applied Energy*, *259*, 114170. https://doi.org/10.1016/j.apenergy.2019.114170

Kay, I., Farhad, S., Mahajan, A., Esmaeeli, R., & Hashemi, S. R. (2022). Robotic Disassembly of Electric Vehicles' Battery Modules for Recycling. *Energies*, *15*(13), 4856. https://doi.org/10.3390/en15134856

Khor, D., AlQasas, T., Galet, C., Barrash, J., Granchi, T., Bertellotti, R., & Wibbenmeyer, L. (2023). Electrical injuries and outcomes: A retrospective review. *Burns*, *49*(7), 1739–1744. https://doi.org/10.1016/j.burns.2023.03.015

Krzyżewska, I., & Chruzik, K. (2023). Maintenance and Exploitation of Electric, Hybrid, and Internal Combustion Vehicles. *Energies*, *16*(23), 7842. https://doi.org/10.3390/en16237842

Kurian, P., & Abbasian, M. (2025). Investigating High-Voltage Safety Concerns in Electric Vehicles Through Voltage Discharge Optimisation. *Energies*, *18*(4), 916. https://doi.org/10.3390/en18040916

Lee, H., Kim, Y. T., & Lee, S. W. (2023). Optimization of the Electrochemical Discharge of Spent Li-Ion Batteries from Electric Vehicles for Direct Recycling. *Energies*, *16*(6), 2759. https://doi.org/10.3390/en16062759

Li, C., Yang, Y., Xu, G., Zhou, Y., Jia, M., Zhong, S., … Zi, Y. (2022). Insulating materials for realising carbon neutrality: Opportunities,

remaining issues and challenges. *High Voltage*, *7*(4), 610–632. https://doi.org/10.1049/hve2.12232

Li, X., Zhang, M., Zhou, Z., Zhu, Y., Du, K., & Zhou, X. (2023). A novel dry powder extinguishant with high cooling performance for suppressing lithium ion battery fires. *Case Studies in Thermal Engineering*, *42*, 102756. https://doi.org/10.1016/j.csite.2023.102756

Lian, Y., Zeng, D., Ye, S., Zhao, B., & Wei, H. (2018). High-Voltage Safety Improvement Design for Electric Vehicle in Rear Impact. *Automotive Innovation*, *1*(3), 211–225. https://doi.org/10.1007/s42154-018-0030-z

Liu, B., Su, Y., Deng, Q., Jin, S., Chen, Y., & Ouyang, T. (2023). Reducing lithium-ion battery thermal runaway risk based on an integrated cooling strategy for electric vehicles. *International Journal of Heat and Mass Transfer*, *216*, 124594. https://doi.org/10.1016/j.ijheatmasstransfer.2023.124594

Liu, J., Xu, N., Shi, Y., Barnett, T., & Jones, S. (2023). Are first responders prepared for electric vehicle fires? A national survey. *Accident Analysis and Prevention*, *179*, 106903. https://doi.org/10.1016/j.aap.2022.106903

Liu, Y., Chen, H., Gao, J., Li, Y., Dave, K., Chen, J., … Perricone, G. (2021). Comparative analysis of non-exhaust airborne particles from electric and internal combustion engine vehicles. *Journal of Hazardous Materials*, *420*, 126626. https://doi.org/10.1016/j.jhazmat.2021.126626

Majeed, F., Jamal, H., Kamran, U., Noman, M., Ali, M. M., Shahzad, T., … Akhtar, F. (2024). Review–Recent Advances in Fire-Suppressing Agents for Mitigating Lithium-Ion Battery Fires. *Journal of The Electrochemical Society*, *171*(6), 060522. https://doi.org/10.1149/1945-7111/ad5620

Mohd Tohir, M. Z., & Martín-Gómez, C. (2023). Electric vehicle fire risk assessment framework using Fault Tree Analysis. *Open Research Europe*, *3*, 178. https://doi.org/10.12688/openreseurope.16538.1

Muram, F. U., Pop, P., & Javed, M. A. (2024). Assuring the safety of rechargeable energy storage systems in electric vehicles. *Journal of Systems Architecture*, *154*, 103218. https://doi.org/10.1016/j.sysarc.2024.103218

Ogbuka, I., Avera, S., & King, M. (2023). 213: One Shock Treated With Another: New-Onset Atrial Fibrillation After High-Voltage Electrical Injury. *Critical Care Medicine*, *51*(1), 90–90. https://doi.org/10.1097/01.ccm.0000906588.30822.fc

Paramane, A., Chen, X., Dai, C., Guan, H., Yu, L., & Tanaka, Y. (2020). Electrical insulation performance of cross-linked polyethylene/MgO nanocomposite material for ±320 kV high-voltage direct-current cables. *Polymer Composites*, *41*(5), 1936–1949. https://doi.org/10.1002/pc.25509

Pardo-Ferreira, M. C., Torrecilla-García, J. A., de las Heras-Rosas, C., & Rubio-Romero, J. C. (2020). New risk situations related to low noise from electric vehicles: Perception of workers as pedestrians and other vehicle drivers. *International Journal of Environmental Research and Public Health*, *17*(18), 1–16. https://doi.org/10.3390/ijerph17186701

Pardo-Ferreira, M. del C., Rubio-Romero, J. C., Galindo-Reyes, F. C., & Lopez-Arquillos, A. (2020). Work-related road safety: The impact of the low noise levels produced by electric vehicles according to experienced drivers. *Safety Science*, *121*, 580–588. https://doi.org/10.1016/j.ssci.2019.02.021

Ping, P., Gao, X., Kong, D., Gao, W., Feng, Z., Yang, C., … Dai, X. (2024). Experimental study on the synergistic strategy of liquid

nitrogen and water mist for fire extinguishing and cooling of lithium-ion batteries. *Process Safety and Environmental Protection*, *188*, 713–725. https://doi.org/10.1016/j.psep.2024.05.077

Pleşa, I., Noţingher, P. V., Schlögl, S., Sumereder, C., & Muhr, M. (2016). Properties of polymer composites used in high-voltage applications. *Polymers*, *8*(5), 173. https://doi.org/10.3390/polym8050173

Pollard, T. (n.d.). Electric car batteries: everything you need to know. Retrieved from carmagazine.co.uk website: https://www.carmagazine.co.uk/electric/ev-car-battery-capacity-tech/

Rådman, L., Nilsagård, Y., Jakobsson, K., Ek, Å., & Gunnarsson, L. G. (2016). Electrical injury in relation to voltage, "no-let-go" phenomenon, symptoms and perceived safety culture: a survey of Swedish male electricians. *International Archives of Occupational and Environmental Health*, *89*(2), 261–270. https://doi.org/10.1007/s00420-015-1069-3

Ren, D., Feng, X., Liu, L., Hsu, H., Lu, L., Wang, L., … Ouyang, M. (2021). Investigating the relationship between internal short circuit and thermal runaway of lithium-ion batteries under thermal abuse condition. *Energy Storage Materials*, *34*, 563–573. https://doi.org/10.1016/j.ensm.2020.10.020

Riba, J. R., Moreno-Eguilaz, M., & Bogarra, S. (2023). Tracking Resistance in Polymeric Insulation Materials for High-Voltage Electrical Mobility Applications Evaluated by Existing Test Methods: Identified Research Needs. *Polymers*, *15*(18), 3717. https://doi.org/10.3390/polym15183717

Rosewater, D. M. (2023). Reducing Risk When Performing Energized Work on Batteries. *IEEE Transactions on Industry*

Applications, *60*(2), 2732–2741. https://doi.org/10.1109/TIA.2023.3332828

Rui, X., Feng, X., Wang, H., Yang, H., Zhang, Y., Wan, M., … Ouyang, M. (2021). Synergistic effect of insulation and liquid cooling on mitigating the thermal runaway propagation in lithium-ion battery module. *Applied Thermal Engineering*, *199*, 117521. https://doi.org/10.1016/j.applthermaleng.2021.117521

Saleem, M. Z., & Akbar, M. (2022). Review of the Performance of High-Voltage Composite Insulators. *Polymers*, *14*(3), 431. https://doi.org/10.3390/polym14030431

Shahid, S., & Agelin-Chaab, M. (2022). A review of thermal runaway prevention and mitigation strategies for lithium-ion batteries. *Energy Conversion and Management: X*, *16*, 100310. https://doi.org/10.1016/j.ecmx.2022.100310

Shahsavarian, T., Wu, X., Lents, C., Zhang, D., Li, C., & Cao, Y. (2021). Temperature-dependent partial discharge characteristics of high temperature materials at DC voltage for hybrid propulsion systems. *High Voltage*, *6*(4), 590–598. https://doi.org/10.1049/hve2.12110

Shih, J. G., Shahrokhi, S., & Jeschke, M. G. (2017). Review of Adult Electrical Burn Injury Outcomes Worldwide: An Analysis of Low-Voltage vs High-Voltage Electrical Injury. *Journal of Burn Care and Research*, *38*(1), e293–e298. https://doi.org/10.1097/BCR.0000000000000373

Song, L., Zheng, Y., Xiao, Z., Wang, C., & Long, T. (2022). Review on Thermal Runaway of Lithium-Ion Batteries for Electric Vehicles. *Journal of Electronic Materials*, *51*(1), 30–46. https://doi.org/10.1007/s11664-021-09281-0

Spies, C., & Trohman, R. G. (2006). Narrative review: Electrocution and life-threatening electrical injuries. *Annals of Internal Medicine*, *145*(7), 531–537. https://doi.org/10.7326/0003-4819-145-7-200610030-00011

Stave, C., & Carlson, A. (2017). A case study exploring firefighters' and municipal officials' preparedness for electrical vehicles. *European Transport Research Review*, *9*(2), 25. https://doi.org/10.1007/s12544-017-0240-1

Takada, T., Fujitomi, T., Mori, T., Iwata, T., Ono, T., Miyake, H., & Tanaka, Y. (2017). New diagnostic method of electrical insulation properties based on current integration. *IEEE Transactions on Dielectrics and Electrical Insulation*, *24*(4), 2549–2558. https://doi.org/10.1109/TDEI.2017.006355

Tang, W., Yuan, L., Thomas, R., & Soles, J. (2023). Comparison of Fire Suppression Techniques on Lithium-Ion Battery Pack Fires. *Mining, Metallurgy and Exploration*, *40*(4), 1081–1087. https://doi.org/10.1007/s42461-023-00765-7

Tran, M. K., Mevawalla, A., Aziz, A., Panchal, S., Xie, Y., & Fowler, M. (2022). A Review of Lithium-Ion Battery Thermal Runaway Modeling and Diagnosis Approaches. *Processes*, *10*(6), 1192. https://doi.org/10.3390/pr10061192

Ubaldi, S., Di Bari, C., Quinterno, M., De Rosa, A., Mazzaro, M., Ferrigno, G., … Russo, P. (2024). Suppression capacity and environmental impact of three extinguishing agents for lithium-ion battery fires. *Case Studies in Chemical and Environmental Engineering*, *10*, 100810. https://doi.org/10.1016/j.cscee.2024.100810

Villagrossi, E., & Dinon, T. (2023). Robotics for electric vehicles battery packs disassembly towards sustainable remanufacturing.

Journal of Remanufacturing, *13*(3), 355–379. https://doi.org/10.1007/s13243-023-00134-z

Waldmann, V., Narayanan, K., Combes, N., Jost, D., Jouven, X., & Marijon, E. (2018). Electrical cardiac injuries: current concepts and management. *European Heart Journal*, *39*(16), 1459–1465. https://doi.org/10.1093/eurheartj/ehx142

Wang, H., Zhang, Y., Zhang, G., Zhang, Z., Zhang, Z., & Zhao, Z. (2025). Study on the Fire Suppression Efficiency of Common Extinguishing Agents for Lithium Iron Phosphate Battery Fires. *Fire Technology*. https://doi.org/10.1007/s10694-024-01687-6

Wöhrl, K., Geisbauer, C., Nebl, C., Lott, S., & Schweiger, H. G. (2021). Crashed electric vehicle handling and recommendations—state of the art in Germany. *Energies*, *14*(4), 1040. https://doi.org/10.3390/en14041040

Wójcik, G., & Przystałka, P. (2025). Towards Safer Electric Vehicles: Autoencoder-Based Fault Detection Method for High-Voltage Lithium-Ion Battery Packs. *Sensors*, *25*(5), 1369. https://doi.org/10.3390/s25051369

Wu, Y., Wu, Q., Sun, M., Zeng, Z., Cheng, S., & Xie, J. (2025). Enhancing Safety in Lithium Batteries: A Review on Functional Separators Controlling Substance and Heat During Thermal Runaway. *Advanced Functional Materials*, *35*(30). https://doi.org/10.1002/adfm.202425698

Xu, G., Han, Q., Chen, H., Xia, Y., Liu, Z., & Tian, S. (2022). Safety warning analysis for power battery packs in electric vehicles with running data. *Journal of Energy Storage*, *56*, 105878. https://doi.org/10.1016/j.est.2022.105878

Xu, J., Guo, P., Duan, Q., Yu, X., Zhang, L., Liu, Y., & Wang, Q. (2020). Experimental study of the effectiveness of three kinds of

extinguishing agents on suppressing lithium-ion battery fires. *Applied Thermal Engineering*, *171*, 115076. https://doi.org/10.1016/j.applthermaleng.2020.115076

Yang, H., Yang, J., & Zhang, X. (2021). DC-Bus Capacitor Maximum Power Discharge Strategy for EV-PMSM Drive System with Small Safe Current. *IEEE Access*, *9*, 132158–132167. https://doi.org/10.1109/ACCESS.2021.3112462

Yuan, S., Chang, C., Yan, S., Zhou, P., Qian, X., Yuan, M., & Liu, K. (2021). A review of fire-extinguishing agent on suppressing lithium-ion batteries fire. *Journal of Energy Chemistry*, *62*, 262–280. https://doi.org/10.1016/j.jechem.2021.03.031

Zhang, B., Bewley, R. L., Tanim, T. R., & Walker, L. K. (2022). Electric vehicle post-crash Recovery—Stranded energy issues and mitigation strategy. *Journal of Power Sources*, *552*, 232239. https://doi.org/10.1016/j.jpowsour.2022.232239

Zhang, B., Tanim, T. R., & Black, D. (2025). A Software/Hardware Framework for Efficient and Safe Emergency Response in Post-Crash Scenarios of Battery Electric Vehicles. *Batteries*, *11*(2), 80. https://doi.org/10.3390/batteries11020080

Zhang, J., Zhang, L., Sun, F., & Wang, Z. (2018). An Overview on Thermal Safety Issues of Lithium-ion Batteries for Electric Vehicle Application. *IEEE Access*, *6*, 23848–23863. https://doi.org/10.1109/ACCESS.2018.2824838

Zhang, L., Duan, Q., Liu, Y., Xu, J., Sun, J., Xiao, H., & Wang, Q. (2021). Experimental investigation of water spray on suppressing lithium-ion battery fires. *Fire Safety Journal*, *120*, 103117. https://doi.org/10.1016/j.firesaf.2020.103117

Zhang, L., Li, Y., Duan, Q., Chen, M., Xu, J., Zhao, C., … Wang, Q. (2020). Experimental study on the synergistic effect of gas

extinguishing agents and water mist on suppressing lithium-ion battery fires. *Journal of Energy Storage*, *32*, 101801. https://doi.org/10.1016/j.est.2020.101801

Zhang, X., Chen, S., Zhu, J., & Gao, Y. (2023). A Critical Review of Thermal Runaway Prediction and Early-Warning Methods for Lithium-Ion Batteries. *Energy Material Advances*, *4*. https://doi.org/10.34133/energymatadv.0008

Zhao, J., Lv, Z., Li, D., Feng, X., Wang, Z., Wu, Y., … Burke, A. F. (2024). Battery engineering safety technologies (BEST): M5 framework of mechanisms, modes, metrics, modeling, and mitigation. *ETransportation*, *22*, 100364. https://doi.org/10.1016/j.etran.2024.100364

Zhou, H., He, J., Gao, S., Cao, X., Li, C., Zhang, Q., … Kang, R. (2025). Critical Perspectives on the Design of Polymeric Materials for Mitigating Thermal Runaway in Lithium-Ion Batteries. *Polymers*, *17*(9), 1227. https://doi.org/10.3390/polym17091227

Zorn, M., Ionescu, C., Klohs, D., Zähl, K., Kisseler, N., Daldrup, A., Friedrich, B. (2022). An Approach for Automated Disassembly of Lithium-Ion Battery Packs and High-Quality Recycling Using Computer Vision, Labeling, and Material Characterization. *Recycling*, *7*(4), 48. https://doi.org/10.3390/recycling7040048

Zuo, K., Li, Z., Liang, H., Wang, Z., & Ouyang, T. (2025). An integrated scheme to prevent the propagation of Li-ion battery thermal runaway. *International Journal of Heat and Mass Transfer*, *241*, 126725. https://doi.org/10.1016/j.ijheatmasstransfer.2025.126725

GEÇİCİ KAPAK

Kapak tasarımı devam ediyor.